

# **SPARK INDUCED FLOW IN QUIESCENT AIR**

by

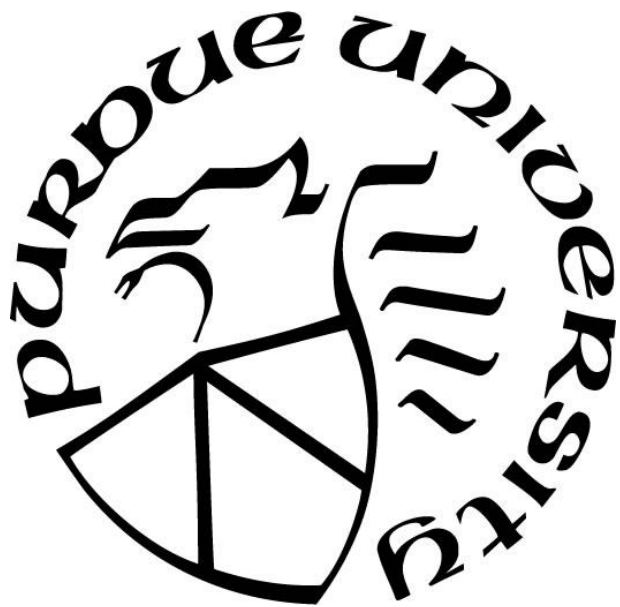
**Bhavini Singh**

**A Dissertation**

*Submitted to the Faculty of Purdue University*

*In Partial Fulfillment of the Requirements for the degree of*

**Doctor of Philosophy**



School of Aeronautics and Astronautics

West Lafayette, Indiana

May 2021

**THE PURDUE UNIVERSITY GRADUATE SCHOOL**  
**STATEMENT OF COMMITTEE APPROVAL**

**Dr. Sally P. M Bane, Chair**

School of Aeronautics and Astronautics

**Dr. Pavlos P. Vlachos**

School of Aeronautics and Astronautics

**Dr. Alexey Shashurin**

School of Aeronautics and Astronautics

**Dr. Sergey O. Macheret**

School of Aeronautics and Astronautics

**Dr. Gregory Blaisdell**

School of Aeronautics and Astronautics

**Approved by:**

Dr. Gregory Blaisdell

## ACKNOWLEDGMENTS

I would like to thank my committee members, Prof. Bane, Prof. Vlachos, Prof. Shashurin, Prof. Macheret and Prof. Blaisdell for their guidance and support throughout my PhD. I would also like to thank my funding sources, First Year Engineering for funding me as a graduate teaching assistant throughout my PhD and to the U.S. Department of Energy, Office of Science, Office of Fusion Energy Sciences who supported this work under Award No. DE-SC0018156.

This work would not have been possible without collaboration among research groups. I would especially like to thank Lalit Rajendran with whom I have collaborated on all the research objectives that comprise this work. Additional thanks to Jiacheng Zhang, Dr. Sayantan Bhattacharya and Dr. Rohan Gejji for their collaborations.

Finally, the machinists at the Aerospace Sciences Laboratory, Jim Younts, Robin Snodgrass and Jerry Hahn expertly fabricated key elements of the experimental set ups used in this work and the expertise that John Phillips provided with the high voltage pulser has ensured its continued use in the completion of these research projects.

# TABLE OF CONTENTS

LIST OF FIGURES .....	7
ABSTRACT.....	10
1. INTRODUCTION.....	12
1.1 Motivation.....	12
1.2 Background.....	13
1.2.1 Plasma generation mechanisms.....	13
1.2.2 Plasma induced flow field.....	14
1.2.2.1 Shock wave .....	14
1.2.2.2 Hot gas kernel and vortex rings .....	15
1.2.2.3 Vorticity generation .....	16
1.2.2.4 Effect of electrode geometry and electrical energy deposited .....	16
1.3 Primary research objectives.....	17
1.4 Dissertation format.....	18
2. TWO REGIME COOLING IN FLOW INDUCED BY A SPARK DISCHARGE .....	19
Abstract.....	19
2.1 Introduction .....	19
2.2 Experimental methods and techniques.....	21
2.2.1 Plasma generation – pulser and electrode description.....	22
2.2.2 Stereoscopic Particle Image Velocimetry.....	23
2.2.2.1 Experimental Setup.....	23
2.2.2.2 Image Processing.....	24
2.2.2.3 Uncertainty quantification .....	24
2.2.3 Background Oriented Schlieren.....	25
2.2.3.1 Experimental Setup.....	25
2.2.3.2 Image Processing.....	26
2.2.3.3 Uncertainty quantification .....	28
2.2.4 Post processing metrics.....	28
2.2.5 Non-dimensionalization.....	29
2.3 Results and Discussion .....	30
2.3.1 Observations from experimental results.....	30

2.3.2	A model for the effect of cold gas entrainment on the kernel cooling process.....	35
2.3.3	Calculation of parameters in the cooling model.....	37
2.3.4	Results of the data driven cooling model .....	39
2.4	Conclusions .....	40
	Appendix .....	42
3.	<b>VORTEX RINGS DRIVE ENTRAINMENT AND COOLING IN FLOW INDUCED BY A SPARK DISCHARGE.....</b>	<b>45</b>
	Abstract.....	45
3.1	Introduction .....	45
3.2	Vortex ring cooling model.....	47
3.2.1	Entrainment model .....	48
3.2.2	Thin core vortex ring model.....	49
3.3	Experimental methods and techniques.....	51
3.3.1	Plasma generation.....	51
3.3.2	Simultaneous velocity and density measurements .....	51
3.3.2.1	Experimental set-up .....	51
3.3.2.2	S-PIV image processing and uncertainty quantification .....	52
3.3.2.3	BOS image processing and uncertainty quantification .....	53
3.3.3	Non-dimensionalization of results.....	54
3.3.4	Entrainment function calculation from PIV velocity fields .....	54
3.3.5	Post-processing metrics and calculation of parameters .....	55
3.4	Results and discussion.....	57
3.4.1	Spatial organization of the flow field and the effect of energy .....	57
3.4.2	Application of vortex ring cooling model .....	59
3.4.2.1	Entrainment.....	60
3.4.2.2	Cooling.....	60
3.5	Conclusions .....	62
4.	<b>SHOCK GENERATED VORTICITY IN SPARK DISCHARGES.....</b>	<b>64</b>
	Abstract.....	64
4.1	Introduction .....	64
4.2	Vorticity generation due to a curved shock.....	66

4.3	Experimental methods and techniques.....	68
4.3.1	Schlieren imaging.....	69
4.3.2	Processing metrics and calculations of parameters .....	69
4.3.2.1	Shock outline detection .....	70
4.3.2.2	Shock velocity calculation.....	71
4.3.2.3	Shock generated vorticity calculation.....	71
4.3.3	Uncertainty quantification.....	72
4.4	Results and discussion.....	73
4.4.1	Shock wave induced by spark discharge .....	73
4.4.2	Vorticity estimation based on shock curvature .....	74
4.4.3	Comparison of shock-estimated vorticity to experimental results from S-PIV .....	75
4.5	Conclusions .....	78
5.	TOWARDS 3D VELOCITY MEASUREMENTS IN SPARK INDUCED FLOWS.....	80
	Abstract.....	80
5.1	Introduction .....	80
5.2	Experimental methods and techniques.....	81
5.2.1	Tomographic particle image velocimetry experimental set-up.....	81
5.2.2	Image processing.....	82
5.2.2.1	Calibration.....	82
5.2.2.2	Image pre-processing .....	83
5.2.2.3	Volume reconstruction and velocity estimation .....	84
5.3	Preliminary results .....	84
5.3.1	Volume reconstruction from MART.....	84
5.3.2	3D velocity field.....	85
5.4	Summary and recommendations .....	86
	Appendix .....	88
6.	CONCLUSION .....	91
6.1	Summary .....	91
6.2	Recommendations for future work .....	93
	REFERENCES.....	95
	VITA.....	104

## LIST OF FIGURES

Figure 1.1: Schematic showing the evolution of the flow field induced by a single spark discharge. (a) A shock wave and a cylindrical shaped hot gas kernel are induced at early times ( $< 20 \mu\text{s}$  after the spark discharge). The initially cylindrical shock wave evolves into a spherical wave while also decaying in strength with time. (b) A pair of vortex rings are formed near each electrode tip which entrain cold, ambient gas, leading to subsequent cooling of the hot gas kernel ( $\sim 100 \mu\text{s} - 1 \text{ms}$  after the spark discharge). (c) The two vortex rings move towards each other, eventually colliding, and in time the hot gas kernel cools to ambient. .... 15

Figure 2.1: (a) Sketch of the cone-tipped electrode, (b) the two-electrode configuration used for plasma generation, and (c) sample current, voltage and energy waveform produced during a spark discharge in a 5 mm electrode gap..... 22

Figure 2.2: Schematic of the experimental set-up for S-PIV measurements of the plasma-induced flow field..... 23

Figure 2.3: Experimental schematic of the primary components of the BOS system. .... 26

Figure 2.4: Projection of a 2D axisymmetric field. .... 28

Figure 2.5: Time evolution of the density of the hot gas kernel from  $t/\tau = 1.9$  (0.15 ms) to 26.6 (2.05 ms) obtained from BOS measurements. The measurements show minimum kernel densities ( $\rho/\rho_{shock}$ ) as low as 0.3 and the evolution of the kernel shape from cylindrical to toroidal shape for a single test where  $\rho_{shock} = 1.47 \text{ kg/m}^3$  and  $\tau = 0.08 \text{ ms}$ ..... 31

Figure 2.6: (a) Time history of mean kernel density inside BOS control volume, for the same test as in Figure 2.5, showing presence of two cooling regimes, each with different rates of cooling, with inset of identified kernel control volume from BOS data at  $t/\tau$  values of 3.2, 8.4 and 20.1 (b) fast and slow cooling rates for all tests, showing no dependence on energy deposited..... 32

Figure 2.7: Coherent vorticity induced by the spark from  $t/\tau = 0.98$  (0.07 ms) to 27.7 (2.0 ms) obtained from PIV measurements. The results show motion of a pair of vortex rings towards each other and collision of the vortex rings followed by decay, for a single test where  $u_{shock} = 66 \text{ m/s}$  and  $\tau = 0.07 \text{ ms}$ ..... 33

Figure 2.8: (a) Map of vortex trajectories showing motion towards  $y/d = 0$  and simultaneous radial expansion in  $x$ . (b) Time history of mean radius of top and bottom vortex rings showing overall expansion and time history of mean circulation showing decay post collision of the vortex rings. .... 34

Figure 2.9: Comparison of cooling regime changeover points obtained from BOS with vortex ring collision times obtained from PIV. Quartiles of changeover points from the fast cooling to slow cooling range between  $t/\tau = 8.9$  and 12.4 for BOS and quartiles of collision times range between  $t/\tau = 7.7$  and 12.2 for PIV..... 34

Figure 2.10: Cooling ratios calculated from S-PIV and BOS measurements show that in the fast regime, the total cooling effect observed from the kernel density measurement is statistically equivalent to the ratio measured from the cold gas entrained. .... 40

Figure 3.1: (a) Schematic of the vortex ring cooling model showing entrainment of cold ambient gas into the hot gas kernel, hypothesized to be due to a pair of thin core vortex rings. (b) Schematic showing a thin core ring with ring radius  $R$ , core radius  $a$ , circulation  $\Gamma$  and  $z$ -component of ring velocity  $U_z$ . Entrainment ( $\mathbf{V}_{in}$ ) is calculated using the thin core model inside the core and filament model outside. The effect of the second ring on entrainment across the boundary of the first ring is negligible, and vice versa. .... 48

Figure 3.2: (a) Schematic of the experimental set-up for simultaneous S-PIV and BOS measurements of the plasma-induced flow field. (b) Timing diagram used to synchronize the simultaneous measurements. .... 52

Figure 3.3: Post-processing steps for S-PIV and BOS measurements showing the identification of coherent vortex rings and density calculation. The centroids of the identified vortex rings are used to define the control volume used for entrainment calculations from experiment and model as well as mean kernel density calculation from BOS. .... 57

Figure 3.4: Time evolution of the induced hot gas kernel and vortex rings for the highest energy case (5.1 mJ, top) and the lowest energy case (2.2 mJ, bottom). A portion of the pair of vortex rings is located inside the hot gas kernel for all tests, with the spatial distribution of the vortex rings controlling the shape of the hot gas kernel. The intensity of the hot gas kernel is scaled using the mean kernel density, with a darker kernel signifying lower densities. .... 59

Figure 3.5: (a) Comparison of the total instantaneous entrainment calculated from the vortex ring model to experimental values calculated from least-squares integration of the S-PIV measurements and (b) comparison of cooling ratios from the entrainment-based calculations from the vortex ring model and the least-squares integration of the S-PIV measurements to the cooling ratios from the density-based calculations from BOS density data. .... 61

Figure 4.1: Schematic of shock generated due to a spark discharge showing (a) the curved nature of the shock wave in cylindrical coordinates and the misalignment of pressure and density behind the shock due to non-uniform shock strength; (b) the local coordinate system for a segment of the shock with normal shock velocity  $U_s$  and horizontal component of shock velocity  $U$  ..... 68

Figure 4.2: Schematic of the experimental set-up for schlieren measurements of the plasma-induced flow field. .... 69

Figure 4.3: Processing steps used to calculate the vorticity jump across a shock wave using images obtained from schlieren experiments. The  $z$ -location of the electrode tip is shown as a gray dashed line. .... 72

Figure 4.4: (a) Time evolution of a shock wave induced by a single spark discharge (4.9 mJ energy and  $\tau = 14 \mu s$ ) between two electrodes (5mm gap). (b) Vorticity field measured in prior work for a similar spark discharge (5 mm gap, 4.8 mJ,  $\tau = 14.1 \mu s$ ) showing a pair of vortex rings generated near the electrode tips[95]. .... 74

Figure 4.5: Normalized spatial variation of shock properties: (a) shock profile, (b) curvature, (c) tangential velocity, (d) density ratio, and (e) vorticity jump across the shock. Orange profiles are calculated using the shock profile, green profiles using a combination of the shock profile and the shock velocity. The  $z$ -location of the electrode tip is shown as a gray dashed line. .... 75

Figure 4.6: (a) The locations of peak vorticity ( $z\omega$ ) and peak shockcurvature ( $z\kappa$ ) and (b) shock curvature, (c) tangential velocity, and (d) density ratio values used to calculate the maximum vorticity jump across the shock as a function of the analytic, normalized pressure gradient. .... 77

Figure 4.7: Comparison between the non-dimensionalized peak vorticity estimated from the schlieren images with a curved shock model and mean vorticity from PIV measurements. .... 78

Figure 5.1: Schematic of the experimental set-up for tomographic PIV measurements of the plasma-induced flow field..... 82

Figure 5.2: XY, ZY and XZ projections of the reconstructed volume from raw images and the reconstructed volume from the preprocessed images of the spark experiment..... 85

Figure 5.3: (a) Isometric view and (b) front, side and top views of 3D vorticity field (contours) and velocity field (vectors) of the spark induced flow..... 86

Figure 5.4: (a) XY, ZY and XZ projections of the true intensity volume, the reconstructed volume from raw images and the reconstructed volume from the preprocessed images of the synthetic data. (b) A spatial map of the reconstruction quality of the projections with the raw images and the preprocessed images..... 90

## ABSTRACT

Nanosecond spark plasma actuators provide an opportunity to reduce pollutants by promoting efficient combustion in engines or provide targeted, tunable, flow control over vehicles, due to their ability to influence flow and combustion through multiple mechanisms. The plasma actuators can be physically unobtrusive, can be turned on and off and their low duty cycle, large bandwidth, and light weight make them more appealing than other control approaches. One method by which these plasma actuators interact with the environment is by inducing a complex local flow field and in order, to design scalable, high frequency actuators effectively, it is necessary to first understand the flow induced by a single spark discharge. Most experimental analysis on the flow induced by spark discharges has been restricted to qualitative descriptions of the flow field, primarily due to the difficulties associated with measuring such a transient and highly complex flow with sufficient spatiotemporal resolution. Quantitative, experimental characterization of the flow induced by a spark discharge remains lacking.

A spark discharge produces a shock wave and a hot gas kernel with a complex flow field following the shock. In this work, combined experimental and theoretical characterization of the spark induced flow is performed through a series of high spatiotemporal resolution measurements of the density and velocity fields and reduced-order modeling. The work investigates the mechanisms driving the cooling and vorticity generation in spark induced flow and the 3D nature of the flow field. Planar (2D-3C) and volumetric (3D-3C) velocity measurements are taken using stereoscopic particle image velocimetry (SPIV) and tomographic PIV, respectively. Density measurements are taken using background oriented schlieren (BOS) and high speed schlieren imaging is used to capture the shock wave induced by the spark.

The work shows that spark plasma discharges induce vortex rings whose vorticity is likely generated due to baroclinic torque arising from the non-uniform strength of the induced shock wave. The hot gas kernel cools in two stages: an initially fast cooling regime, followed by a slower cooling process. Reduced order analytical models are developed to describe the cooling observed in the fast regime and the role of the vortex rings in the entrainment of cold ambient gas and the cooling of the hot gas kernel. The results show that the vortex rings entrain ambient gas and drive

cooling in the fast, convective regime, cooling approximately 50% of the hot gas within the first millisecond of the induced flow. An increase in the electrical energy deposited in the spark gap increases the shock strength and curvature and increases the vortex ring strength, thereby increasing the cooling rate and expansion of the hot gas kernel. The volumetric velocity measurements capture one of the two induced vortex rings and provide a framework for the improvements needed in future tomographic PIV experiments of the spark induced flow field, necessary in assessing the 3D nature of the induced vortex rings.

The results of this work provide the first set of quantitative, experimental data on flow induced by nanosecond spark discharges that can be used for validation of computational fluid dynamics (CFD) simulations. The results demonstrate that spark plasmas induce vortex ring-driven mixing flows and the results on mixing and cooling of the hot gas kernel can be extended to any passive scalars present in the flow field as well as inform pulsation frequencies and actuator designs for flow and combustion control. The results from the reduced order modeling can inform future studies and applications of nanosecond spark discharges and can be extended to a variety of other types of plasma discharges like laser sparks, long duration sparks and surface discharges with similar induced flow fields.

# 1. INTRODUCTION

## 1.1 Motivation

Plasma discharges in gasses are created by breakdown of the gas in the presence of a strong electromagnetic field leading to the formation of ionized species. These discharges have applications in flow and combustion control, material processing, biomedicine, nanotechnology, and environmental engineering [1]–[6]. Flow can be induced by plasma discharges via either an electrohydrodynamic mechanism such as in dielectric barrier discharge (DBD) actuators driven by AC voltage or via the thermal mechanism such as in spark discharge actuators. The former of these two actuator types, AC-DBDs, have been the most studied types of plasma actuators [3], [6]–[9]. With these actuators, a body force is generated due to the presence of an electric field, inducing flow resembling a tangential wall jet with velocities on the order of  $10 \text{ m s}^{-1}$  [6].

Spark plasma discharges are generated by raising the voltage difference between two electrodes until the breakdown voltage is reached, resulting in ionization of the gas in the electrode gap and a rapid release of energy which results in the formation of a shock wave [10] as well as a region of hot gas that expands and cools with time [11]. Sparks generated using microsecond-duration high voltage pulses were the focus of many computational studies [12]–[14] as well as some experimental investigations, [15]–[17]. More recently, nanosecond repetitively pulsed (NRP) discharges have gained interest due to their ability to efficiently generate excited species at atmospheric pressure with relatively low power input [18], [19] and because their low duty cycle makes them more energy efficient to operate than AC or DC plasmas. A characteristic of these discharges is very rapid heating on a nanosecond time scale that results in production of shock waves and complex induced flow.

While NRP spark plasma discharges are being applied for various flow and combustion control applications [20]–[23], a detailed characterization of the flow induced by these discharges is still lacking. Computations on the flow induced by a single nanosecond spark were so far restricted to the very early stages ( $< 100 \mu\text{s}$ ) of flow development [24]. While this study showed the presence of a torus-shaped hot gas kernel and a weak shock, the development of the kernel in the post shock

wave phase of the flow, and the associated heat, mass and momentum transport mechanisms which are crucial for the design of flow and combustion control systems, have not been characterized. Additionally, researchers have in the past hypothesized that there is a strong coupling between the velocity induced by the spark discharge and the subsequent cooling of the hot gas kernel [16] but have not been able to show this using quantitative experimental results. Recent work on the applications of NRP discharges to ignition showed that the pulse frequency and number of pulses have a distinct effect on the size of the flame kernel, and this effect was attributed to be due to a possible coupling between the characteristic recirculation time from the induced flow and the inter-pulse time interval [25]–[27]. However, no quantitative experimental measurements of the induced velocity field and the induced hot gas kernel exist to verify this claim. The majority of the experimental analysis on flow induced by spark discharges in the late stages ( $> 100 \mu\text{s}$ ) was restricted to qualitative descriptions of the flow field [13], [16], primarily due to the difficulties associated with measuring such a transient and highly complex flow field with sufficient spatiotemporal resolution.

Experimentally characterizing the flow induced by a single spark, over the duration of its influence, is certainly the first step in understanding these actuators so as to enable informed actuator designs tailored to specific applications. To fill the knowledge gaps that exist, this work uses experimental measurement of the induced velocity field and density field, combined with reduced order modelling, to characterize the flow field induced by a single spark. This characterization involves a quantitative assessment of the induced flow structures as well as an evaluation of the development of the induced hot gas kernel and heat transfer mechanisms responsible for its cooling.

## **1.2 Background**

### **1.2.1 Plasma generation mechanisms**

The formation of a spark plasma discharge between a pair of electrodes is attributed to highly random and chaotic electron avalanches, leading to the growth of thin ionized channels (streamers), in the presence of an electric field [10]. Spark plasma discharges usually occur at higher pressures (near atmospheric or higher), where thermal instability causes the plasma to constrict into a localized filament with high current, extending the length of the electrode gap. The spark formation

is accompanied by an ultrafast, two-step heating mechanism. The first step of the two-step ultrafast heating is characterized by electron impact excitation of gaseous nitrogen followed by the second step which involves the quenching of the excited nitrogen by oxygen molecules producing oxygen atoms and heat.

## **1.2.2 Plasma induced flow field**

### **1.2.2.1 Shock wave**

The rapid release of energy in the spark plasma discharges leads to fast heating in the gap, accompanied by a sharp rise in pressure resulting in the formation of a shock wave. The shock wave then moves radially out of the center of the gap at time scales on the order of a few microseconds [28], [29], giving rise to a transient three-dimensional flow field [30]. This process is illustrated in Figure 1.1(a). In their computational investigations of spark discharges, Bane *et al.* [30] found that a strong shock is induced and takes on a cylindrical shape along the length of the electrode gap, except near the electrode tips where the shock is spherical. Some researchers found via computations that at early times, the shock wave induced by nanosecond sparks resembles a blast wave, but decays rapidly into an acoustic wave [31] while other researchers suggest, also through computations, that the shock wave propagates at the speed of sound from about 1 ns after spark actuation [24]. The shock wave velocity at times  $> 5 \mu\text{s}$  after the spark was investigated experimentally by few researchers and found to be close to the speed of sound [28]. The speed and strength of the shock wave induced are critical in determining the relationship between the shock wave, the induced velocity behind it, and the flow field induced at later times. Our results capturing the flow induced by microsecond discharges, have shown promise in using the induced velocity behind this induced shock wave in scaling circulation and entrainment in the spark gap at later times [17].

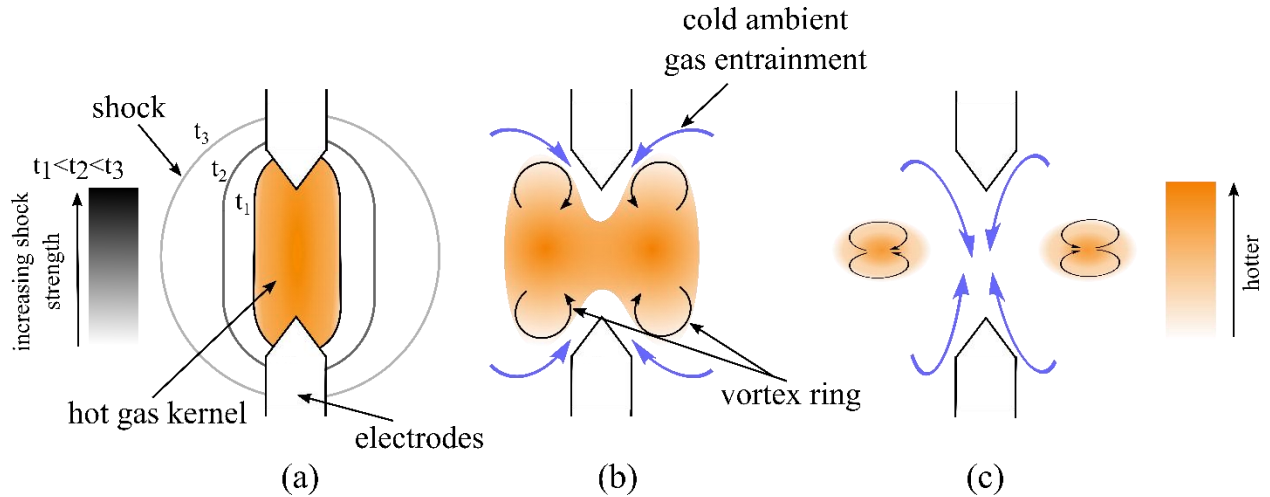


Figure 1.1: Schematic showing the evolution of the flow field induced by a single spark discharge. (a) A shock wave and a cylindrical shaped hot gas kernel are induced at early times ( $< 20 \mu\text{s}$  after the spark discharge). The initially cylindrical shock wave evolves into a spherical wave while also decaying in strength with time. (b) A pair of vortex rings are formed near each electrode tip which entrain cold, ambient gas, leading to subsequent cooling of the hot gas kernel ( $\sim 100 \mu\text{s} - 1 \text{ms}$  after the spark discharge). (c) The two vortex rings move towards each other, eventually colliding, and in time the hot gas kernel cools to ambient.

### 1.2.2.2 Hot gas kernel and vortex rings

At longer time scales, the hot gas kernel in the gap expands and cools. There is consensus among researchers that vortices are induced in the flow [12]–[14], [16], [17]. Much of the previous work was limited to computational studies and schlieren visualization of microsecond and hundreds of nanosecond sparks. It was found that the spark-induced hot gas kernel is initially cylindrical in shape, then deforms into a torus [13], [16]. The deformation was attributed to the inflow of cold gas from the surroundings [12], [16] which mixes with the hot gas kernel. The cooling of the hot gas kernel was attributed to the convective mechanisms induced by these vortices [16], however without detailed proof. In more recent experimental results presenting quantitative information on the flow induced by microsecond sparks [17], we showed the presence of a pair of vortex rings around the hot gas kernel for 5 mm and 8 mm electrode gap distances. The vortex rings were shown to entrain jets of surrounding gas into the electrode gap and the circulation of the vortex rings as well as the rate of entrainment were found to decay over time. The entrainment of cold gas into the gap and the change in circulation with time was not related to the cooling of the hot

gas kernel in this study. The vortices induced by the spark and their role in flow entrainment and subsequent cooling of the hot gas kernel are illustrated in Figure 1.1(b) and (c).

### **1.2.2.3 Vorticity generation**

The vorticity that constitutes the vortex rings has received some interest. Researchers have used CFD simulations to study the flow field at early times during the spark induced shock wave, and have suggested that there are two possible sources of vorticity generation, both through a baroclinic effect: (1) vorticity production due to the non-uniformity in the shock strength [30], [32], [33] (2) vorticity production due to the interaction of pressure gradients behind the shock wave with the hot gas kernel [32], [34]–[38]. There has been little experimental investigation on the contribution of each of these sources of vorticity in nanosecond spark discharges.

### **1.2.2.4 Effect of electrode geometry and electrical energy deposited**

Varying parameters such as the energy deposited, the electrode gap distance, and electrode geometry has been found to have an impact on the flow induced at later times. Electrode gap distance was found to influence the number of vortices induced within the gap [12] while electrode geometry was found to affect the temperature distribution in the hot gas kernel [30]. Higher energy deposited in the electrode gap was found to result in wider spark channels [15], [39] and hotter gas temperatures within the electrode gap [40] which could result in stronger shock waves. In combustion studies using sparks, larger ignition kernels were observed for higher energy values and this was attributed to the underlying hydrodynamics of the spark induced flow [41]. A comparative study investigating the relationship between energy deposited in an electrode gap, by a single spark plasma discharge, and the strength of the shock wave, vortex ring circulation, rate of cooling, and other hydrodynamic quantities has not yet been done. Thus, the results of this work will clarify the relationships between these plasma and flow parameters and provide critical insight for development of future actuator designs.

### 1.3 Primary research objectives

The main aim of this investigation is to quantify and develop a better understanding of the flow induced due to a single spark discharge produced at standard atmospheric pressure and temperature. This goal is further divided into four main research objectives:

1. Study the cooling of the hot gas kernel and determine the extent of convective cooling.
  - i. Measure velocity and density using particle image velocimetry (PIV) and background oriented schlieren (BOS) experiments, respectively.
  - ii. Develop a cooling model using a control volume analysis of the energy equation to relate entrained fluid to cooling of the hot gas kernel.

*Manuscript title: Two regime cooling in flow induced by a spark discharge.*

2. Determine the role of the induced vortex rings in the entrainment and subsequent cooling of the hot gas kernel and evaluate the effect of energy on the cooling process.
  - i. Design simultaneous PIV and BOS experiments to study flow induced by a spark discharge for a range of energy values.
  - ii. Develop a vortex ring model relating flow entrained by a vortex ring to entrainment and cooling of the hot gas kernel.
  - iii. Evaluate the effect of energy deposited by the spark on the induced flow field.

*Manuscript title: Vortex rings drive entrainment and cooling in flow induced by a spark discharge.*

3. Estimate the role of the induced shock wave in the generation of the vortex ring vorticity.
  - i. Design a schlieren system to capture the evolution of the shock induced by a spark discharge.
  - ii. Use a model for the vorticity jump behind a curved shock to predict the vorticity generated in the spark.

*Manuscript title: Shock generated vorticity in spark discharges.*

4. Assess the symmetry of the vortex rings induced by a spark discharge, using time-resolved, tomographic PIV measurements.

## **1.4 Dissertation format**

This dissertation is divided into six chapters, with chapters 2-5 presenting a collection of research articles, addressing each research objective outlined in section 1.3. Chapter 2 investigates the coupling between the induced velocity field and the cooling of the hot gas kernel and develops a cooling ratio parameter to assess the role of entrainment in the cooling of the kernel. Chapter 3 builds on the cooling model presented in chapter 2 and presents the role of the induced vortex rings in the entrainment and convective cooling of the hot gas kernel, while also studying the effect of the electrical energy deposited in the electrode gap on the cooling process. Chapter 4 investigates the contribution of the shock wave induced at early times in generating the vorticity in the vortex rings that drive the cooling of the hot gas kernel. Chapter 5 presents the first steps towards 3D measurements of the induced velocity field using tomographic PIV to capture the induced vortex rings. Chapter 6, concludes the dissertation, providing a summary of chapters 2-5 along with recommendations for future research in the field.

## 2. TWO REGIME COOLING IN FLOW INDUCED BY A SPARK DISCHARGE

Bhavini Singh<sup>1</sup>, Lalit K. Rajendran<sup>1</sup>, Pavlos P. Vlachos<sup>2</sup>, and Sally P. M. Bane<sup>1</sup>

<sup>1</sup>*School of Aeronautics and Astronautics, Purdue University, West Lafayette, Indiana 47907, USA*

<sup>2</sup>*School of Mechanical Engineering, Purdue University, West Lafayette, Indiana 47907, USA*

This chapter has been previously published in *Physical Review Fluids*

DOI: 10.1103/PhysRevFluids.5.014501

### ***Abstract***

The cooling process associated with the flow induced by a spark plasma discharge generated between a pair of electrodes is measured using stereoscopic particle image velocimetry (S-PIV) and background oriented schlieren (BOS). Density measurements show that the hot gas kernel initially cools fast by convective cooling, followed by a slower cooling process. The cooling rates during the fast regime range from being 2 to 10 times those in the slower regime. An analytical model is developed to relate the cooling observed in the fast regime from BOS, to the total entrainment of cold ambient fluid per unit volume of the hot gas kernel, measured from S-PIV. The model calculates the cooling ratio to characterize the cooling process and shows that the cooling ratio estimated from the density measurements are in close agreement with those calculated from the entrainment. These measurements represent the first ever quantitative density and velocity measurements of the flow induced by a spark discharge and reveal the role of entrainment on the cooling of the hot gas kernel. These results underscore that convective cooling of the hot gas kernel, in the fast regime, leads to approximately 50% of the cooling and occurs within the first millisecond of the induced flow.

### **2.1 Introduction**

Plasma discharges are created by the breakdown of a gas in the presence of a strong electromagnetic field, leading to the formation of ionized species which are on average electrically neutral. These discharges have widespread applications in flow and combustion control, material

processing, biomedicine, nanotechnology, and environmental engineering [1]–[5]. In flow control applications, the discharges are typically used to induce localized heating and fluid motion to control and modify transport processes. The induced flow can be produced through an electrohydrodynamic mechanism such as in dielectric barrier discharge (DBD) actuators where a body force is generated due to the electric field thereby inducing a wall jet [3], [6], [8], [42], or via a thermal mechanism such as in spark discharge actuators.

Spark discharges are typically generated by raising the voltage difference between two electrodes, until the breakdown voltage is reached, resulting in ionization of gas in the electrode gap. The spark initiates a kernel of gas at very high temperature and pressure which then expands outward [10], producing a shock wave that lasts on the order of a few microseconds, which then gives rise to a transient three-dimensional flow field [30]. The flow induced by spark discharges have been the focus of a few computational studies [12]–[14] as well as some experimental investigations, e.g., [16], [41]. Computations on the flow induced by a single spark have thus far been restricted to the very early stages ( $< 100 \mu\text{s}$ ) of flow development [24]. While these studies showed the presence of a torus-shaped hot gas kernel and a weak shock, the development of the kernel in the post shock phase of the flow, and the associated heat, mass and momentum transport mechanisms have not been characterized. Experimental results of the late stages of the flow induced by sparks have been restricted to qualitative descriptions of the flow field [11], [16], [43], primarily due to difficulties associated with measuring such a transient and highly complex flow field with sufficient spatiotemporal resolution. Some of the first experimental results presenting quantitative information on the flow induced by microsecond-duration sparks [17] have shown the presence of a pair of vortex rings around the hot gas kernel for 5 mm and 8 mm electrode gap distances. In addition, these experiments revealed, jets of surrounding gas entrained into the electrode gap, and the circulation of the vortex rings as well as the rate of entrainment was found to decay over time. The rates of decay were similar for both electrode gaps, when non-dimensionalized using the electrode gap distance and velocity induced behind the shock produced by the spark.

While spark plasma discharges are being applied for various flow control and combustion applications [20]–[22], a detailed characterization of the flow induced by these discharges under quiescent conditions is still lacking. For example, recent work on the applications of nanosecond

repetitively pulsed (NRP) discharges to ignition have shown that the pulse frequency and number of pulses have a distinct effect on the size of the flame kernel, and this effect was attributed to a possible coupling between the characteristic recirculation time from the induced flow and the interpulse time interval [25], [44]. Detailed quantitative characterization of the flow induced by these discharges under quiescent conditions is a necessary step in characterizing these actuators to enable informed actuator designs, tailored to specific applications.

The purpose of this paper is to explain the cooling process observed in spark plasma discharge induced flow fields. This will be done by characterizing the flow induced by a single nanosecond-scale spark discharge using high speed stereo Particle Image Velocimetry (S-PIV) and Background Oriented Schlieren (BOS) to obtain velocity and density measurements in the post-shock phase of the induced flow. Using density information from the BOS measurements, it will be shown that there are two distinct cooling regimes of the spark-induced hot gas kernel with significantly different cooling rates. Further, the cold ambient gas entrained into the electrode gap leads to a bulk of the cooling of the hot gas kernel in the first regime. To assess this effect, a model is developed to relate the cooling rate of the hot gas kernel to the volume of the entrained fluid. The measurements show good agreement with the model within the limits of experimental uncertainty.

## **2.2 Experimental methods and techniques**

To investigate the flow induced by a spark plasma, two separate but complementary experiments were conducted. In the first test, velocity measurements of the flow induced by a nanosecond spark discharge were obtained using stereoscopic particle image velocimetry (S-PIV) measurements, and in the second the density of the hot gas kernel was measured under the same spark generating conditions, using background oriented schlieren (BOS). In each test, 25 runs were conducted, i.e. 25 separate spark plasma discharges were measured. Each run was spaced out in time such that there were no residual flow effects from one spark event to the next, that is, each run was at least 30 seconds apart. Voltage and current measurements were taken with each run.

### 2.2.1 Plasma generation – pulser and electrode description

A nanosecond high voltage pulse generator from Eagle Harbor Technologies was used to generate a spark discharge between two electrodes. The pulse parameters of the pulse generator can be independently varied, with peak voltages up to 25 kV, pulse durations from 20 to 110 ns, and pulse repetition frequencies (PRF) up to 400 kHz. The electrodes, shown in Figure 2.1, were machined out of ceriated-tungsten and had cone shaped tips with radius of curvature of approximately 150  $\mu\text{m}$  to enhance the electric field and aid in breakdown. The electrodes were separated by 5 mm in atmospheric, quiescent air. The voltage and current across the electrode gap during breakdown and spark discharge were measured using two Tektronix P6015A high voltage probes (in a differential measurement configuration) and a Magnelab CT-D1.0 current transformer, respectively. These measurements were used to calculate the electrical energy deposited in the plasma, which is the integral of the product of the voltage and current measurements over the pulse duration, as shown in Figure 2.1 (c). The electrical energy deposited in the plasma ranged from 4 mJ to 7 mJ.

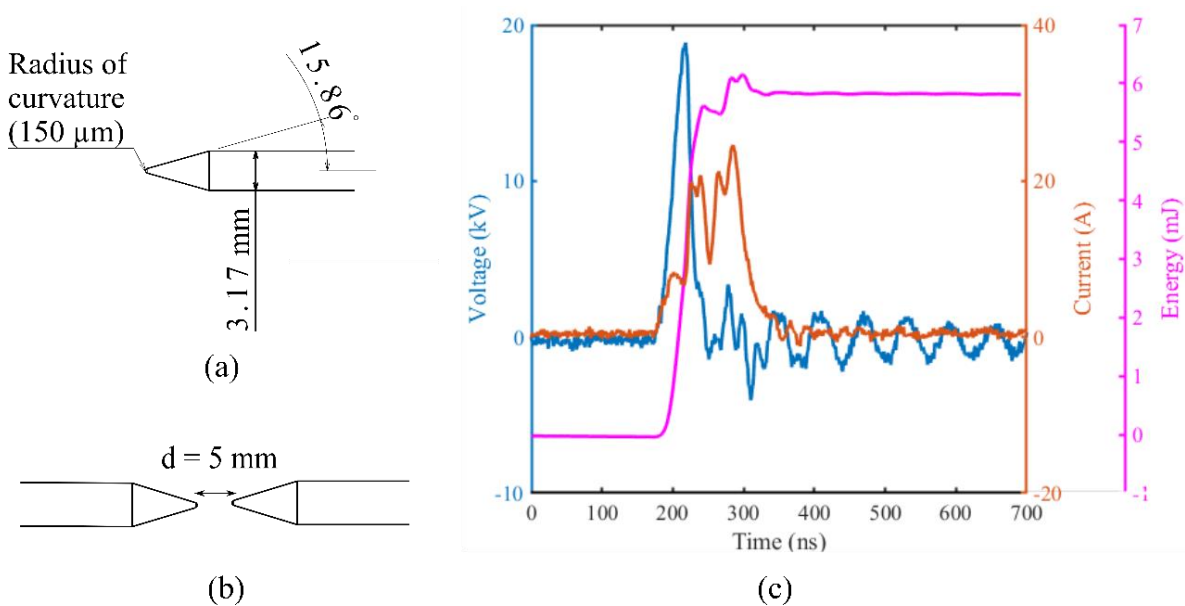


Figure 2.1: (a) Sketch of the cone-tipped electrode, (b) the two-electrode configuration used for plasma generation, and (c) sample current, voltage and energy waveform produced during a spark discharge in a 5 mm electrode gap.

## 2.2.2 Stereoscopic Particle Image Velocimetry

### 2.2.2.1 Experimental Setup

A schematic of the stereoscopic particle image velocimetry (S-PIV) system used to analyze the flow field is shown in Figure 2.2. The main components of the set-up include a Q-switched, double pulsed EdgeWave Nd: YAG laser which was operated at 10 kHz with pulse separation of 30  $\mu$ s, two high speed cameras (Photron SA-Z camera and Phantom v2512), and an acrylic test section measuring 190.5 x 140 x 152 mm, containing the electrodes. The laser sheet optics produced an approximately 1 mm thin waist in the region of interest where the spark discharge was generated. A Quantum Composer Model 575 delay generator and La Vision high speed controller were used to synchronize and trigger the laser, cameras, and high voltage pulse generator. The Photron and Phantom cameras with Nikon Nikorr 105 mm lenses were used to record particle images at 20,000 fps (corresponding to an image pair sampling rate of 10 kHz). The resolutions for the two cameras were 1024 x 1024 pixels for the Photron and 1280 x 800 pixels for the Phantom, with approximate fields of view of 10 x 10 mm and 20 x 13 mm, respectively. The included angle between the two cameras was 40°. A fluidized bed seeder was used to inject aluminum oxide particles with diameters of about 0.3  $\mu$ m and estimated Stokes number of approximately 0.002 into the test section.

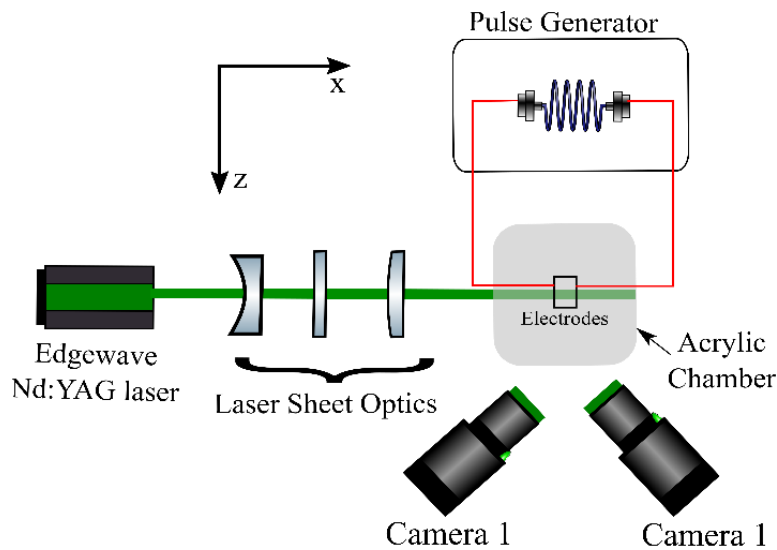


Figure 2.2: Schematic of the experimental set-up for S-PIV measurements of the plasma-induced flow field.

### 2.2.2.2 Image Processing

PRANA (PIV, Research and ANALysis) software (<https://github.com/aether-lab/prana>) developed by Vlachos and coworkers at Virginia Tech and Purdue University was used to process the recorded particle images. For the S-PIV measurements, a calibration was first performed to calculate the mapping function of the camera. The camera coordinates and physical coordinates were fitted using a least squares polynomial with cubic dependence in the x and y directions and quadratic dependence in the z direction [45]. A self-calibration procedure [46] was then followed to account for misalignment between the calibration target and the plane of the laser sheet, and the mapping function was corrected accordingly. With the new mapping function and calibration information, the individual camera images from each camera were dewarped onto a common grid and cross correlated to yield particle displacement values [47]. The correlation method used was the Robust Phase Correlation (RPC) [48]–[50] in an iterative multigrid framework using window deformation [51]–[54], with each pass validated by universal outlier detection (UOD) [55]. A total of four passes were used and a 50% Gaussian window was applied to the original window size [49] resulting in window resolutions of 64x64 pixels in the first pass to 32x32 pixels in the last pass, with 50 % window overlap in all passes. Between successive passes, velocity interpolation was performed using bicubic interpolation and the image interpolation was performed using a sinc interpolation with a Blackman filter. Finally, subpixel displacement was estimated using a three-point Gaussian fit [56]. The projected velocity fields calculated in this manner were then combined with the camera angle information obtained from calibration to yield the three components of velocity in the measurement plane [57]. Proper orthogonal decomposition with the entropy line fit (ELF) method [58] was used to denoise the PIV velocity fields. The spatial resolution for velocity calculations was 0.32 mm and each snapshot contains 50 x 64 vectors.

### 2.2.2.3 Uncertainty quantification

Experimental uncertainties vary in space and time, and are unique to each experiment [59]. Various a-posteriori methods have been developed to quantify systematic and random uncertainty bounds in PIV measurements, grouped into indirect methods [60]–[62] and direct methods [63]–[65] of uncertainty quantification. Experimental uncertainties in the S-PIV measurements were propagated according to the procedure outlined by Bhattacharya *et al* [66]. Uncertainties in the

planar velocity fields were calculated using Image Matching (IM) [64] which uses the position disparity between particle pairs in the two images at the end of a converged deformation processing to estimate the uncertainty in the displacement value. IM was used as it is a direct method and these have been shown to be more sensitive to elemental error sources [67]. However, the IM method has some drawbacks due to its reliance on pairing of individual particle images which can be imprecise in highly seeded images or can be inaccurate due to out of plane motion [59]. Any of the other direct uncertainty quantification methods could be used though each method has its own drawbacks and planar PIV uncertainty quantification is an active area of research. These uncertainties were then propagated through the stereo reconstruction by combining uncertainties in the planar velocity field with positional uncertainties calculated from the disparity map obtained after the self-calibration procedure and uncertainties in the camera angles, to calculate uncertainty in the reconstructed velocity field. Maximum uncertainties in the three components of velocity ( $u$ ,  $v$  and  $w$ ) were approximately 0.04 m/s, 0.03 m/s and 0.09 m/s, corresponding to 1.2%, 1% and 3% of the maximum velocity (3 m/s), respectively.

## **2.2.3 Background Oriented Schlieren**

### **2.2.3.1 Experimental Setup**

Background Oriented Schlieren (BOS) was used to measure density gradients in the post-discharge flow by tracking the apparent distortion of a target dot pattern. The dot pattern was generated by illuminating a block of sand-blasted aluminum with a 150 W xenon arc lamp (Newport 66907), and the images were captured at 20 kHz using a Photron SA-Z camera with a 105 mm Nikon lens with an  $f\#$  of 11 and a 2X tele-converter for an approximate field of view of 14 x 14 mm. A schematic of the BOS system is shown in Figure 2.3. The distance from the center of the electrodes to the BOS target ( $Z_D$ ) was approximately 57 mm and the distance from the center of the electrodes to the camera ( $Z_A$ ) was approximately 152 mm.

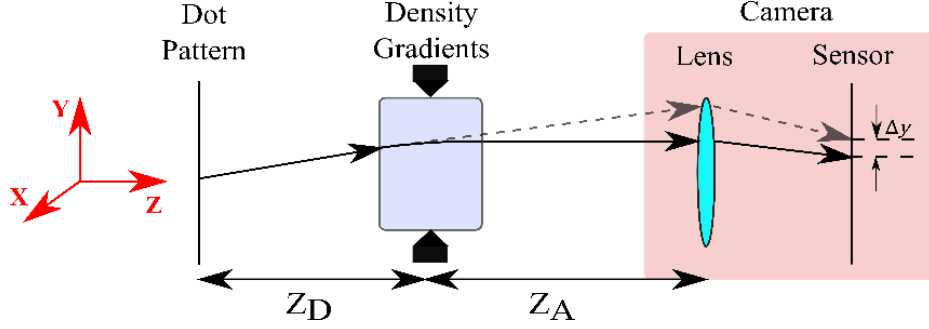


Figure 2.3: Experimental schematic of the primary components of the BOS system.

### 2.2.3.2 Image Processing

The distortion of the dot pattern is estimated by cross-correlating an image taken with the flow to a reference image taken without the flow. The images were processed using the same approach and software (PRANA) as for the S-PIV measurements. The correlation method used was the Robust Phase Correlation (RPC) [48]–[50] in an iterative multigrid framework using window deformation [51]–[54]. Each pass was validated by universal outlier detection (UOD) [55]. A total of four passes were used with window resolutions of 64x64 pixels in the first pass to 32x32 pixels in the last pass, with 50 % window overlap in all passes. Subpixel displacement was estimated using a three-point Gaussian fit [56]. The spatial resolution of the final pass was 0.2 mm and each snapshot contains 22 x 55 vectors.

The pixel displacements obtained from the cross-correlation analysis were then used to calculate the projected density gradient field [68],

$$\frac{\partial \rho_p}{\partial x} = \int \frac{\partial \rho}{\partial x} dz = \frac{\Delta x}{Z_D M} \frac{n_0}{K} \quad (2.1a)$$

$$\frac{\partial \rho_p}{\partial y} = \int \frac{\partial \rho}{\partial y} dz = \frac{\Delta y}{Z_D M} \frac{n_0}{K} \quad (2.1b)$$

where  $\partial \rho / \partial x$  is the density gradient along the  $x$  direction,  $\rho_p = \int \rho dz$  is the projected density field,  $\Delta x$  is the pixel displacement on the camera sensor,  $M$  is the magnification,  $Z_D$  is the distance between the mid-plane of the density gradient and the dot pattern,  $n_0$  is the refractive index of the undisturbed medium, and  $K$  is the Gladstone-Dale constant.

The projected density field  $\rho_p(x, y)$  was calculated by 2D integration, on solving the Poisson equation given by:

$$\frac{\partial^2 \rho_p}{\partial x^2} + \frac{\partial^2 \rho_p}{\partial y^2} = S(x, y) \quad (2.2)$$

The source term  $S$  is calculated as

$$\bar{\bar{S}} = \bar{\bar{V}}_x \overline{\frac{\partial \rho_p}{\partial x}} + \bar{\bar{V}}_y \overline{\frac{\partial \rho_p}{\partial y}} \quad (2.3)$$

where  $\bar{\bar{V}}_x, \bar{\bar{V}}_y$  are the discretized gradient operators (matrices represented by a double overbar) that depend on the finite difference scheme, and  $\overline{\frac{\partial \rho_p}{\partial x}}, \overline{\frac{\partial \rho_p}{\partial y}}$  are the measured density gradients and are calculated from 2.1(a)-(b). (1D column vector represented by a single overbar). A second order central difference discretization scheme is used for the results reported in this paper.

Dirichlet boundary conditions were used on the left and right boundary, with  $\rho_p = 0$  at the edges since there was no flow due to the spark in these regions. The field of view was chosen to be about one electrode gap along the radial direction on each side, such that the left and right boundaries were far enough from the discharge to justify this boundary condition. At the top boundaries, the displacements obtained from the cross-correlation were integrated along the boundaries starting from the left and right corners with a known  $\rho_p$  to set up an *artificial* Dirichlet boundary condition. The Poisson equation was solved by matrix inversion using sparse linear operators as described in [69] to obtain the final projected density field.

Finally, the actual density field  $\rho(r, z)$  was calculated from the projected density field by Abel inversion under the assumption that the flow was approximately axisymmetric [70]. This was a reasonable assumption in this problem because the geometry is axisymmetric. However, given that the spark channel may not be axisymmetric, the post-discharge flow may deviate from perfect axisymmetry, and this is a possible source of error in these measurements.

For the 2D axisymmetric field shown in Figure 2.4, the Abel inversion equation is given by,

$$\rho(r) = -\frac{1}{\pi} \int_r^\infty \frac{d\rho_p}{dx} \frac{dx}{\sqrt{x^2 - r^2}} \quad (2.3)$$

and can be used to calculate a 2D axisymmetric field  $\rho(r)$  from a 1D projection  $\rho_p(x)$ . Since the BOS measurements are 2D projections, this procedure was sequentially applied for each horizontal row of measurements to reconstruct 2D slices of the full 3D axisymmetric flow field.

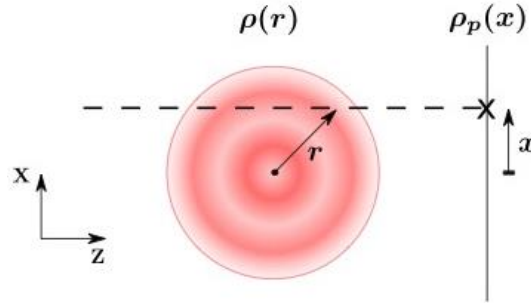


Figure 2.4: Projection of a 2D axisymmetric field.

### 2.2.3.3 Uncertainty quantification

Experimental uncertainties in the BOS measurements were propagated through the complete density reconstruction according to [71]. Uncertainties in the displacement field were calculated using Image Matching [64], then propagated through the optical layout followed by the Poisson solver to obtain uncertainty in the projected density field. The uncertainties were then propagated through the Abel inversion to obtain total uncertainty in the density field. Maximum uncertainties in the density field were approximately 0.01 kg/m<sup>3</sup>, corresponding to 0.01% of ambient density (1.225 kg/m<sup>3</sup>).

### 2.2.4 Post processing metrics

The measured velocity and density fields were used to calculate additional quantities and metrics to characterize the induced flow. From the velocity field obtained using S-PIV measurements, the vorticity field was calculated using a 4th order compact noise optimized Richardson extrapolation scheme [72]. The coherent structures in this vorticity field were then identified using swirl strength, using the  $\lambda_{ci}$  method [73]. All swirl values that were at least 5% of the maximum swirl strength and had a specified minimum area were considered coherent structures. The area of each coherent structure was calculated as the sum of all grid points identified as part of that structure. Then,

assuming that the coherent structures are perfectly circular, an effective radius was calculated. The centroids of the cores are the barycenter of the calculated area, weighted by  $\lambda_{ci}$  values.

From the calculated density field, the kernel is identified as any region of density that is lower than 95% of ambient density (1.225 kg/m<sup>3</sup>). The mean density at a single snapshot was calculated by summing all the density values in the identified kernel and dividing this by the number of points in the kernel.

### 2.2.5 Non-dimensionalization

Results were non-dimensionalized similar to prior work [17] using the velocity induced behind the shock wave produced by the spark expansion. The shock was assumed to be weak [28], [29] and the weak shock solution for the pressure jump across a shock, developed by Jones *et al* [74], was used:

$$\frac{p_2 - p_1}{p_1} = \frac{2\gamma}{\gamma + 1} \frac{0.4503}{(1 + 4.803(r/R_0)^2)^{\frac{3}{8}} - 1} \quad (2.4)$$

where the subscripts 1 and 2 represent conditions upstream and downstream the shock, respectively. The quantity  $p$  represents pressure, and  $r$  is the radial distance at which flow properties behind the shock are measured. In the present context, the radial distance was considered to be the electrode gap distance (5 mm). The variable  $R_0$  is the characteristic radius determined by the initial conditions, and is given by:

$$R_0 = \left[ \frac{4E_0}{3.94\gamma p_1} \right]^{\frac{1}{2}} \quad (2.5)$$

where  $E_0$  is the energy deposited by the plasma per unit length of the electrode gap and  $\gamma$  is the ratio of specific heats (taken to be 1.4 for air). Using these equations, the upstream Mach number and the shock speed were determined, and then the normal shock relations were used to calculate the induced velocity and density behind the shock. All measurements were non-dimensionalized using this induced velocity ( $u_{shock}$ ) and density ( $\rho_{shock}$ ) behind the shock and the characteristic length ( $d$ ) which is considered to be the electrode gap distance (5 mm). The velocity and length scales were then used to define a characteristic time scale ( $\tau$ ) as the electrode gap distance ( $d$ ) divided by the velocity induced behind the shock. For the maximum energy value of 7 mJ,  $u_{shock}$ ,

$\rho_{shock}$  and  $\tau$  are 71 m/s, 1.45 kg/m<sup>3</sup> and 0.07 ms, respectively, and for the minimum energy value of 4 mJ, they are 54 m/s, 1.42 kg/m<sup>3</sup> and 0.09 ms respectively.

## 2.3 Results and Discussion

### 2.3.1 Observations from experimental results

An example of the flow field induced after a single spark discharge generated under quiescent conditions, in a 5 mm electrode gap and corresponding to deposited energy of 5.8 mJ, whose waveform is shown in Figure 2.1(c), is presented in Figure 2.5. The flow is initially dominated by the formation of a thin region of hot gas in the gap between the two electrodes, the formation of a shock wave and its subsequent radial expansion, all within less than 30  $\mu$ s ( $t/\tau < 1$ ) [29]. The flow field continues to evolve, and the measurements reported in this study are collected approximately 100  $\mu$ s ( $t/\tau > 1$ ) after the discharge, by which time the shock has departed the field of view. At  $t/\tau = 1.9$ , a cylindrical shaped gas kernel exists within the electrode gap as seen in the density measurements shown in Figure 2.5 and the density of the gas kernel is lower than the ambient, with  $\rho/\rho_{shock} = 0.3$  (~40% of the ambient density). This hot gas kernel expands while simultaneously cooling over time, changing in shape from cylindrical, to the characteristic toroidal shape previously observed in visualization studies of flow induced by sparks [13], [16]. The hot gas kernel continues to cool over time until its density eventually equilibrates to the ambient.

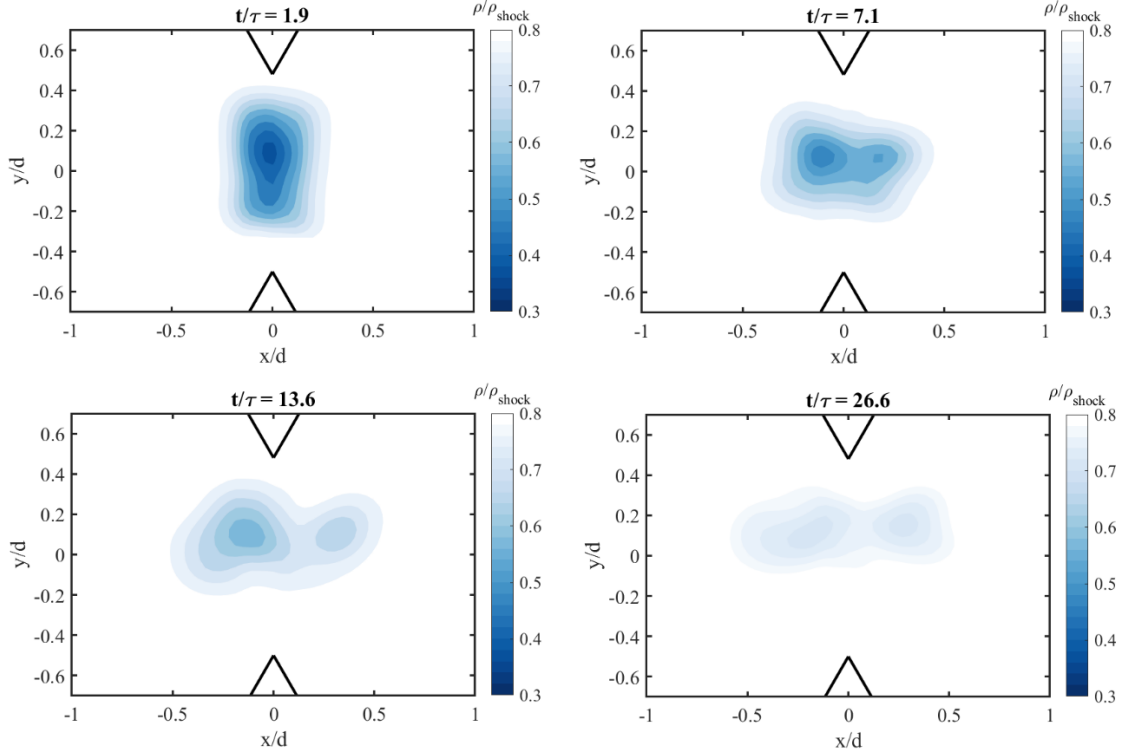


Figure 2.5: Time evolution of the density of the hot gas kernel from  $t/\tau = 1.9$  (0.15 ms) to 26.6 (2.05 ms) obtained from BOS measurements. The measurements show minimum kernel densities ( $\rho/\rho_{shock}$ ) as low as 0.3 and the evolution of the kernel shape from cylindrical to toroidal shape for a single test where  $\rho_{shock} = 1.47 \text{ kg/m}^3$  and  $\tau = 0.08 \text{ ms}$ .

The mean density of all points lying within the hot gas kernel is computed, and a time history of the mean kernel density is shown in Figure 2.6(a). We observe an initial rapid increase in density from  $\rho/\rho_{shock} = 0.64$  to 0.75, followed by a slower increase in density. The increase in density represents a cooling of the hot gas kernel, and the two stages of cooling both show linear increase in density. For the current test, we see that the rate of cooling in the first stage ( $m_{fast}$ ) is nearly 5 times larger than in the second stage ( $m_{slow}$ ), and the changeover ( $t_{cp}$ ) from the first stage to the second occurs at  $t/\tau = 8.8$ .

This analysis is repeated for all 25 BOS experiments and the results are shown in Figure 2.6(b). We find that for each experiment two cooling regimes are present, a fast cooling regime and a slow cooling regime. Figure 2.6(b) also shows that for the spark energy ranges considered herein, the rates of cooling in the first (fast) regime are higher, by at least a factor of 2, than in the second,

slow regime. In addition, neither the fast nor slow cooling rates display a clear dependence on the energy deposited in the gas by the discharge plasma.

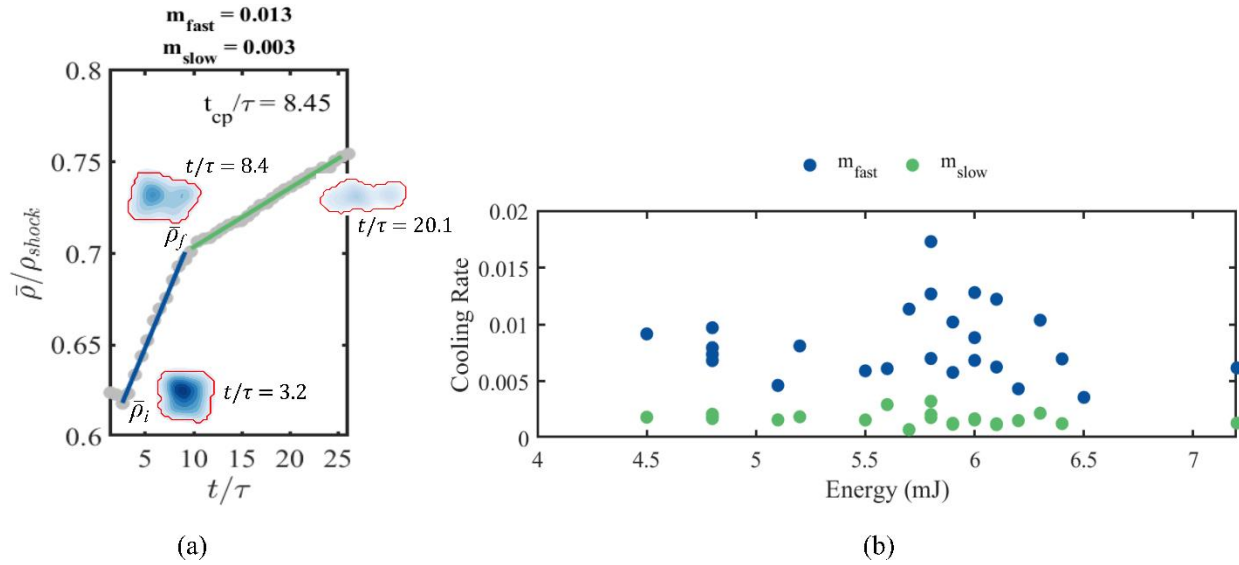


Figure 2.6: (a) Time history of mean kernel density inside BOS control volume, for the same test as in Figure 2.5, showing presence of two cooling regimes, each with different rates of cooling, with inset of identified kernel control volume from BOS data at  $t/\tau$  values of 3.2, 8.4 and 20.1 (b) fast and slow cooling rates for all tests, showing no dependence on energy deposited.

Researchers have in the past hypothesized that the shape and density of the hot gas kernel is strongly coupled to the velocity field induced due to the spark [16]. Figure 2.7, shows an example of the vorticity field of the induced flow due to a single spark corresponding to deposited energy of 6.8 mJ. A pair of vortex rings are present near the electrode tips whose vortex cores are outlined by black circles and whose weighted centroids are represented by the filled circles contained inside the cores. Vortex trajectories of the pair of vortex rings in Figure 2.8(a) show that these migrate towards each other in the y-direction due to self-induction until they eventually collide [75]. As the rings get closer, the ring radii increase as shown by the time history of the mean ring radii of the top and bottom rings in Figure 2.8(b). This increase in ring radii could be due to the combined effects of mutual induction and viscosity, although the rate of increase due to viscosity would be much slower, on the order of  $1e-3$  m/s ( $\nu/d$ , where  $\nu$  is assumed to be  $1.48e-5$ , the kinematic viscosity of air and  $d$  is the electrode gap distance, 5 mm) compared to the rate of increase in ring radii observed in the experiments which are on the order of 1 m/s. The mean circulation of both

rings also continues to decay post collision as shown by the time history plot of circulation in Figure 2.8(b). Figure 2.9 shows the collision time of the vortex rings from S-PIV and the changeover time ( $t_{cp}$ ) in the cooling rates measured from BOS. For the experiments considered, the median collision time in PIV is  $t/\tau = 11.6$  and the median changeover time in BOS is  $t/\tau = 10.4$ .

As previously noted from the BOS data, all 25 tests showed that the hot gas kernel cools over time in two distinct cooling regimes. Similarly, all 25 S-PIV tests showed significant entrainment of ambient gas into the electrode gap, which may be responsible for the cooling observed in BOS. Based on these observations, we hypothesize that the entrained ambient fluid mixes with the hot gas kernel, and therefore the entrainment drives the cooling of the hot gas kernel. A model of the cooling process based on this hypothesis, is developed and tested in the following section.

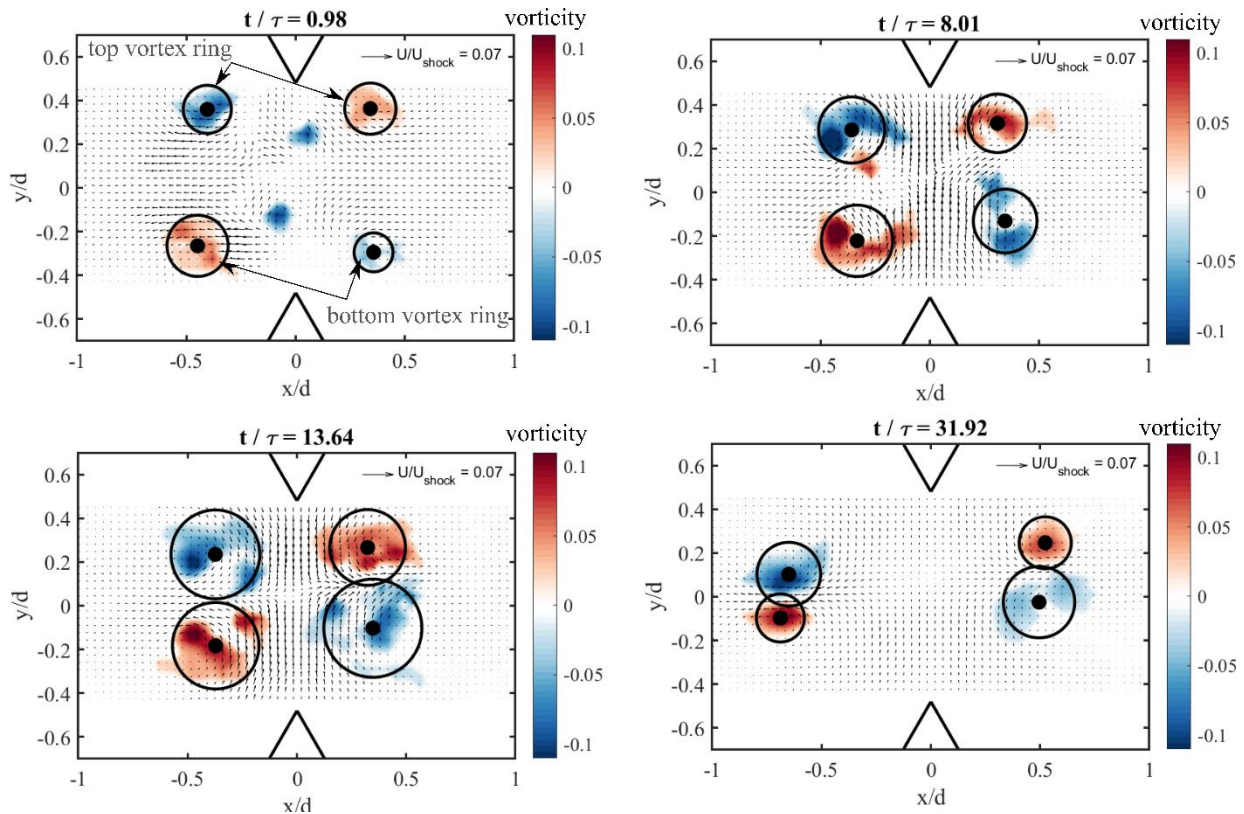


Figure 2.7: Coherent vorticity induced by the spark from  $t/\tau = 0.98$  (0.07 ms) to 27.7 (2.0 ms) obtained from PIV measurements. The results show motion of a pair of vortex rings towards each other and collision of the vortex rings followed by decay, for a single test where  $u_{shock} = 66 \text{ m/s}$  and  $\tau = 0.07 \text{ ms}$ .

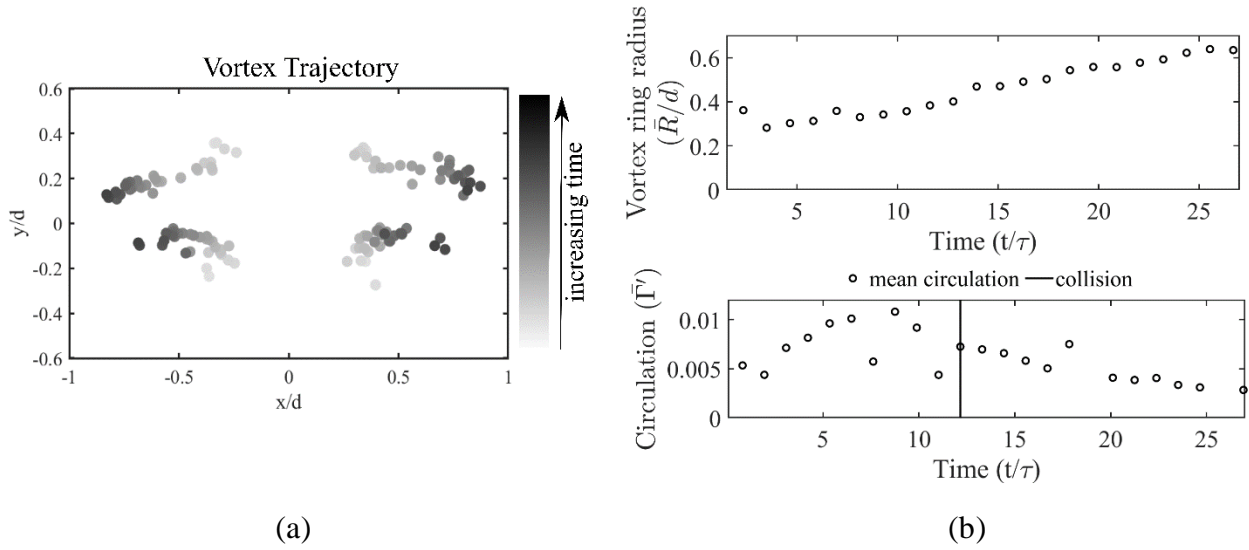


Figure 2.8: (a) Map of vortex trajectories showing motion towards  $y/d = 0$  and simultaneous radial expansion in  $x$ . (b) Time history of mean radius of top and bottom vortex rings showing overall expansion and time history of mean circulation showing decay post collision of the vortex rings.

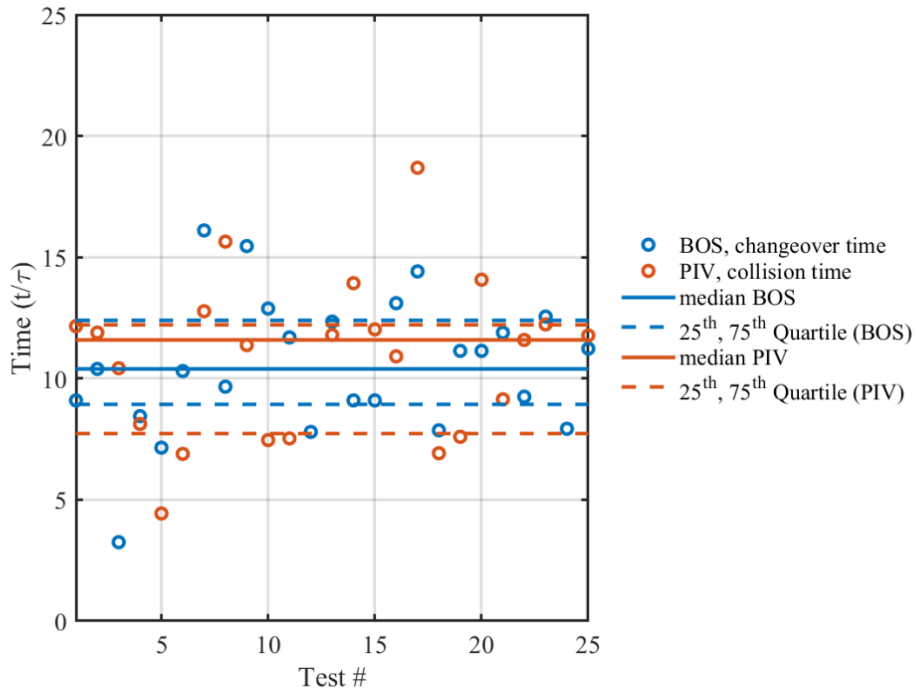


Figure 2.9: Comparison of cooling regime changeover points obtained from BOS with vortex ring collision times obtained from PIV. Quartiles of changeover points from the fast cooling to slow cooling range between  $t/\tau = 8.9$  and  $12.4$  for BOS and quartiles of collision times range between  $t/\tau = 7.7$  and  $12.2$  for PIV.

### 2.3.2 A model for the effect of cold gas entrainment on the kernel cooling process

In order to test the hypothesis that entrainment of cold ambient gas is responsible for cooling of the hot gas kernel in the fast regime, a model is developed to relate the total cooling of the hot gas kernel to the volume of entrained fluid within a control volume representing the kernel. A pair of vortex rings is induced near each electrode tip and the PIV control volume is defined between the centroids of the cores of the vortex rings; details on this control volume definition will be provided in the following section. Cold ambient gas is entrained into the control volume, cooling the hot gas kernel.

The cooling process can be characterized by considering the rate of change of enthalpy of the kernel, with the simplifying assumption that the fluid is inviscid, thereby neglecting work done by viscous forces. Further neglecting body forces and heat transfer due to conduction and radiation, enables the simplification of the total energy budget to the following equation,

$$\frac{d}{dt} \int_V (\rho h_0) dV + \iint \rho h_0 \vec{u} \cdot \vec{n} dS = 0 \quad (2.6)$$

where  $h_0$  is the stagnation (or total) enthalpy in the control volume and given by  $h_0 \equiv e + \frac{P}{\rho} + \frac{1}{2} \vec{u} \cdot \vec{u}$ . Here  $e$  is internal energy (per unit mass),  $\frac{P}{\rho}$  is work done due to pressure forces and  $\frac{1}{2} \vec{u} \cdot \vec{u}$  is the kinetic energy (per unit mass).

Assuming a calorically perfect gas, the energy equation can be further simplified to

$$\frac{d}{dt} (m c_p T) = \rho_{in} c_p T_{in} \dot{V}_{in} - \rho_{out} c_p T_{out} \dot{V}_{out} \quad (2.7)$$

where  $m$  is the mass of the hot gas kernel,  $c_p$  is the specific heat capacity at constant pressure, and  $T$  is the temperature of the hot gas kernel. Further,  $\rho_{in}$  and  $T_{in}$  represent the density and temperature of ambient fluid entering the control volume and conversely  $\rho_{out}$  and  $T_{out}$  are the density and temperature of fluid exiting the control volume. Finally,  $\dot{V}_{in}$  and  $\dot{V}_{out}$  denote the entrainment (influx) and detrainment (efflux), respectively.

The energy equation can be simplified even further by employing additional assumptions about the flow field. Making the low Mach number assumption, we imply that changes in density are

only due to changes in temperature (as the cooling process occurs long after the shock has departed the field of view) and that  $\dot{V}_{in} = \dot{V}_{out}$ . On considering air to be a perfect gas ( $P = \rho RT$ ), changes in temperature due to pressure in the control volume are negligible. The temperature of the entrained ambient fluid is considered to be constant and at the ambient temperature under the assumption of an infinite reservoir of cold gas ( $T_{in} = T_{\infty} = const$ ) in relation to the size of the control volume. It is also assumed that the entrained fluid mixes perfectly with the gas inside the kernel, and therefore the temperature of the fluid leaving the control volume,  $T_{out}$ , is considered to be equal to the temperature of the kernel,  $T$ .

Under these assumptions, the energy equation can be further simplified to,

$$\frac{d}{dt} \left( m \frac{P}{\rho R} \right) = \dot{V}_{in} \left( \rho_{\infty} \frac{P}{\rho_{\infty} R} - \rho \frac{P}{\rho R} \right) \quad (2.8)$$

The right-hand side of Equation 2.8 goes to 0, giving,

$$\frac{1}{\rho} \frac{d}{dt} (m) - \frac{V_{cv}}{\rho} \frac{d\rho}{dt} = 0 \quad (2.9)$$

Here  $V_{cv}$  is the volume of the control volume defined between the centroids of the coherent structures, as described in the following section. Further, we write the continuity equation,

$$\frac{d}{dt} \int_V \rho dV + \iint \rho \vec{u} \cdot \vec{n} dS = 0 \quad (2.10)$$

Evaluating the volume integrals gives,

$$\frac{d}{dt} (m) = \rho_{\infty} \dot{V}_{in} - \rho \dot{V}_{out} = \dot{V}_{in} (\rho_{\infty} - \rho) \quad (2.11)$$

Using Equations 2.9 and 2.11, the energy equation can be further simplified to relate the rate of change of density of the kernel to the entrainment, and is given by,

$$\frac{1}{(\rho_{\infty} - \rho)} \frac{d\rho}{dt} = \frac{\dot{V}_{in}}{V_{cv}} \quad (2.12)$$

where the left-hand side of the equation is obtained from BOS measurements and the right-hand side is obtained from the S-PIV measurements.

Thus, the change in the mean kernel density can be calculated by integrating each side of the equation,

$$\int_{\bar{\rho}_i}^{\bar{\rho}_f} \frac{d\rho}{\rho - \rho_\infty} = \int_{t_i}^{t_{collision}} \frac{\dot{V}_{in}}{V_{cv}} dt \quad (2.13)$$

where the integral on the left represents the total change in kernel density (the cooling effect) observed in the fast regime of the experiment, integrated from the initial mean kernel density (minimum of time history of mean kernel density) to the density at the changeover point, and the right-hand side represents the total amount of cold gas that is entrained as a fraction of the volume of the hot gas kernel, integrated from time  $t/\tau > 3$ , corresponding on average to the time of minimum density from BOS, to the time of collision. A metric termed the *cooling ratio* is introduced at this point and is obtained by further subtracting both sides of the equation from 1, as given by Equation 2.13:

$$\left( \frac{\bar{\rho}_f - \bar{\rho}_i}{\rho_\infty - \bar{\rho}_i} \right) = 1 - \exp \left( - \int_{t_i}^{t_{collision}} \frac{\dot{V}_{in}}{V_{cv}} dt \right) \quad (2.14)$$

It can be observed from the equation that for a fixed initial density  $\bar{\rho}_i$ , as the final density of the kernel  $\bar{\rho}_f$  approaches the ambient density  $\rho_\infty$ , the ratio on the left-hand side of the equation (the ‘cooling ratio’) approaches 1. Therefore, the cooling ratio represents the extent of completion of the cooling process, and the closer its value is to 1, the more complete the cooling process.

### 2.3.3 Calculation of parameters in the cooling model

As stated earlier, the two sides of Equation 2.14 will be estimated from separate measurements, with the left-hand side evaluated using the density measurements from BOS, and the right-hand side using velocity measurements from S-PIV. One of the limitations of this calculation procedure is that the measurements are not simultaneous, and since the spark discharge is a chaotic process which is very sensitive to initial conditions (such as the electrode tip geometry and surface roughness), each realization of the spark induced flow field will be different. Our objective in this study is to therefore perform a statistical analysis of the quantities on the two sides of the equation and assess their agreement.

To facilitate this comparison, we denote the cooling ratio on the left-hand side of Equation 2.14 as  $\kappa_{BOS}$ , and is defined by:

$$\kappa_{BOS} = \left( \frac{\bar{\rho}_f - \bar{\rho}_i}{\rho_\infty - \bar{\rho}_i} \right) \quad (2.15)$$

Similarly, the term on the right hand side of the equation is denoted by  $\kappa_{PIV}$ , and is defined by:

$$\kappa_{PIV} = 1 - \exp \left( - \int_{t_i}^{t_{collision}} \frac{\dot{V}_{in}}{V_{cv}} dt \right) \quad (2.16)$$

In order to calculate the BOS cooling ratio  $\kappa_{BOS}$ , the initial ( $\bar{\rho}_i$ ) and final ( $\bar{\rho}_f$ ) densities in the fast cooling regime are determined from the time histories of the mean kernel density, as shown in Figure 2.6(a-b), note that these values are different from one test to another. The initial density is considered to be the absolute minimum mean density measured during the time series, while the final density is considered to be the density at the changeover time in BOS, which marks the transition from the fast to the slow cooling regime.

The term  $\kappa_{PIV}$  represents the total entrainment/volume flux into an arbitrary control volume ( $V_{cv}$ ) representing the hot gas kernel, here defined to be a polygon with the vertices located on the swirl strength weighted centroids of the coherent structures identified. Entrainment is calculated over the time period before vortex ring collision which marks the changeover from fast to slow cooling regimes in the S-PIV data. The velocity of the fluid relative to the control volume is used to calculate the entrainment, where the velocity of an edge of the control volume is calculated by taking a finite difference of the time history of each point along the boundary of the control volume. The velocity of the fluid at the edge of the control volume is calculated by interpolating the velocity measurements from the S-PIV grid on to the control volume edge of interest. This procedure is repeated for all edges of the control volume, and any influx of fluid is classified as entrainment. The volume of the control volume is defined as  $V_{cv} = \pi \frac{w^2}{4} h$ , where  $w$ , the width of the control volume, is defined as the mean of the width of the top and bottom boundaries, and  $h$ , the height, is defined as the mean y distance of the left and right control volume boundaries.

As the model described in this work is data-driven, and all measurements contain inherent uncertainties, it is essential to propagate these uncertainties in the raw measurements (velocities

and densities) through the calculation procedure associated with the cooling model. The uncertainties in the fundamental quantities such as the velocity and density are propagated through each quantity in the cooling ratio equation using the Taylor series based propagation method [76] to determine the final uncertainty in cooling ratios estimated from BOS and S-PIV. The uncertainties in cooling ratio from the BOS and S-PIV measurements ranged from 1% to 16% of the cooling ratio value, with the majority (~ 80%) of the cooling ratio uncertainties being less than 5% of their respective cooling ratio values. Details of the uncertainty propagation are provided in the appendix.

### **2.3.4 Results of the data driven cooling model**

The cooling ratios calculated from both S-PIV and BOS for all tests are shown in Figure 2.10. While there is considerable scatter in the estimates from both measurements, it is seen that the S-PIV cooling ratios are distributed about a median value of 0.41, while the BOS cooling ratios exhibit a median value of 0.39. The 25<sup>th</sup> and 75<sup>th</sup> quartiles show that these cooling ratio values range from 0.32 to 0.44 for BOS and from 0.3 to 0.51 for S-PIV. Given that the cooling ratio is a measure of the extent of cooling in the hot gas kernel, and a value of 1 indicates 100% cooling has occurred, these results imply that close to 30-50% of the cooling occurs in the fast regime which spans about a millisecond, and illustrates the rapid, convective nature of the cooling process. As seen from Figure 2.10, the cooling ratios separately calculated from BOS and S-PIV are statistically equivalent over the range of experiments considered in this work, thus supporting the hypothesis that the cooling of the kernel is governed by the entrainment of cold gas.

It is important to note, however, that diffusive effects will also play a role in the kernel cooling in the fast regime, albeit at a much slower rate. The scatter in the cooling ratio estimates arise from the variability of each experiment, due primarily to the stochastic nature of the spark. This therefore prevents an exact match of cooling ratios from the two experimental campaigns.

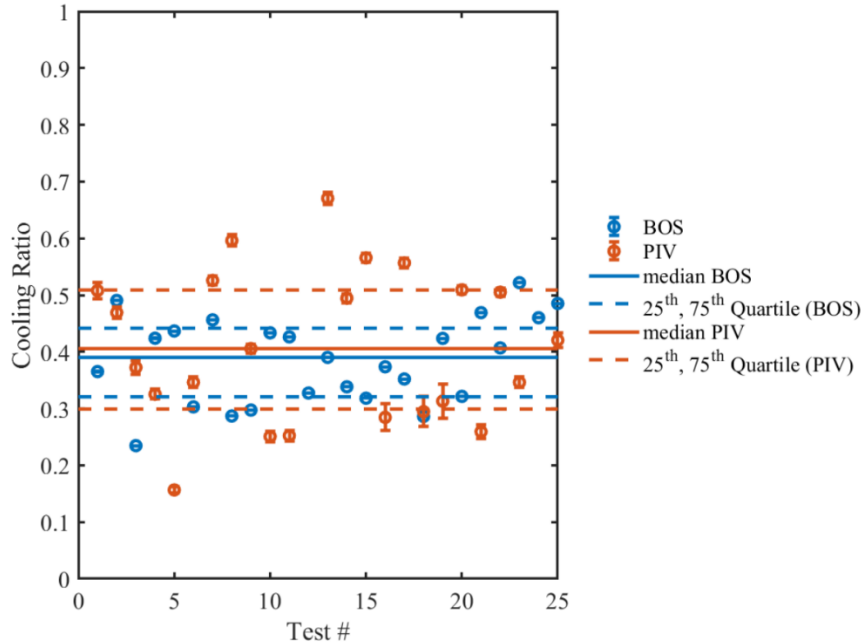


Figure 2.10: Cooling ratios calculated from S-PIV and BOS measurements show that in the fast regime, the total cooling effect observed from the kernel density measurement is statistically equivalent to the ratio measured from the cold gas entrained.

## 2.4 Conclusions

This work uses stereoscopic particle image velocimetry (S-PIV) and background oriented schlieren (BOS) measurements to characterize the flow induced by a spark generated between two conical shaped electrodes. The density field measured from BOS shows the cooling and expansion of an induced hot gas kernel, transforming in shape from an initially cylindrical region of hot gas to a torus shape, while simultaneously cooling to the ambient temperature/density. It was also observed that the cooling process, characterized by an increase in the mean kernel density, occurs in two stages: an initial fast, convective cooling regime on the order of a millisecond, followed by a slower cooling regime. Additionally, it was found that the rate of increase of density in the fast regime was at least twice as high as that in the slow regime for all 25 tests. The velocity measurements from S-PIV show the presence of a pair of vortex rings near each electrode tip and significant entrainment of fluid into the electrode gap. The vortex rings move towards each other and eventually collide, followed by the subsequent decay of vorticity.

Based on the observations, it is hypothesized that the entrainment of cold ambient gas drives the cooling of the hot gas kernel. In order to test this hypothesis, a simplified model of the cooling process was developed by considering the conservation of thermal energy inside a control volume representing the hot gas kernel. It is shown from the model that the rate of increase in density is directly proportional to the cold gas entrainment per unit volume of the kernel, and a metric termed the ‘cooling ratio’ was proposed to characterize the extent of this cooling process. From the point of view of the kernel density, the cooling ratio represents the ratio of the change in kernel density over the fast regime to the initial density deficit with respect to the ambient. From the point of view of entrainment, the cooling ratio represents the time integral of the entrainment of cold gas per unit volume of the hot gas kernel, over the duration of the fast regime.

The cooling model was tested by calculating the cooling ratio terms separately from the BOS and S-PIV measurements conducted over different experimental campaigns. The ratios were seen to be statistically equivalent within the limits imposed by the measurement uncertainty and the chaotic nature of the spark discharge, thereby confirming the hypothesis. The cooling ratios were distributed around median values of 0.39 and 0.41 for BOS and S-PIV respectively. This also implies that close to 30-50% of the cooling occurs in the fast regime which lasts just over a millisecond. This information can be used to inform the use of multiple pulses and pulse repetitive frequencies which aim to benefit from the synergetic effect of multiple plasma discharges [25], by ensuring that the frequency of these is always greater than  $1/t_{cp}$ . For the range of energies evaluated in these experiments, the frequencies needed to obtain synergetic effects between pulses have to be greater than 1 kHz. The cooling of the hot gas kernel also gives insight into the mixing process with the density representing passive scalar mixing. An initial driving velocity field during the entrainment process brings about significant mixing in the fast regime, resulting in cooling of the hot gas kernel. This would be beneficial when spark plasma discharges are used in combustible mixtures to improve combustion efficiency as well as reduce ignition delay.

Further improvements can be made to this analysis by conducting simultaneous PIV and BOS measurements so as to eliminate discrepancies in cooling ratio values for a single test due to the stochastic nature of the spark. A detailed analysis of the cause of entrainment that leads to this cooling will also provide further insight into the flow induced and the cooling of the hot gas kernel.

Different electrode gap distances will affect the coherent structures induced in the gap [17] and hence the vortex dynamics, entrainment rates and cooling regimes are also likely to be different. Some work exists on the effect of electrode gap distance on the induced hot gas kernel [11], [32] however a generalization on the cooling regimes described in this work cannot be made at this time and is beyond the scope of this work. This understanding of the flow field and the relationship between fluid entrainment and the cooling process will inform future studies on these types of spark discharges and can be extended to understanding a broad range of phenomena related to all types of plasma discharges and their applications.

### **Appendix**

The uncertainty in the BOS cooling ratio  $\kappa_{BOS}$  is calculated as,

$$\sigma_{\kappa_{BOS}} = \sqrt{\left(\frac{1 - \bar{\rho}_i}{\rho_\infty - \bar{\rho}_i}\right)^2 \sigma_{\rho_f}^2 + \left(\frac{\bar{\rho}_f - \rho_\infty}{(\rho_\infty - \bar{\rho}_i)^2}\right)^2 \sigma_{\rho_i}^2} \quad (2.A.1)$$

where,  $\sigma_{\bar{\rho}}$  represents the uncertainty in the mean kernel density and can be expressed in terms of the density uncertainties of the points within the kernel as  $\sigma_{\bar{\rho}} = \frac{1}{n} \sqrt{\sum \sigma_{\rho}^2}$ . The uncertainties in the cooling ratio estimates from BOS measurements ranged from 0.04% to 0.09% of the cooling ratio value.

The uncertainty in the cooling ratio calculated using S-PIV data is similarly determined by propagating uncertainties through the right-hand side of the cooling ratio equation, and is given by,

$$\sigma_{\kappa} = \sqrt{\left(\frac{\partial \kappa}{\partial \eta}\right)^2 \sigma_{\eta}^2} \quad (2.A.2)$$

where  $\eta = \frac{\dot{V}_{in}}{\frac{w^2}{4} h}$  is the instantaneous entrainment per unit volume of the kernel. The uncertainty in this term is given by,

$$\sigma_{\eta} = \sqrt{\left(\frac{\partial \eta}{\partial \dot{Q}_{in}}\right)^2 \sigma_{\dot{V}_{in}}^2 + \left(\frac{\partial \eta}{\partial w}\right)^2 \sigma_w^2 + \left(\frac{\partial \eta}{\partial h}\right)^2 \sigma_h^2} \quad (2.A.3)$$

where the entrainment is defined as,

$$\dot{V}_{in} = \int_0^{\frac{w}{2}} \int_0^{2\pi} v_{rel} x dx d\theta \quad (2.A.4)$$

the equation for relative velocity ( $v_{rel}$ ) is given by the equation below,

$$v_{rel} = \sqrt{(v - v_{ring})^2 + (u - u_{ring})^2} \quad (2.A.5)$$

giving the uncertainty in entrainment as,

$$\sigma_{\dot{Q}_{in}} = 2\pi \sqrt{\left(\frac{\partial \dot{V}_{in}}{\partial v_{rel}}\right)^2 \sigma_{v_{rel}}^2 + \left(\frac{\partial \dot{V}_{in}}{\partial x}\right)^2 \sigma_x^2} \quad (2.A.6)$$

The uncertainty in the relative velocity, calculated using a 4<sup>th</sup> compact noise optimized Richardson extrapolation finite difference scheme used in entrainment calculation is given by,

$$\sigma_{v_{rel}} = \sqrt{\left(\frac{\partial v_{rel}}{\partial v}\right)^2 \sigma_v^2 + \left(\frac{\partial v_{rel}}{\partial v_{ring}}\right)^2 \sigma_{v_{ring}}^2 + \left(\frac{\partial v_{rel}}{\partial u}\right)^2 \sigma_u^2 + \left(\frac{\partial v_{rel}}{\partial u_{ring}}\right)^2 \sigma_{u_{ring}}^2} \quad (2.A.7)$$

with the uncertainties in the calculation of ring velocities calculated according to [72].

The uncertainties in calculation of the width and height of the control volume are dependent on the uncertainty in the centroid ( $X_0$  and  $Y_0$ ), given below,

$$\sigma_w = \frac{1}{\sqrt{2}} \sigma_{X_0} \quad (2.A.8)$$

$$\sigma_h = \sqrt{2} \sigma_{Y_0} \quad (2.A.9)$$

$$\sigma_{X_0} = \sqrt{\left(\frac{1}{\sum \lambda_{ci_i}}\right)^2 \left(\sum \sigma_{\lambda_{ci_i}}^2 x_i^2 + \sigma_{x_i}^2 \lambda_{ci_i}^2\right) + \left(\frac{\sum x_i \lambda_{ci_i}}{(\sum \lambda_{ci_i})^2}\right)^2 \left(\sum \sigma_{\lambda_{ci_i}}^2\right)} \quad (2.A.10)$$

$$\sigma_{Y_0} = \sqrt{\left(\frac{1}{\sum \lambda_{ci_i}}\right)^2 \left(\sum \sigma_{\lambda_{ci_i}}^2 y_i^2 + \sigma_{y_i}^2 \lambda_{ci_i}^2\right) + \left(\frac{\sum y_i \lambda_{ci_i}}{(\sum \lambda_{ci_i})^2}\right)^2 \left(\sum \sigma_{\lambda_{ci_i}}^2\right)} \quad (2.A.11)$$

where  $\lambda_{ci}$  is calculated as,

$$\lambda_{ci} = \left| \text{imag} \left( \frac{1}{2} \left( \frac{\partial u}{\partial x} + \frac{\partial v}{\partial y} \right) \pm \frac{1}{2} \sqrt{\left( \frac{\partial u}{\partial x} + \frac{\partial v}{\partial y} \right)^2 - 4 \left( \frac{\partial u}{\partial x} \frac{\partial v}{\partial y} - \frac{\partial u}{\partial y} \frac{\partial v}{\partial x} \right)} \right) \right| \quad (2.A.12)$$

and its uncertainty ( $\sigma_{\lambda_{ci}}$ ) is given by,

$$\sqrt{\frac{1}{4} \left( \left( \frac{0.7085}{\Delta} \right)^2 (\sigma_u^2 + \sigma_v^2) + \frac{1}{\left( \sqrt{\frac{1}{4} \left( \frac{\partial u}{\partial x} \right)^2 + \frac{1}{4} \left( \frac{\partial v}{\partial y} \right)^2 - \frac{1}{2} \frac{\partial u}{\partial x} \frac{\partial v}{\partial y} + \frac{\partial u}{\partial y} \frac{\partial v}{\partial x}} \right)^2 \left( \frac{1}{4} \left( \frac{\partial u}{\partial x} \right)^2 + \frac{1}{4} \left( \frac{\partial v}{\partial y} \right)^2 + \left( \frac{\partial v}{\partial x} \right)^2 \right) \left( \frac{0.7085}{\Delta} \right)^2 \sigma_u^2 + \left( \frac{1}{4} \left( \frac{\partial v}{\partial y} \right)^2 + \frac{1}{4} \left( \frac{\partial u}{\partial x} \right)^2 + \left( \frac{\partial u}{\partial y} \right)^2 \right) \left( \frac{0.7085}{\Delta} \right)^2 \sigma_v^2} \right)} \quad (2.A.13)$$

### 3. VORTEX RINGS DRIVE ENTRAINMENT AND COOLING IN FLOW INDUCED BY A SPARK DISCHARGE

Bhavini Singh<sup>1</sup>, Lalit K. Rajendran<sup>1</sup>, Jiacheng Zhang<sup>2</sup>, Pavlos P. Vlachos<sup>2</sup>, and Sally P. M. Bane<sup>1</sup>

<sup>1</sup>*School of Aeronautics and Astronautics, Purdue University, West Lafayette, Indiana 47907, USA*

<sup>2</sup>*School of Mechanical Engineering, Purdue University, West Lafayette, Indiana 47907, USA*

This chapter has been previously published in *Physical Review Fluids*

DOI: 10.1103/PhysRevFluids.5.114501

#### ***Abstract***

Spark plasma discharges induce vortex rings and a hot gas kernel. We develop a model to describe the late stage of the spark induced flow and the role of the vortex rings in the entrainment of cold ambient gas and the cooling of the hot gas kernel. The model is tested in a plasma-induced flow, using density and velocity measurements obtained from simultaneous stereoscopic particle image velocimetry (S-PIV) and background oriented schlieren (BOS). We show that the spatial distribution of the hot kernel follows the motion of the vortex rings, whose radial expansion increases with the electrical energy deposited during the spark discharge. The vortex ring cooling model establishes that entrainment in the convective cooling regime is induced by the vortex rings and governs the cooling of the hot gas kernel, and the rate of cooling increases with the electrical energy deposited during the spark discharge.

#### **3.1 Introduction**

There is a significant interest in understanding the dynamics of the flow induced by spark discharges, especially their impact in the fields of flow and combustion control [2], [77]. For example, quantitative information on the rate of cooling of the induced hot gas kernel and the mechanisms driving the flow induced can be used to determine the pulsation frequency necessary to stabilize flames and promote lean, efficient combustion [21], [26], [78]. Further, studying the spatial extent of the induced flow, its temporal evolution and the effect of energy deposited can be

used to optimize ignition systems and promote repeatable ignition [27]. However, the spark induced flow field is complex, transient, and requires diagnostics with high spatiotemporal resolution. As a result, prior work has been limited to qualitative experiments [11], [13], [16], [28] or computational simulations [12], [24], [31], [32], [79], the majority of which focused on the very early ( $<100 \mu\text{s}$ ) stages of the induced flow field. These studies have shown that the spark creates a hot gas kernel between the electrodes that cools over time. Some computations have shown the presence of vortices near the electrodes [12], [13], and in one of these studies, the authors postulate that these vortices are responsible for the shape of the hot gas kernel [13]. Recently, we performed measurements using stereoscopic particle image velocimetry (S-PIV) and background oriented schlieren (BOS) to measure the velocity and density fields, respectively, during the kernel cooling process [33], [80]. The velocity measurements showed the presence of vortex rings near each electrode and significant entrainment of ambient gas into the electrode gap [17], [80]. The density measurements showed that the cooling of the hot gas kernel occurs in two distinct regimes: an initially fast, convective cooling regime, followed by a slower cooling regime, with the fast regime contributing approximately 50% of the overall cooling in less than 1 ms after the spark discharge. We also developed a reduced-order model to describe the cooling process and showed that the entrainment of cold ambient gas into the electrode gap controls the rate of cooling in the fast regime [80]. However, the driving mechanism behind the cold gas entrainment remains unresolved.

In this work, we use theory and experiment to demonstrate that the induced vortex rings drive the entrainment and thus control the rate of cooling of the hot gas kernel. We develop a model for the entrainment using inviscid vortex ring theory that directly relates the geometric and kinematic properties of the vortex rings to the cooling. To test the model predictions, we perform simultaneous measurements of velocity and density in a flow field induced by a spark discharge using time-resolved S-PIV and BOS. Simultaneous measurements are critical because the spark discharge is a chaotic process, and thus each realization of the flow field is different.

The high spatiotemporal resolution measurements capture the spatial organization of the vortex rings with respect to the hot gas kernel. We reveal the role that induced vorticity plays in heat transfer and the dynamics of flows induced by sparks and discover that spark discharges produce vortex-driven mixing flow. This could have broad implications in a variety of scientific,

engineering and technological applications by enabling the alteration of temperature, chemical species distribution (combustion), and momentum transport (flow control).

### 3.2 Vortex ring cooling model

The vortex ring cooling model presented herein expands upon our prior work, where a model relating entrainment to the cooling of the hot gas kernel was developed by considering the rate of change of enthalpy of the kernel [80]. Entrainment is defined in this work as the volume of fluid that flows across the surface of the control volume. We assumed low Mach number, inviscid flow, negligible body forces, negligible heat transfer due to conduction and radiation, as well as a calorically perfect gas, to simplify the energy equation to:

$$\frac{d\rho}{dt} = \frac{\dot{V}_{in}}{V_{cv}} (\rho_{\infty} - \bar{\rho}) \quad (3.1)$$

where  $\frac{d\rho}{dt}$  is the cooling rate of the hot gas kernel,  $\bar{\rho}$  and  $\rho_{\infty}$  are the mean kernel density and ambient density, respectively,  $\dot{V}_{in}$  is the volumetric entrainment, and  $V_{cv}$  is the volume of fluid enclosed by the control volume.

We further use the cooling rate equation to calculate the *cooling ratio* parameter as:

$$\left( \frac{\bar{\rho}_f - \bar{\rho}_i}{\rho_{\infty} - \bar{\rho}_i} \right) = 1 - \exp \left( - \int_{t_i}^{t_f} \frac{\dot{V}_{in}}{V_{cv}} dt \right) \quad (3.2)$$

where  $\bar{\rho}$  is the mean kernel density and  $t$  is time, with the subscripts  $i$  and  $f$  representing the initial and the final values in the convective cooling regime. This formulation of the cooling ratio assumes the ambient fluid that is entrained, perfectly mixes with the hot gas inside the kernel. Further, the mixing of the hot and cold gas does not affect the flow itself and is therefore passive. The cooling ratio represents the extent of completion of the cooling process, with a value of 1 indicating the fluid has cooled to the ambient temperature. The present work aims to relate the entrainment ( $\dot{V}_{in}$ ) to the properties of the vortex rings, subject to the hypothesis that the pair of vortex rings drive the entrainment and therefore govern the cooling in the convective regime.

The left-hand side of the cooling ratio equation is the density-based cooling ratio and is calculated by taking the difference in the mean final and initial density values within a control volume, in the

fast cooling regime, normalized by the density deficit at the start of the fast cooling regime. The right-hand side is the entrainment-based cooling ratio and is calculated from the entrainment due to the vortex rings, per unit volume of the cylindrical control volume.

### 3.2.1 Entrainment model

We approximate the hot gas kernel as a moving and deforming cylindrical control volume, defined by the centroids of the two vortex rings at the top and bottom and centered at the electrode axis,  $r = 0$  (Figure 3.1 (a)). The top and bottom vortex rings bounding the kernel are located at  $Z_t$  and  $Z_b$  and have ring radii  $R_t$ ,  $R_b$ , and core radii  $a_t$  and  $a_b$ , respectively. Entrainment into the control volume is calculated across the top and bottom boundaries. In the experimental measurements, the top and bottom vortex rings do not have the same dimensions, so the radius of the cylinder is taken as the mean of the top and bottom ring radii.

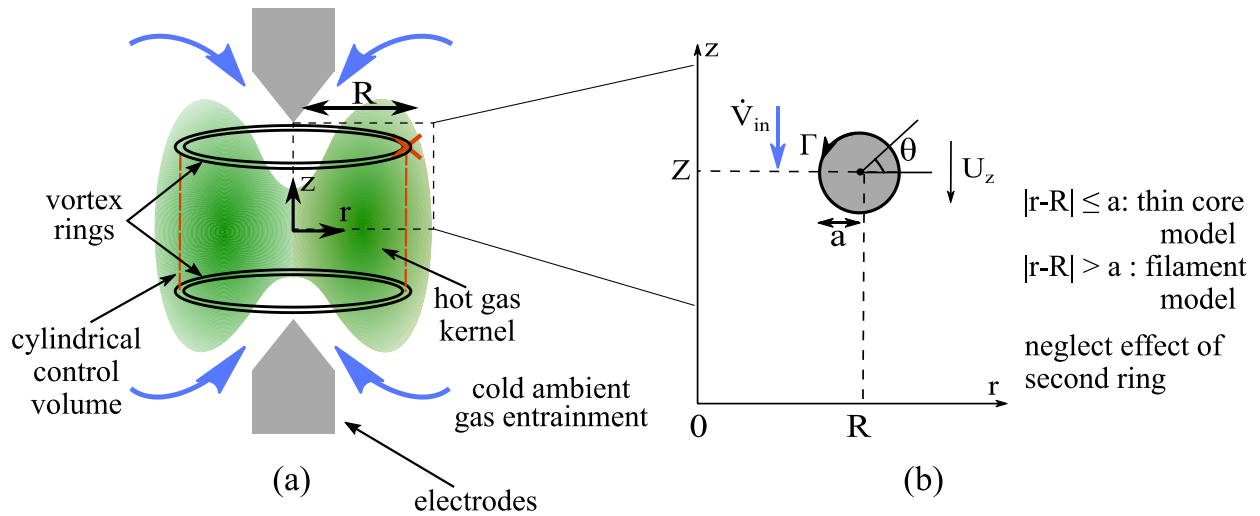


Figure 3.1: (a) Schematic of the vortex ring cooling model showing entrainment of cold ambient gas into the hot gas kernel, hypothesized to be due to a pair of thin core vortex rings. (b) Schematic showing a thin core ring with ring radius  $R$ , core radius  $a$ , circulation  $\Gamma$  and  $z$ -component of ring velocity  $U_z$ . Entrainment ( $\dot{V}_{in}$ ) is calculated using the thin core model inside the core and filament model outside. The effect of the second ring on entrainment across the boundary of the first ring is negligible, and vice versa.

We calculate the entrainment using a coordinate system attached to the vortex ring, as follows:

$$\dot{V}_{in} = 2\pi \left( \int_0^R u_z r dr - \int_0^R U_z r dr \right) \quad (3.3)$$

where  $R$  is the mean ring radii of the top and bottom vortex rings ( $R = \frac{1}{2}(R_t + R_b)$ ), and  $U_z$  is the  $z$ -component of the ring velocity, which is calculated separately for the top and bottom rings. The total entrainment is the sum of the entrainment across both the top and bottom boundaries of the control volume.

We define a function  $f(r, z)$ , the entrainment function in cylindrical coordinates, such that:

$$u_r = -\frac{1}{r} \frac{\partial f}{\partial z} \quad \text{and} \quad u_z = \frac{1}{r} \frac{\partial f}{\partial r} \quad (3.4)$$

where,  $u_r$  and  $u_z$  are the radial and axial velocities, respectively. Substituting the definition of the entrainment function (Equation 3.4) into Equation 3.3 gives:

$$\dot{V}_{in} = 2\pi \left( [f(R, Z) - f(0, Z)] - \frac{1}{2} U_z r^2 \Big|_0^R \right) \quad (3.5)$$

For incompressible flow, this entrainment function is equivalent to the stream function. The low Mach number assumption implies that changes in density are only due to changes in temperature and that the flow is acoustically incompressible (as the cooling process occurs long after the shock wave has departed the field of view). Buoyancy effects are also negligible. Under these assumptions, we can employ vortex ring models derived for incompressible flows to calculate entrainment for our flow field, assuming one-way coupling, namely that variations in density do not affect the velocity field.

### 3.2.2 Thin core vortex ring model

The entrainment is calculated as the difference of the values of the entrainment function between the ring centroid ( $r = R$ ) and the axis of symmetry ( $r = 0$ ) (Equation 3.5). Using ring-fixed coordinates, the motion of the ring is accounted for by subtracting the last term in Equation 3.5. The total entrainment into the control volume is the sum of the entrainment due to both vortex rings. Several approaches have been proposed to model the entrainment induced by vortex rings [81]–[86], and they depend on the model used for the vorticity distribution inside the rings. In this

work, we consider inviscid, thin-cored vortex rings of uniform vorticity inside the core ( $\omega(r, z) = \omega_0 r/R$ ) where it is assumed that the cores do not overlap, and the core radius is much less than the ring radius. We use two models to calculate the entrainment function: 1) a filament model outside the core of the ring and 2) a thin-core model for points that lie inside the ring core, as shown in Figure 3.1(b). Since the equation for entrainment (Equation 3.5) employs the value of the function at two points, we use the filament model at the axis of symmetry ( $r = 0$ ), and the thin-core model at the ring centroid ( $r = R$ ). Finally, the entrainment due to one vortex ring at the location of the other ring was found to be negligible (on average, 10% of the entrainment due to the second ring on itself) and was therefore omitted in the total entrainment calculation. In summary, the entrainment across the top and bottom faces of the control volume is calculated based only on ring properties.

The entrainment function, according to the filament model, is given by [82], [85], [87]:

$$f(r, z) = \frac{\Gamma}{2\pi} \sqrt{Rr} \left[ \left( \frac{2}{\sqrt{m}} - \sqrt{m} \right) K(m) - \frac{2}{\sqrt{m}} E(m) \right] \quad (3.6)$$

where  $\Gamma$  is the circulation of the vortex ring,  $m = \frac{4rR}{L^2}$ ,  $L^2 = (z - Z)^2 + (r + R)^2$  and  $K, E$  are elliptic integrals of the first and second kind. The filament model assumes inviscid, infinitesimally thin vortex rings and is valid at distances far from the centroid of the vortex ring.

The entrainment function inside the core of the vortex ring is calculated using the thin-core model, according to Saffman [82]. This model uses the asymptotic properties of the elliptic integrals as  $m \rightarrow 1$  ( $r/R \rightarrow 1$ ) and assumes uniform vorticity inside the core to obtain:

$$f(r, z) = \frac{\Gamma R}{2\pi} \left[ \log \left( \frac{8R}{a} \right) - \frac{3}{2} - \frac{d^2}{2a^2} + \frac{d}{2R} \cos \theta \left[ \log \frac{8R}{a} + 1 - \frac{5d^2}{4a^2} \right] \right] \quad (3.7)$$

where  $\theta$  is defined as shown in Figure 3.1 and  $d$  is the distance from the centroid of the ring core and is given by  $d = \sqrt{(r - R)^2 + (z - Z)^2}$ .

The ring velocity  $U_z$  in Equation 3.5 is taken to be the self-induced ring velocity [88] because the effect of the second ring is negligible:

$$U_z = \frac{\Gamma}{4\pi R} \left[ \log \frac{8R}{a} - \frac{1}{4} \right] \quad (3.8)$$

The model parameters,  $\Gamma$ ,  $R$ , and  $a$  are all calculated from the velocity field induced by the spark discharge measured using S-PIV experiments.

### **3.3 Experimental methods and techniques**

The cooling effect in a single spark discharge was investigated using measurements of the induced velocity field and density field. Simultaneous time -resolved S-PIV and BOS measurements were performed for a range of energy values from 2.2 to 5.1 mJ. Each experimental run was spaced out at least 30 seconds apart to eliminate residual flow effects from one spark event to the next.

#### **3.3.1 Plasma generation**

A single nanosecond spark discharge was generated between two electrodes using a high voltage pulse generator from Eagle Harbor Technologies. The electrodes were machined out of ceriated-tungsten and had cone-shaped tips. Details of the plasma generation set-up are given in prior work [80]. The energy deposited in the electrode gap was controlled by limiting the current through the discharge by adding resistances in series with the spark, as shown in Figure 3.2 where the label “R” represents the resistances. Total resistance values of 0, 100, 200, 400, 600, and 1000 were used in these experiments, where a resistance value of 0 means that no resistance was added in the electrical configuration. For each resistance level, multiple tests were conducted, resulting in a range of energy values from 2.2 mJ to 5.1 mJ.

#### **3.3.2 Simultaneous velocity and density measurements**

##### **3.3.2.1 Experimental set-up**

A schematic of the simultaneous S-PIV and BOS system is shown in Figure 3.2. The time-resolved S-PIV system consisted of a QuasiModo quasi-continuous burst-mode (QCBM) Nd:YAG laser [89], two high-speed Photron SA-Z cameras, and an acrylic test section containing the electrodes. The laser was operated at 50 kHz, and laser sheet optics produced an approximately 1 mm thin waist in the region of interest where the spark discharge was generated. The cameras with an included angle of approximately  $50^\circ$  were operated with Nikon AF FX Micro-Nikorr 200 mm lenses and recorded particle images at a sampling rate of 50 kHz. The resolution for the two

cameras was approximately  $600 \times 640$  pixels, corresponding to an approximate field of view of  $6 \times 6.5$  mm. Alumina particles were injected into the test enclosure with diameters of about  $0.3 \mu\text{m}$  and the estimated Stokes number of approximately 0.002. The BOS system consisted of a Phantom v2640 camera with a Nikon Nikorr 105 mm lens,  $f\# 11$ , and a 2x teleconverter, which recorded at a 20 kHz sampling rate, with a resolution of  $1024 \times 704$  pixels, corresponding to an approximate field of view of  $10 \times 7$  mm. The dot pattern contained dots  $42 \mu\text{m}$  in diameter with an equal edge to edge spacing between the dots of  $42 \mu\text{m}$ , and was back-illuminated using a 150 W xenon arc lamp (Newport 66907). The distance from the center of the electrodes to the BOS target ( $Z_D$ ) was approximately 32 mm, and the distance from the center of the electrodes to the camera ( $Z_A$ ) was approximately 165 mm. A delay generator was used to synchronize and trigger the laser, the S-PIV, and BOS cameras and the high voltage pulser.

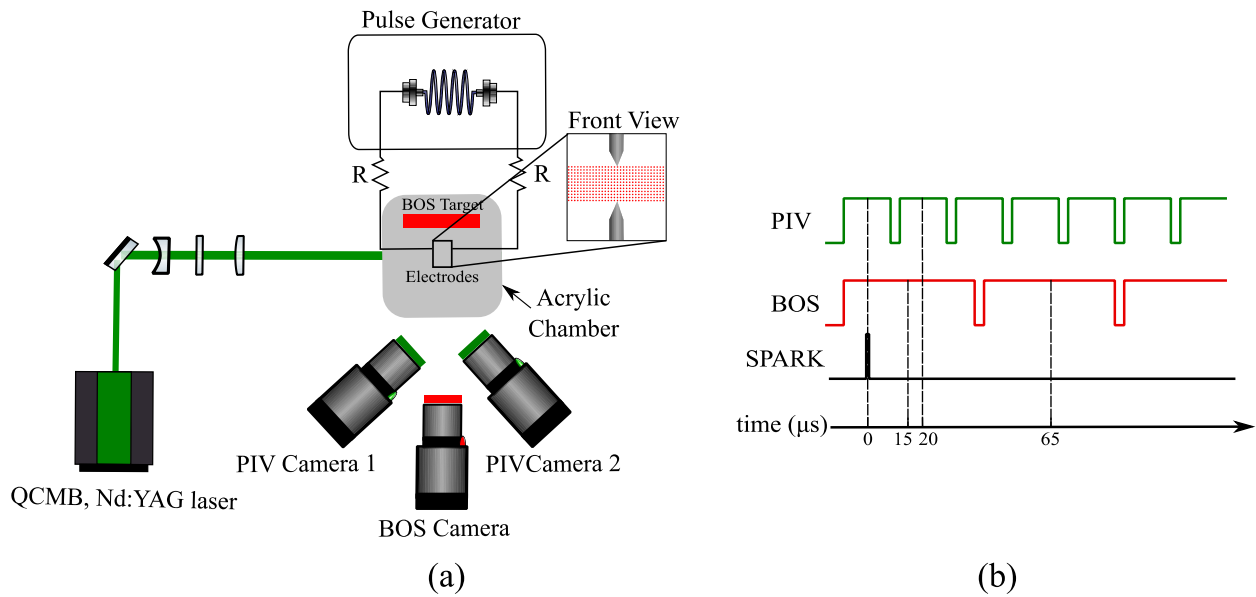


Figure 3.2: (a) Schematic of the experimental set-up for simultaneous S-PIV and BOS measurements of the plasma-induced flow field. (b) Timing diagram used to synchronize the simultaneous measurements.

### 3.3.2.2 S-PIV image processing and uncertainty quantification

The recorded S-PIV particle images were processed using PRANA (PIV, Research, and ANalysis) software [90]. A total of four passes were used, and a 50% Gaussian window was applied to the original window size [49] resulting in window resolutions of  $64 \times 64$  pixels in the first pass to  $32 \times 32$

pixels in the last pass, with 50 % window overlap in all passes. The projected velocity fields calculated in this manner were then combined with the camera angle information obtained from calibration to yield the three components of velocity in the measurement plane [57]. Proper orthogonal decomposition with the entropy line fit (ELF) method [58] was used to denoise the PIV velocity fields. The spatial resolution for velocity calculations was 0.32 mm, and each snapshot contains 38 x 40 vectors. Further details on the calibration procedure and processing can be found in prior work [80].

Experimental uncertainties in the S-PIV measurements were propagated according to the procedure outlined by Bhattacharya *et al.* [66]. Uncertainties in the planar velocity fields were calculated using the moment of correlations (MC) [65] and then propagated through the stereo reconstruction to calculate uncertainty in the reconstructed velocity field. Maximum uncertainties in the three components of velocity (u, v and w) were approximately 0.1 m/s, 0.1 m/s and 0.3 m/s, corresponding to 2.5%, 2.5% and 7.5% of the maximum velocity (4 m/s), respectively.

### **3.3.2.3 BOS image processing and uncertainty quantification**

The distortion of the dot pattern is estimated by cross-correlating an image taken with the flow to a reference image taken without the flow. The images were processed using the same approach and software (PRANA) as for the S-PIV measurements. A total of four passes were used with window resolutions of 64x64 pixels in the first pass to 32x32 pixels in the last pass, with a 50 % window overlap in all passes. The spatial resolution of the final pass was 0.31 mm, and each snapshot contained 62 x 24 vectors. The projected density field  $\rho_p(x, y)$ , was then calculated from the displacement field by 2D integration using an uncertainty based Weighted Least Squares (WLS) methodology, wherein the density gradient measurements are weighted based on the inverse of their uncertainty [91]. Finally, the actual density field  $\rho(r, z)$  was calculated from the projected density field by Abel inversion under the assumption that the flow is axisymmetric. Further details on the processing and calculation of the density field from displacement values can be found in prior work [80].

Experimental uncertainties in the BOS measurements were propagated through the complete density reconstruction according to [69]. Uncertainties in the displacement field were calculated

using MC [65], then propagated through the optical layout followed by the WLS solver to obtain uncertainty in the projected density field. The uncertainties were then propagated through the Abel inversion to obtain total uncertainty in the density field. The maximum uncertainties in the density field were approximately  $0.005 \text{ kg/m}^3$ , corresponding to 0.4% of ambient density ( $1.225 \text{ kg/m}^3$ ).

### 3.3.3 Non-dimensionalization of results

All results were non-dimensionalized using the induced velocity ( $u_{shock}$ ) and density ( $\rho_{shock}$ ) behind the shock wave produced by the spark and the characteristic length ( $d$ ) taken to be the electrode gap distance (5 mm) [17], [80]. The velocity and length scales were used to define a characteristic time scale,  $\tau$ , as  $d/u_{shock}$ . For the maximum energy value of 5.1 mJ,  $u_{shock}$ ,  $\rho_{shock}$  and  $\tau$  are 61 m/s,  $1.45 \text{ kg/m}^3$ , and 0.08 ms, respectively, and for the minimum energy value of 2.2 mJ, they are 41 m/s,  $1.38 \text{ kg/m}^3$ , and 0.12 ms, respectively. Further details on the non-dimensionalization can be found in prior work [80].

### 3.3.4 Entrainment function calculation from PIV velocity fields

The entrainment calculated from the vortex ring models was compared to a direct calculation of entrainment from the experiment according to Equation 3.5. The gradients of the entrainment function  $f$  were calculated from the measured velocity field as:

$$\frac{\partial f}{\partial z} = -ru_r \quad \text{and} \quad \frac{\partial f}{\partial r} = ru_z. \quad (3.9)$$

The field of  $f$  was then obtained by solving the following equation as:

$$\begin{bmatrix} G_z \\ G_r \\ L_0 \end{bmatrix} \mathbf{f} = \begin{bmatrix} -ru_r \\ ru_z \\ f_0 \end{bmatrix}, \quad (3.10)$$

where  $G_z$  and  $G_r$  are the discrete gradient operators (2D matrices) along the  $z$ -dimension and  $r$ -dimension, respectively,  $\mathbf{f}$  is the column vector containing the discrete entrainment function values, and  $L_0$  is the labeling matrix consisting of zeros and ones for imposing the Dirichlet boundary conditions  $f_0$ . Equation 3.10 forms an overdetermined linear system and may not be consistent with possessing a solution. Thus Equation 3.10 was solved via optimization using least-squares as:

$$\begin{aligned}
\mathbf{f} &= \underset{f}{\operatorname{argmin}} (\|Gf - s\|_2) = (G^T G)^{-1}(G^T \mathbf{s}), \\
G &= [G_z \quad G_r \quad L_0]^T \\
\mathbf{s} &= [-ru_r \quad ru_z \quad f_0]^T
\end{aligned} \tag{3.11}$$

where  $G$  represents the augmented linear operator and  $\mathbf{s}$  is the augmented source term.

The variances  $\sigma_s^2$  of the values in  $\mathbf{s}$  can be estimated by propagating the uncertainty of the velocity measurement through Equation 3.9 as:

$$\boldsymbol{\sigma}_s = [r\sigma_{u_r} \quad r\sigma_{u_z} \quad \sigma_{f_0}]^T \tag{3.12}$$

where  $\sigma_{u_r}$  and  $\sigma_{u_z}$  are the uncertainty of the velocity components  $u_r$  and  $u_z$ , respectively, and  $\sigma_{f_0}$  is the uncertainty of the Dirichlet values in  $f_0$ . With the assumption that the errors in the source term are uncorrelated, the covariance matrix  $\Sigma_s$  of the augmented source term can be estimated as the diagonal matrix with the diagonal elements being  $\sigma_s^2$ . Thus, the uncertainty of the calculated entrainment function can be obtained by propagating  $\Sigma_s$  through Equation 3.11 as:

$$\begin{aligned}
\Sigma_f &= M\Sigma_s M^T, \\
\text{with } M &= (G^T G)^{-1}G^T,
\end{aligned} \tag{3.13}$$

where  $\Sigma_f$  is the covariance matrix of the entrainment function. The square root of the diagonal elements in  $\Sigma_f$  corresponds to the uncertainty in the calculated entrainment function values.

### 3.3.5 Post-processing metrics and calculation of parameters

The post-processing steps are summarized in Figure 3.3. Once the density and velocity fields were processed, the 2D grid was split along the electrode axis ( $r = 0$ ), and the left side was flipped and combined with the right-hand side to create a spatially averaged axisymmetric field. The velocity field was then time averaged to match the temporal resolution of the density field. The coherent vorticity was calculated from the velocity field using a 4th order compact noise optimized Richardson extrapolation scheme [72] and the coherent structures were identified based on swirl strength using the  $\lambda_{ci}$  method [73]. All swirl values that were at least 2% of the maximum swirl strength were taken as the vortex cores. The core radius was defined as the radius of a circle that occupied the same area as the vortex cores, and the centroid of the core was defined as the barycenter of the calculated area, weighted by  $\lambda_{ci}$  values. These centroids were used to define the cylindrical control volume used in the calculation of both the mean density and entrainment from

the BOS and S-PIV measurements, respectively. The mean density within the control volume was calculated, and the time history of the mean kernel density was used to determine the cooling regimes in the flow. The cooling analysis in this work is restricted to the fast, convective cooling regime, which ranges from  $t = t_i$ , the time of minimum density, to  $t = t_f$ , the changeover point, or the end of the convective cooling regime. The changeover point,  $t_f$ , is the time instant at which the running mean and slope of the kernel density change abruptly. The cooling rate in the convective cooling regime is the slope of the fitted line to the mean density in this regime.

The experimental entrainment function values from S-PIV data were interpolated at the ring centroid locations defining the control volume as well as at  $r = 0$  and used to calculate the total, instantaneous entrainment for all tests. The tracked vortex ring centroids were differentiated in time to determine the experimental ring velocity  $U_z$  in Equation 3.5. The vortex ring parameters,  $R$ ,  $a$ , and  $\Gamma = \oint \vec{u} \cdot d\vec{l}$  were also calculated at each time step for each identified vortex ring and used to calculate the total instantaneous entrainment from the vortex ring model.

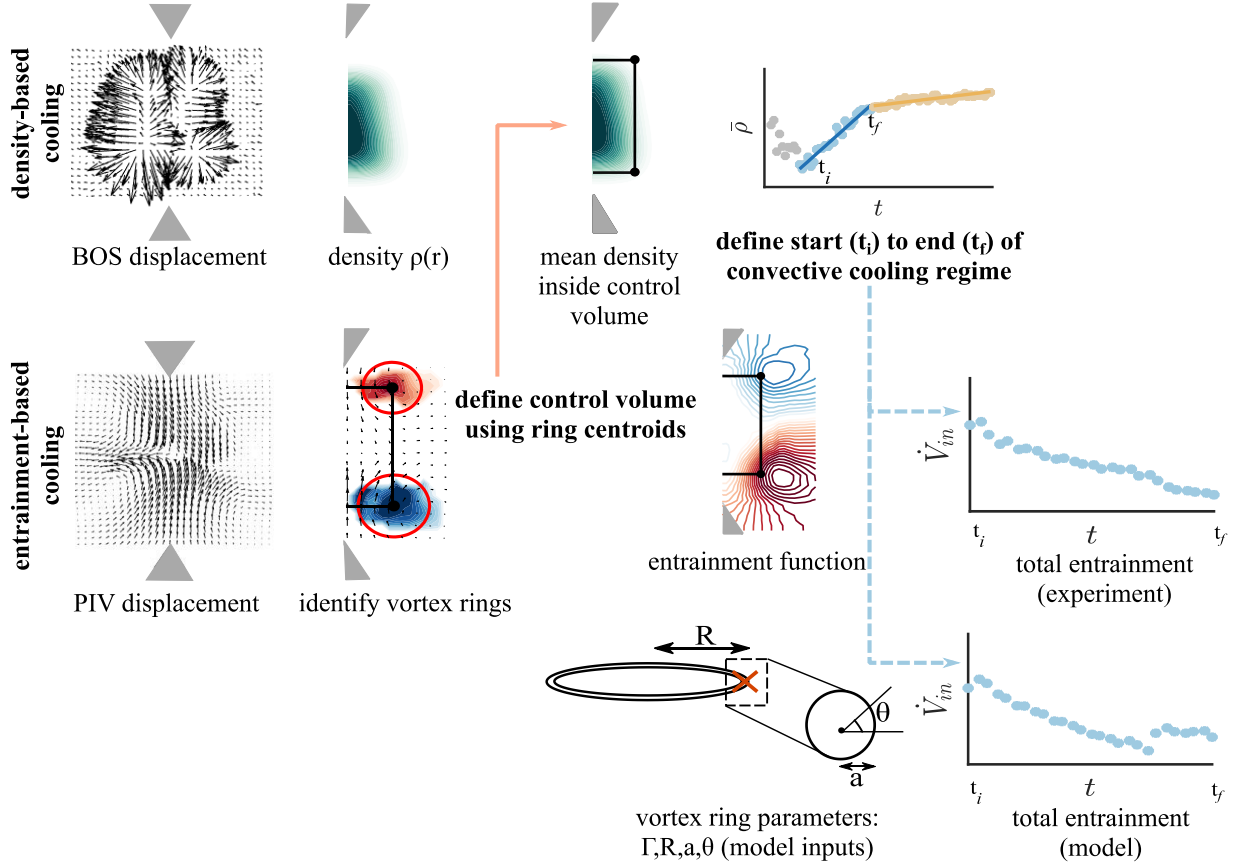


Figure 3.3: Post-processing steps for S-PIV and BOS measurements showing the identification of coherent vortex rings and density calculation. The centroids of the identified vortex rings are used to define the control volume used for entrainment calculations from experiment and model as well as mean kernel density calculation from BOS.

### 3.4 Results and discussion

#### 3.4.1 Spatial organization of the flow field and the effect of energy

The plasma-induced flow field for the highest (5.1 mJ) and lowest (2.2 mJ) energy cases are shown in Figure 3.4. The figure superimposes the hot gas kernel, shown in green, with the vortex rings and the experimentally calculated entrainment function. The hot gas kernel in the figure contains all points less than  $\rho/\rho_{shock}$  of 0.8. The intensity of the hot gas kernel is scaled as a percentage of the mean kernel density at  $t/\tau = 2$  of the high energy case. A darker kernel means it has a lower density.

In the initial stages of flow evolution ( $t/\tau = 2$ ), the shock wave has departed the field of view, and a cylindrical region of hot gas is observed. A pair of vortex rings are also induced and located close to the periphery of the hot gas kernel. The pair of vortex rings then move towards each other due to self-induction, eventually colliding, as the hot gas kernel simultaneously compresses axially. At  $t/\tau = 10$ , the vortex ring centroids are located entirely within the hot gas kernel. The rings and hot gas kernel then begin to expand radially outward while the hot gas kernel continues to cool, its minimum density reaching 90% of ambient density by  $t/\tau = 27$ .

The minimum density in the kernel ( $\rho/\rho_{shock}$ ) at  $t/\tau = 2$  is 0.48 and 0.59 for the high and low energy cases, respectively. The circulation of the vortex ring in the high energy case is 3 times larger than the low energy case. The vortex rings and hot gas kernel expand, with their radial extent ( $r/d$ ) increasing from 0.28 and 0.16 at  $t/\tau = 2$  to 0.55 and 0.3 by  $t/\tau = 27$  for the high and low energy cases, respectively, with a corresponding reduction in kernel height by a factor of 4 and 2 for the two different energy values. The increase in minimum density with time for both the high and low energy cases indicate that the hot gas kernel is cooling with time.

These results underscore that there is a coupling between the dynamics of the vortex rings and the cooling of the hot gas kernel. We further demonstrate that the energy deposited in the gap affects the level of heating in the electrode gap and both the strength of the vortex rings and the extent of radial expansion of the rings and hot gas kernel. The higher energy case induces a hot gas kernel that expands out radially along with the vortex rings, to a radius of approximately half the electrode gap distance, forming a torus shape. Conversely, in the lower energy case, both the vortex rings and hot gas kernel remain concentrated in the center of the gap with much less radial expansion, approximately half of that in the higher energy case. Stronger vortex rings and lower density (more heating) are observed in the high energy case compared to the lower energy case. More heating in the high energy cases leads to more significant density gradients between the kernel and ambient as well as higher mean entrainment values, because the increase in energy results in higher induced velocities within the electrode gap. The coupled effect of the increased entrainment and density gradients result in higher cooling rates of the hot gas kernel for higher energy values. The cooling rate is the rate of change in density of the hot gas kernel, within the control volume defined by the pair of vortex rings.

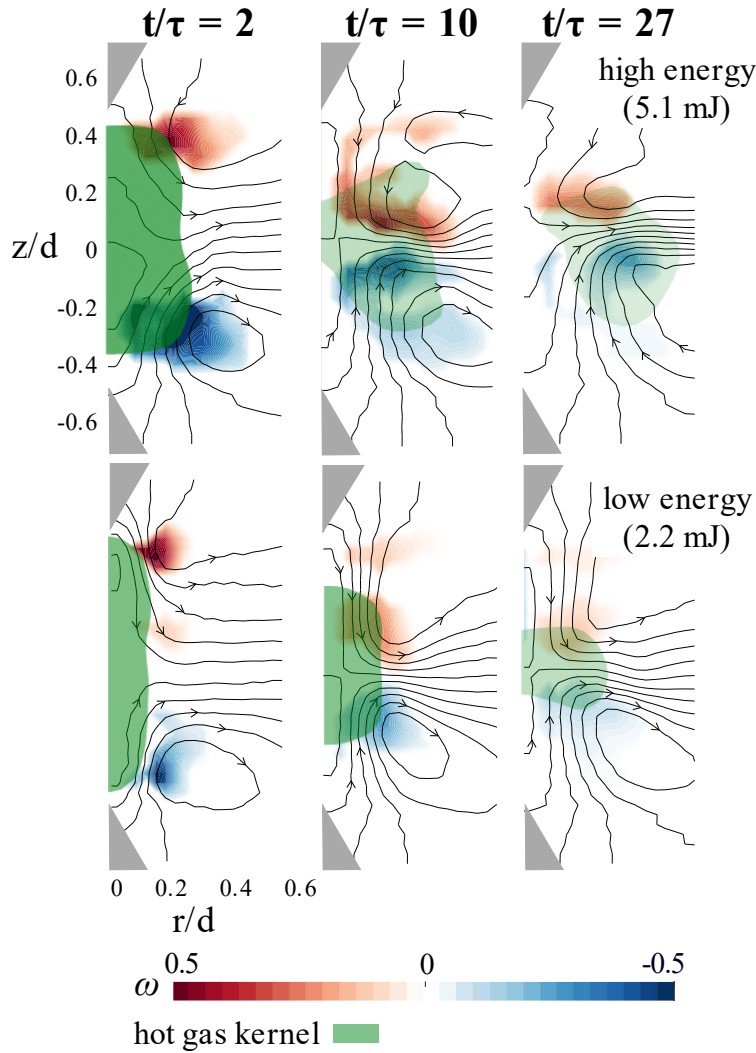


Figure 3.4: Time evolution of the induced hot gas kernel and vortex rings for the highest energy case (5.1 mJ, top) and the lowest energy case (2.2 mJ, bottom). A portion of the pair of vortex rings is located inside the hot gas kernel for all tests, with the spatial distribution of the vortex rings controlling the shape of the hot gas kernel. The intensity of the hot gas kernel is scaled using the mean kernel density, with a darker kernel signifying lower densities.

### 3.4.2 Application of vortex ring cooling model

The fast, convective cooling of the hot gas kernel is due to entrainment of cold ambient gas [80], but the driving mechanism behind this entrainment is not known. The simultaneous measurements in this study highlight the coupled behavior of the cooling of the hot gas kernel and the strength and dynamics of the vortex rings. These measurements also enable us to develop a model to test the hypothesis that the pair of vortex rings drive entrainment and control the cooling of the hot

kernel. The model calculations were tested on two levels: comparison of (1) entrainment and (2) cooling ratio, calculated from the model to the values calculated directly from the experiment.

### **3.4.2.1 Entrainment**

The instantaneous entrainment from the model and the S-PIV experiment calculated using Equation 3.5 is shown in Figure 3.5 (a). The entrainment from the model is calculated by substituting Equations 3.6-3.8 into Equation 3.5, and the entrainment from the experiment is calculated by substituting the entrainment function from the least-squares integration of the velocity field from the S-PIV measurements, described in Section 3.3.4, into Equation 3.5. The mean difference of  $-1.2 \times 10^{-5}$  between the two models, offset from the 1:1 line, shows that, on average, the model and experiment agree well. This mean difference between the model and experiment is within the mean uncertainty of the estimates ( $9 \times 10^{-5}$  and  $1.5 \times 10^{-4}$ , respectively). The entrainment values calculated from the model and experiment are statistically equivalent, supporting the hypothesis that the entrainment is due to the vortex rings.

### **3.4.2.2 Cooling**

The results in Figure 3.5 (b) show the cooling ratio values calculated in 3 different ways: (1) The density-based method which is a direct calculation from experimental density measurements from BOS, (2) the entrainment-based method using the least-squares integration of the S-PIV measurements, and (3) the entrainment-based method using the vortex ring model, driven by data from the S-PIV measurements. The cooling ratios from the entrainment-based calculations from the vortex ring model and the least-squares integration of the S-PIV measurements are compared to those from the density-based calculations, from BOS measurements. There is good agreement between the entrainment-based cooling ratio calculations from the vortex ring model and the experiment with a mean difference of 0.003, which is within the mean uncertainty in the cooling ratio calculated from the experiment of 0.004 and the model of 0.005. Comparison of the cooling ratios from the entrainment-based calculations to density-based calculations, which are a direct measure of the cooling, shows that both the entrainment-based calculations underpredict the cooling ratio by 0.07 compared to the density-based results. This difference in cooling ratio of 0.07 is 14% of the mean cooling ratio estimated using the density-based method. Overall agreement

between the cooling ratios from the experimental entrainment-based and density-based calculations confirm the results of our prior work that entrainment of cold ambient gas drives cooling of the hot gas kernel [80]. In addition, the agreement between the entrainment-based cooling ratio from the model and the density-based cooling ratio further supports the hypothesis that the vortex rings drive the cooling of the hot gas kernel. The cooling ratio values show that less cooling occurs at lower energy values. It was also observed (not shown) that the cooling occurs more rapidly with an increase in energy, with the cooling time for energy values less than 2.8 mJ observed to be about 1.6 times the duration at higher energy values. The cooling time at high energy values was approximately 1.2 ms and similar to previous work for the same energy range [80]. The cooling time is the duration of cooling in the convective regime, from the time of minimum density, to the time corresponding to the changeover from fast to slow cooling.

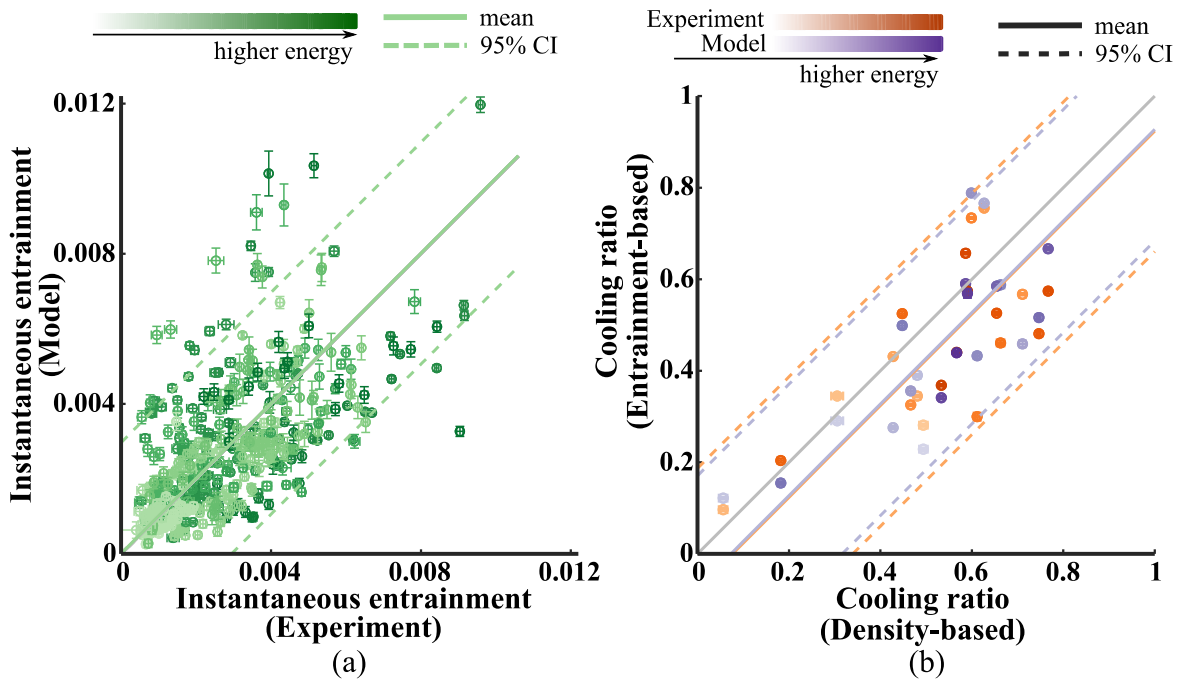


Figure 3.5: (a) Comparison of the total instantaneous entrainment calculated from the vortex ring model to experimental values calculated from least-squares integration of the S-PIV measurements and (b) comparison of cooling ratios from the entrainment-based calculations from the vortex ring model and the least-squares integration of the S-PIV measurements to the cooling ratios from the density-based calculations from BOS density data.

### 3.5 Conclusions

The flow induced by a spark discharge consists of a pair of induced vortex rings and a hot gas kernel. In this work, we study this flow using simultaneous, high spatiotemporal-resolution, density, and velocity field measurements using BOS and S-PIV, respectively, to test the hypothesis that vortex rings drive entrainment and cooling in the induced flow field. To this end, we develop and test a vortex ring cooling model to describe the kernel dynamics using energy conservation and inviscid, axisymmetric, vortex ring models.

The vortex ring cooling model was tested by comparing entrainment and cooling calculated from the model to the experiment. On average, the entrainment calculated from the model and experiment agreed well, with the mean difference between the model and experiment being less than the experimental uncertainty. The cooling calculations of the model were evaluated against cooling calculated from PIV data and BOS data. The model once again agreed well with the PIV experiment, with the mean difference in cooling ratio values lying within experimental uncertainty. The model underpredicts the cooling ratio compared to BOS, with the mean difference being 14% of the mean BOS cooling ratio. The mismatch between the model and the BOS experiment may arise from the axisymmetric assumption made in developing the model. Though the electrode geometry suggests that the flow would be axisymmetric, the spark formed between the electrodes is rarely a perfect cylinder, and the induced shock wave and heating from the spark are not always axisymmetric. A complete understanding of the 3-dimensionality of the flow field will require volumetric measurements.

The results of this work discover that spark discharges induce vortex-driven mixing flows. The induced vortex rings govern the spatial distribution of the hot gas kernel by driving entrainment of cold ambient gas into the kernel, thereby cooling it. The energy deposited in the electrode gap affects the strength of the vortex rings, as well as the extent to which the rings and hot gas kernel expand radially. Stronger vortex rings are induced at higher energy values, resulting in more entrainment and faster cooling of the hot gas kernel. Therefore, the energy deposited in the electrode gap affects the strength and dynamics of the vortex rings, and hence the duration and extent of cooling/mixing, allowing one to control the late stages of the induced flow. It is expected that in longer duration sparks (10 -100  $\mu$ s) the overall induced flow field will contain the same

major flow features as in this flow field induced by a nanosecond spark. We hypothesize that there will still be a pair of vortex rings induced as well as a kernel of hot gas and that the fast cooling will again be driven by the vortex rings. The time scales over which the cooling occurs, however, as well as the spatial extent of the cooling, will likely be different [11], [39]. A future study focusing on longer duration sparks can be used to further extend the current work.

This detailed understanding of the role of the vortex rings in the mixing and cooling process of the hot gas kernel has wide-ranging implications for momentum transport and passive scalar mixing in plasma-based flow and combustion control techniques. The model can help guide further research on a variety of plasma discharges where the presence of vortex rings has been established [35], [92], [93].

## 4. SHOCK GENERATED VORTICITY IN SPARK DISCHARGES

Bhavini Singh<sup>1</sup>, Lalit K. Rajendran<sup>1</sup>, Pavlos P. Vlachos<sup>2</sup>, and Sally P. M. Bane<sup>1</sup>

<sup>1</sup>*School of Aeronautics and Astronautics, Purdue University, West Lafayette, Indiana 47907, USA*

<sup>2</sup>*School of Mechanical Engineering, Purdue University, West Lafayette, Indiana 47907, USA*

This chapter has been submitted for publication and is currently under review.

### *Abstract*

Spark discharges induce a complex flow field consisting of a shock wave at early times ( $\sim 1 \mu\text{s}$ ), a pair of vortex rings, and a hot gas kernel. The vortex rings entrain ambient gas into the hot gas kernel and control its cooling and expansion. In this work, we investigate the shock wave's contribution in producing the vortex ring vorticity. We analyze high-speed (700 kHz) schlieren images of the shock wave for a range of electrical energies to measure the shock properties and estimate shock velocity and curvature. These measurements are combined with a model to calculate the vorticity generated. The measurements show that the highest vorticity is generated near the peak shock curvature location, and the shock curvature and strength increase with electrical energy deposited. A comparison of the vorticity estimated from the model to vorticity measurements from stereoscopic particle image velocimetry shows the results to be statistically equivalent. This suggests that the shock curvature and velocity contribute to the vortex rings induced by spark discharges.

### 4.1 Introduction

Spark plasma discharges lead to rapid heating and pressure rise in the electrode gap, resulting in a shock wave [10], [30], [39], [94]. The shock wave moves radially out of the center of the gap within a few microseconds [28]–[30] and decays rapidly into an acoustic wave. After the shock wave departure, the flow field is comprised of a hot gas kernel and vortex ring(s). The number of vortex rings, their dynamics, and the hot gas kernel evolution depend on the spark generation method [11], [17], [35], [36], [80], [95], [96]. In laser sparks, for instance, a pair of vortex rings of

unequal strength and size are induced [35], [97], while in sparks generated between cone-tipped electrodes (pin-to-pin discharges), a pair of two almost identical vortex rings are induced [17], [80], [95] and in surface discharges, a single vortex ring is formed that propagates away from the discharge surface [96].

In these cases, the strength and dynamics of the vortex ring(s) control the spatial extent and cooling of the hot gas kernel and thus play a critical role in engineering applications. In laser sparks, which are typically used for combustion applications, the vortex ring characteristics control the direction and ejection of the hot gas kernel [35], affecting ignition and flame growth [98]. In pin-to-pin electrical spark discharges, the rings entrain cold ambient gas into the hot kernel to promote rapid cooling/mixing, and this determines the required pulsation frequency of the discharges to utilize the synergetic effect of multiple pulses to optimize ignition systems [27] or to stabilize flames and promote efficient combustion [21], [22], [26].

Despite the critical role vortex rings play in the flow induced by spark discharges, to the best of our knowledge, there has been no quantitative experimental investigation on the source of this vorticity. Researchers have used CFD simulations to study the flow field at early times during the spark induced shock wave, and have suggested that there are two possible sources of vorticity generation, both through a baroclinic effect: (1) vorticity production due to the non-uniformity in the shock strength [30], [32], [33] (2) vorticity production due to the interaction of pressure gradients behind the shock wave with the hot gas kernel [32], [34]–[38]. In laser sparks, the second mechanism has been shown to be the dominant source of vorticity generation because the blast wave expands out of the field of view, depositing vorticity rapidly, while the pressure gradients and expansion waves following the blast wave interact with the low density region from the hot gas kernel for longer periods of time and generate more vorticity than the shock wave. In nanosecond spark discharges, the energy deposited in the gap is an order of magnitude lower than in laser sparks and the induced shock wave and trailing pressure gradients and expansion waves are also weaker. The two mechanisms by which vorticity is generated therefore may occur at similar time scales, and it is possible that because the trailing pressure waves are weaker in nanosecond sparks, the vorticity they generate is also weak. Therefore, the contribution of the vorticity jump across the shock should not be overlooked and a detailed experimental analysis on

the contribution of both mechanisms in low energy plasmas is needed. In this work, we experimentally investigate the shock wave's contribution to the vortex ring vorticity generation, via the first mechanism, as an initial estimate of the vorticity. We employ high-speed schlieren visualization and image processing methods to measure the shock properties and a model to calculate the vorticity based on these shock properties. We compare the estimated vorticity to measurements from stereoscopic particle image velocimetry (S-PIV) from prior work [95] and explore how the shock wave accounts for the vorticity in the vortex rings that drive cooling of the hot gas kernel at later times.

## 4.2 Vorticity generation due to a curved shock

Vorticity can be generated at a boundary and within a fluid due to baroclinicity. The vorticity transport equation is given as:

$$\frac{D\vec{\omega}}{Dt} = (\vec{\omega} \cdot \nabla)\vec{u} - \vec{\omega}(\nabla \cdot \vec{u}) + \frac{1}{\rho^2} \nabla\rho \times \nabla p + \nabla \times \left( \frac{1}{\rho} \nabla \cdot \tau \right) \quad (4.1)$$

where  $\vec{\omega}$  is vorticity,  $\vec{u}$  is the velocity,  $\rho$  and  $p$  are the density and pressure, respectively and  $\tau$  is the viscous stress tensor. The first two terms on the right-hand side represent changes in vorticity due to vortex stretching and compressibility effects, respectively. The third term represents the generation of vorticity due to misalignment of pressure and density gradients, which leads to baroclinic torque. The last two terms represent the diffusion of vorticity due to viscosity and the generation of vorticity due to a body force. In a compressible flow, such as the early stages ( $< 20 \mu\text{s}$ ) of the flow induced by a spark discharge, if we use the simplifying assumption that the flow is inviscid, we can neglect the last term in Equation 1.

In spark discharges, one source of vorticity is baroclinic torque arising from the non-uniform strength of the shock wave [32], [35], [36], which results in a curved shock. The generation mechanism of vorticity behind a curved shock has been explained using a purely dynamic approach by Hayes [99], who shows that the vorticity generated due to a curved shock is dependent only on the magnitude of the tangential component of the shock velocity. Other work used Crocco's theorem to arrive at the same result as Hayes for vorticity jump across a curved shock [100]–[102]. These works show that the non-uniformity in shock strength generates non-uniform entropy behind

a curved shock, resulting in an entropy gradient along the shock, which is responsible for vorticity generation. However, these studies are restricted to steady flows due to Crocco's vorticity law's inherent assumption, a restriction that is not necessary for Hayes' derivation.

The schematic in Figure 4.1 shows a slice of the curved shock generated by a spark discharge in cylindrical coordinates. The middle portion of the shock is approximately cylindrical and has been shown, via CFD simulations, to be stronger than the portions of the shock closer to the electrodes [30]. The difference in the strength of the shock along its length results in pressure and density gradients behind the shock that are misaligned, leading to baroclinicity [103]–[107]. The misalignment in the density and pressure gradients occurs in the regions where the shock is curved, with almost no misalignment in the center of the gap where the shock wave is mostly straight.

According to Hayes [99], the vorticity jump across this unsteady, axisymmetric, curved shock, generated under quiescent flow conditions, is given by:

$$\omega = -\frac{\partial U_s}{\partial e_1}(\epsilon - 1)^2\epsilon^{-1} \quad (4.2)$$

where  $U_s$  is the normal shock velocity. The tangential gradient  $\frac{\partial U_s}{\partial e_1}$  can be expressed in terms of the tangential shock velocity,  $U \cos \sigma$ , and shock curvature,  $\kappa$ , hence Equation (4.2) becomes:

$$\omega = -U \cos \sigma \kappa (\epsilon - 1)^2 \epsilon^{-1} \quad (4.3)$$

where  $\sigma$  is the angle the shock makes with the horizontal. The local shock curvature ( $\kappa = d\sigma/de_1$ ) is negative for the convex surface of the spark induced shock. The shock strength, measured as the density ratio  $\epsilon$ , is the ratio of the density behind the shock,  $\rho_s$ , to the density ahead of the shock  $\rho_\infty$ :

$$\epsilon = \frac{\rho_s}{\rho_\infty} = \frac{(\gamma + 1)M_n^2}{(\gamma - 1)M_n^2 + 2} \quad (4.4)$$

where  $\gamma$  is the ratio of specific heats, which assuming a perfect gas with constant specific heats, is taken to be 1.4. The normal shock Mach number,  $M_n$ , is calculated as  $U_s/a$  where  $a$  is the speed of sound in the ambient air, taken to be 343 m/s. Therefore, to calculate the shock-generated

vorticity, the model (Equations 4.3-4.4) requires the density ratio and the tangential shock velocity estimated from the shock Mach number, and the shock curvature and shock angle obtained from the shock profile. The next section details the experimental measurements capturing the shock wave and the procedure to estimate these parameters.

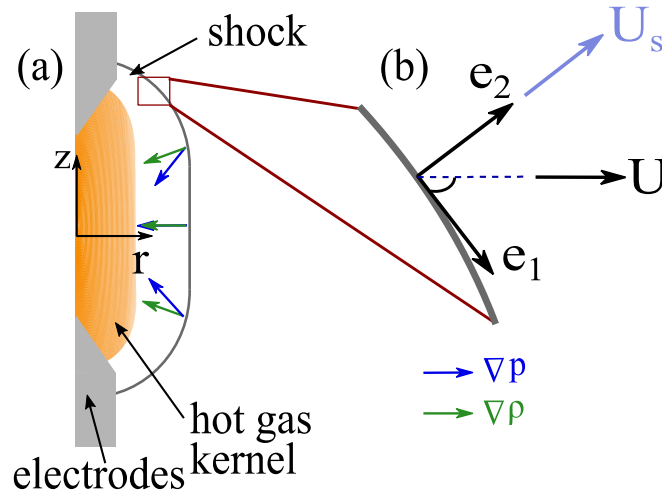


Figure 4.1: Schematic of shock generated due to a spark discharge showing (a) the curved nature of the shock wave in cylindrical coordinates and the misalignment of pressure and density behind the shock due to non-uniform shock strength; (b) the local coordinate system for a segment of the shock with normal shock velocity  $U_s$  and horizontal component of shock velocity  $U$ .

### 4.3 Experimental methods and techniques

The shock wave induced by a single spark discharge was captured using schlieren imaging for energy values ranging from 4.3 to 5.3 mJ, resulting in a total of 10 distinct experiments. Each spark discharge was generated using a nanosecond high voltage pulser in a 5 mm gap between two ceriated-tungsten electrodes with cone-shaped tips. Details on the plasma generation are given in prior work [80]. The experiments were conducted at least 30 seconds apart to eliminate residual flow effects from one spark event to the next. The parameters needed to calculate the vorticity jump were extracted from the first image of the shock after it had separated from the hot gas kernel, approximately  $3.5 \mu s$  after the spark.

### 4.3.1 Schlieren imaging

A schematic of the Z-type schlieren set-up used to image the spark induced shock wave is shown in Figure 4.2. The system consisted of a 150 W xenon arc lamp (Newport 66907) and a 60 mm aspheric condenser lens to create a point light source. Two concave mirrors 152.4 mm in diameter and with a focal length of 3.05 m, were used to collimate the light beam then converge it onto a knife edge. An intermediate lens was used to reduce light spillage before the collimating mirror to control the ray cone's angle emitted from the light source. The camera was set to a frame rate of 700,000 fps ( $\sim 1.4 \mu\text{s}$  between frames) at a resolution of  $64 \times 128$  pixels corresponding to a field of view of approximately  $5 \times 10$  mm and magnification of 0.08 mm/pixel. A delay generator was used to synchronize the camera and the high voltage pulser.

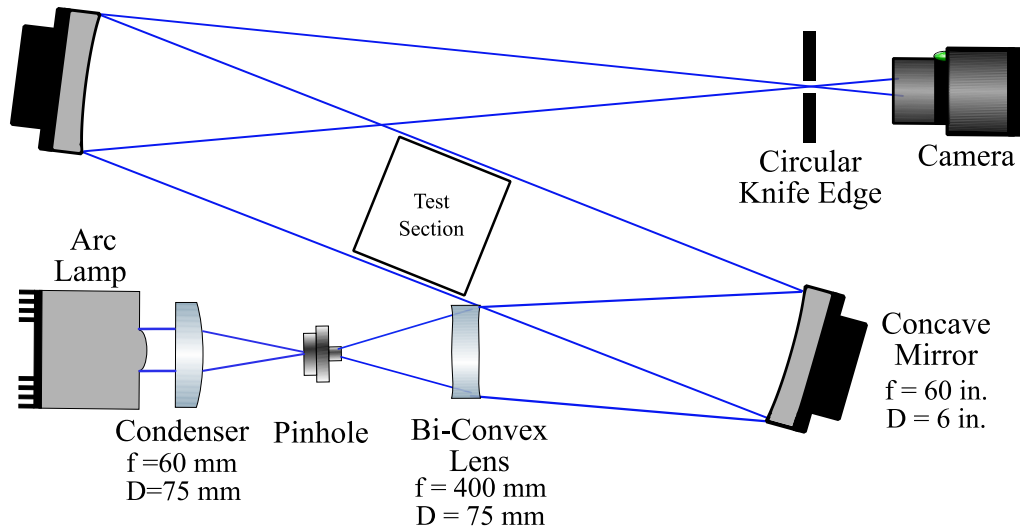


Figure 4.2: Schematic of the experimental set-up for schlieren measurements of the plasma-induced flow field

### 4.3.2 Processing metrics and calculations of parameters

A correlation-based image processing method was used to estimate the shock parameters. The ultra-high-speed recording leads to high image noise due to low exposure times and low spatial resolution due to camera hardware limitations. These two challenges lead to competing requirements in the estimation of the model parameters that involve derivative calculations. These derivative calculations can amplify the already high noise and deteriorate the measurements due

to large random errors. However, reducing the noise by simple smoothing methods is also challenging because they reduce the measurements' spatial resolution and increase systematic errors in the derivative estimates. Therefore, a data processing procedure was employed to achieve an optimal tradeoff between the measurements' systematic and random errors.

The processing steps used to model the vorticity generated due to shock curvature from the schlieren images are summarized in Figure 4.3. Each schlieren experiment captured 990 pre-triggered images of the background and 10 images after the spark discharge. The mean of the pre-triggered images was subtracted from the first image of the shock after it had separated from the hot gas kernel, approximately  $3.5 \mu\text{s}$  after the spark. The background-subtracted image was then flipped along the center of the electrode gap and averaged. The new shock image was used to detect the shock outline and calculate the shock velocity.

#### **4.3.2.1 Shock outline detection**

The shock outline was detected using a Gaussian subpixel fitting scheme. Since these methods are sensitive to noise, we developed a cross-correlation based method to mitigate this effect, as image noise is expected to be uncorrelated across pixels in the image. To detect the shock outline, each row of pixels in the shock image was cross-correlated with the first row of pixels containing the shock by first replicating the single row of pixels to create a 2D intensity map which was 16 pixels in height (Figure 4.3 (a)). We applied a 50% Gaussian window [49] to the 2D map of intensities and cross-correlated the intensities using Robust Phase correlation [48], [50] to determine the displacement of the shock and define the shock outline. The ensemble cross-correlation was calculated along the columns of each 2D map, and a least-squares Gaussian fit to the cross-correlation peak was used to obtain the subpixel location of the shock profile along the horizontal direction for each row of pixels. We then smoothed the shock profile using a moving linear regression.

We used the shock profile (Figure 4.3(b)) to calculate the shock angle and shock curvature. The shock angle (Figure 4.3(c)) was calculated as the arctangent of the derivatives of the  $r$  and  $z$  locations of the shock outline, with the derivatives calculated using a 4<sup>th</sup> order compact noise

optimized Richardson extrapolation scheme[72]. The shock angle and the Euclidean distance between velocity grid points were used to calculate the shock curvature (Figure 4.3(d)).

#### **4.3.2.2 Shock velocity calculation**

The shock velocity was calculated similarly to the shock outline, using cross-correlation based methods to mitigate the effect of image noise and Gaussian subpixel fitting schemes to calculate the subpixel shock displacement. To determine the normal shock velocity, we cross-correlated successive shock images recorded at  $3.5 \mu\text{s}$  and  $4.9 \mu\text{s}$  after the spark. The interrogation windows had a height of 16 pixels, containing 16 points of the shock outline and the orientation of the window was determined using the slope of the line perpendicular to the center shock point in the window. We applied a 75% overlap and a 50% Gaussian window to the original window size, resulting in a window resolution of 8 pixels in height and grid resolution of 2 pixels corresponding to 0.16 mm. The intensities in the same window from the first and second time steps were cross-correlated using Robust Phase correlation to determine the normal shock velocity. The ensemble of the cross-correlation plane obtained for the shock velocity calculation was calculated, and a least-squares Gaussian fit to the cross-correlation peak was used to determine the subpixel shock displacement.

#### **4.3.2.3 Shock generated vorticity calculation**

The tangential shock velocity (Figure 4.3(f)), shock angle, shock curvature, and the density ratio (Figure 4.3(g)), which was calculated from the normal shock Mach number, were used to calculate the spatial variation of the vorticity jump across the shock (Figure 4.3(h)) according to Equation 4. All results were non-dimensionalized using the induced velocity and density behind the shock, calculated according to [17], [74], and the characteristic length scale was taken to be half the electrode gap distance (2.5 mm). Further details on the non-dimensionalization can be found in prior work [80].

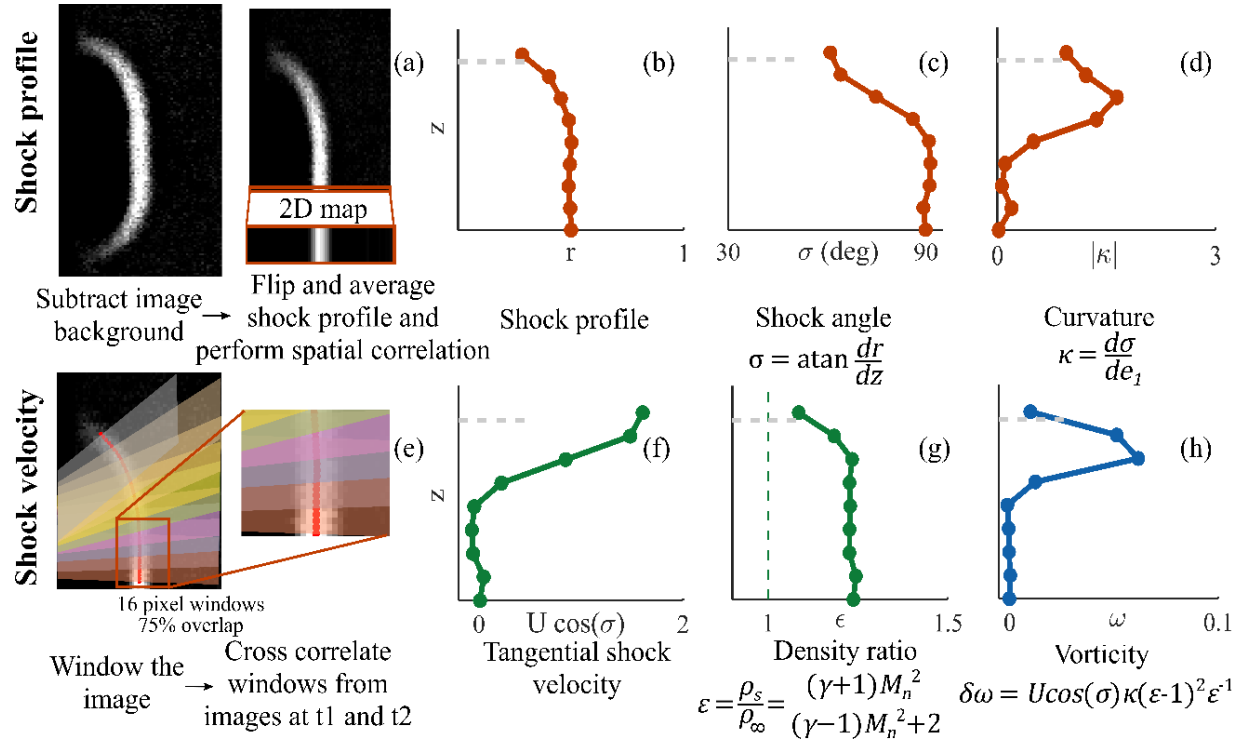


Figure 4.3: Processing steps used to calculate the vorticity jump across a shock wave using images obtained from schlieren experiments. The  $z$ -location of the electrode tip is shown as a gray dashed line.

### 4.3.3 Uncertainty quantification

As mentioned earlier, the high image noise levels and derivative calculations lead to an amplification of the uncertainties in the vorticity estimates. Experimental uncertainties in the displacement field used to estimate both the shock profile and the shock velocity were calculated using the moment of correlation (MC) method [65], then propagated through the shock-generated vorticity calculations using the Taylor series-based propagation method [76]. The maximum uncertainties in the calculation of  $r$  and  $z$  for the shock profile were 0.03 mm and 0.04 mm, respectively, corresponding to 1.2 % and 1.6 % of the half-gap distance (2.5 mm). The maximum uncertainties for the shock velocity calculation were 20 m/s, corresponding to 5 % of the maximum velocity, 412 m/s. The modeled vorticity jump uncertainties ranged from 20% to 60% of the vorticity jump value, with the majority (~70%) of the vorticity jump uncertainties being less than 40% of their respective vorticity jump values.

## 4.4 Results and discussion

### 4.4.1 Shock wave induced by spark discharge

An example of the flow field induced after a single spark discharge generated under quiescent conditions in a 5 mm electrode gap and corresponding to a deposited energy of 4.8 mJ is presented in Figure 4.4(a). The flow field shown spans approximately  $10 \mu\text{s}$  and is comprised of a cylindrical hot gas kernel and a shock wave, trailed by expansion waves. In the first snapshot at  $t/\tau = 0.3$ , the shock wave has completely separated from the induced hot gas kernel. The shape of the shock wave resembles that shown in the schematic in Figure 4.1, where the parts of the shock closest to the electrodes are curved, while the parts near the center of the electrode gap are cylindrical. The normal Mach number along the shock ranges between 1.05 to 1.2, with the normal shock velocity decreasing along the length of the shock from the center of the electrode gap out toward the electrode tips. The Mach number in the center region of the gap remains approximately constant at 1.2. The shape of the Mach number profile (not shown) follows that of the shock outline and resembles the density jump profile shown in Figure 4.5(d).

The first time step shown in Figure 4.4(a) is used to calculate the vorticity jump across the shock because the progressive reduction in the magnitude and non-uniformity of the shock velocity will lead to negligible vorticity production at later times. The shock-generated vorticity estimated using the model is compared to the vorticity calculated directly from a separate set of S-PIV experiments from prior work [95]. An example of the vorticity field induced at later times is shown in Figure 4.4(b), where a pair of vortex rings are generated near the electrode tips.

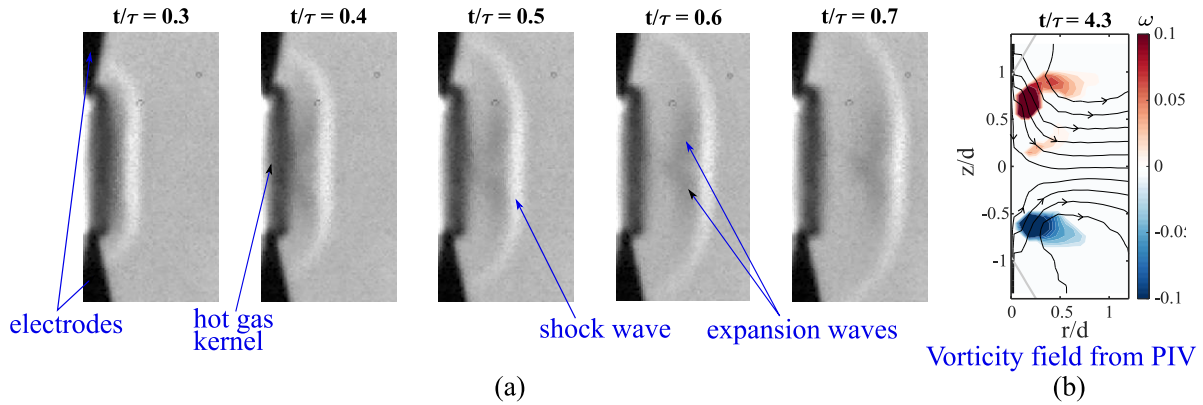


Figure 4.4: (a) Time evolution of a shock wave induced by a single spark discharge (4.9 mJ energy and  $\tau = 14 \mu\text{s}$ ) between two electrodes (5mm gap). (b) Vorticity field measured in prior work for a similar spark discharge (5 mm gap, 4.8 mJ,  $\tau = 14.1 \mu\text{s}$ ) showing a pair of vortex rings generated near the electrode tips[95].

#### 4.4.2 Vorticity estimation based on shock curvature

The spatial profiles of the parameters used to calculate the vorticity jump across the spark induced shock are shown in Figure 4.5 and normalized by their maxima. The profiles calculated from each schlieren experiment are overlaid in the same figure. The orange profiles show quantities calculated using the shock profile, the green profiles show quantities calculated using a combination of the shock profile and shock velocity, and the blue profiles show the vorticity.

The shock outlines in Figure 4.5(a) are seen to be curved in all tests, with the curvature in Figure 4.5(b) being close to zero near the center of the gap and highest near the electrodes (the  $z$ -location of the electrode tip is shown by the gray dashed line). The tangential shock velocity (Figure 4.5(c)) increases monotonically from the center of the shock ( $z = 0$ ) to the ends of the shock near the electrodes. The density ratio term (Figure 4.5(d)), which represents the shock's strength, is almost constant near the center region of the shock and decreases as we move closer to the electrodes, corresponding to a decrease in the normal Mach number. The density ratio profile is the same as that of the normal shock velocity (not shown), both roughly resembling the shock profile. Combining the first 4 terms into Equation 4 gives the final vorticity jump across the length of the shock (Figure 4.5(e)), with negligible vorticity generated near the center of the gap and the peak vorticity being generated in the region of highest curvature.

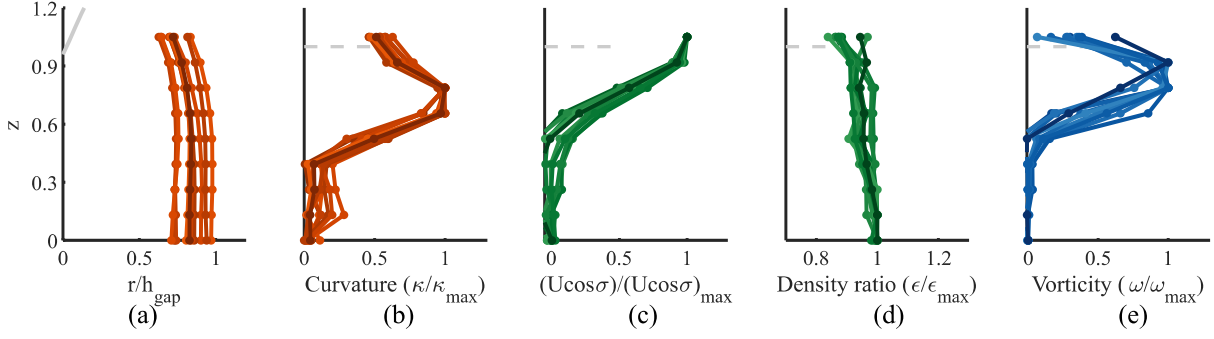


Figure 4.5: Normalized spatial variation of shock properties: (a) shock profile, (b) curvature, (c) tangential velocity, (d) density ratio, and (e) vorticity jump across the shock. Orange profiles are calculated using the shock profile, green profiles using a combination of the shock profile and the shock velocity. The  $z$ -location of the electrode tip is shown as a gray dashed line.

#### 4.4.3 Comparison of shock-estimated vorticity to experimental results from S-PIV

For all the experiments, the peak vorticity is determined for comparison to the S-PIV results from prior work. The shock parameters calculated from the schlieren and S-PIV measurements are plotted against the analytic, normalized pressure gradient across the shock, calculated from the energy deposited in the electrode gap. This allows for comparing two independent measurements while demonstrating the effect of the analytic shock strength and energy deposited in the gap on the different parameters. The analytic, normalized pressure gradient, like the density ratio calculated in the previous section, is also a measure of the strength of the shock wave, although the density ratios calculated in this study are all obtained directly from the schlieren images. The analytic, normalized pressure gradient and analytic shock strength will be used interchangeably.

The analytic, normalized pressure gradient across the shock is related to the electrical energy deposited in the electrode gap and is calculated according to Jones *et al.* [74] as:

$$\frac{p_2 - p_1}{p_1} = \frac{2\gamma}{\gamma + 1} (M_1^2 - 1) = \frac{2\gamma}{\gamma + 1} \frac{0.4503}{\left(1 + 4.803 \left(\frac{r}{R_0}\right)^2\right)^{\frac{3}{8}} - 1} \quad (6)$$

where the subscripts 1 and 2 represent conditions upstream and downstream of the shock, respectively, and  $r$  is the radial distance at which flow properties behind the shock are measured.

In the present context, the radial distance is half the electrode gap distance (2.5 mm). The variable  $R_0$  is the characteristic radius determined by the initial conditions and is given by:

$$R_0 = \left[ \frac{4E_0}{3.94\gamma p_1} \right]^{\frac{1}{2}} \quad (7)$$

where  $E_0$  is the electrical energy deposited by the plasma per unit length of the electrode gap. The analytic, normalized pressure gradient (analytic shock strength) increases with an increase in electrical energy deposited in the gap.

Figure 4.6 shows the peak vorticity and peak curvature locations and the shock curvature, tangential velocity, and density ratio which determine the peak vorticity as a function of the analytic pressure gradient. The peak vorticity location and the tangential shock velocity at peak vorticity show no clear dependence on the analytic shock strength. The peak vorticity location is roughly the same for almost all experiments, occurring near the peak curvature location. The shock curvature at the locations of peak vorticity show a weak dependence on the analytic shock strength, while the density ratio increases with the analytic shock strength, as expected.

These results show that the density ratio estimates calculated from the schlieren images can capture the expected increase in density ratio, which is a measure of the experimentally calculated shock strength, with an increase in the electrical energy deposited. We also demonstrate using these results that stronger shocks tend to have higher maximum curvature (smaller radius of curvature) than weaker shocks. The curvature values in the region of peak vorticity range from approximately 1 to approximately 1.7.

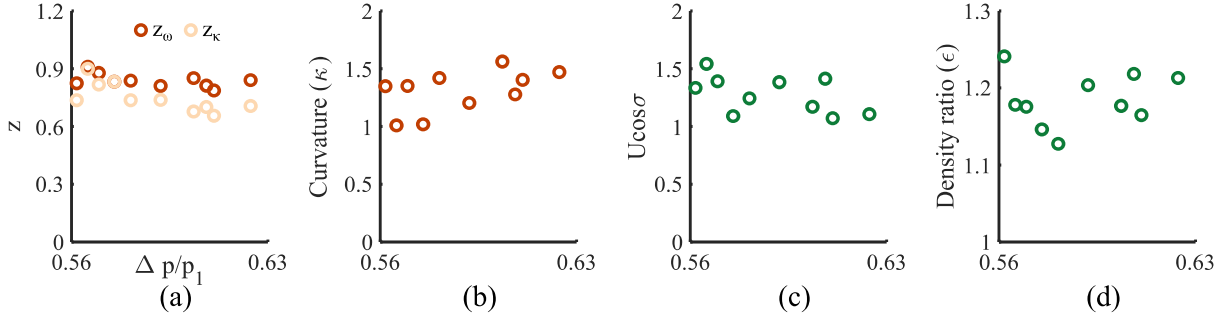


Figure 4.6: (a) The locations of peak vorticity ( $z_\omega$ ) and peak shock curvature ( $z_\kappa$ ) and (b) shock curvature, (c) tangential velocity, and (d) density ratio values used to calculate the maximum vorticity jump across the shock as a function of the analytic, normalized pressure gradient.

The peak shock-generated vorticity jump obtained from the schlieren images is compared to the mean vorticity within the vortex rings from S-PIV experiments described in prior work [95]. The velocity field obtained from S-PIV was flipped and averaged along the  $z = 0$  axis to obtain a single coherent structure representing the vortex ring's core in each experiment. The peak shock-generated vorticity and the mean vorticity calculated in the vortex rings are compared in Figure 4.7. The median values are 0.046 and 0.05 from the shock and vortex rings, respectively. This shows that the vorticity from the model based on shock curvature and the vorticity in the vortex rings are statistically equivalent over the range of experiments performed in this study. This suggests that the shock curvature contributes to the vorticity observed in the vortex rings at later times.

However, there is considerable scatter in the vorticity values and a negligible dependence on the analytic pressure gradient. Further, the S-PIV and schlieren measurements are from different experiments, and some of the variability is likely due to the stochastic nature of the spark discharge as well as the high uncertainties in the shock-generated vorticity estimates. Additionally, the schlieren measurements are taken at approximately  $3 \mu\text{s}$ , whereas the first PIV measurements are taken at approximately  $30 \mu\text{s}$  and local values of vorticity can be altered post generation [108], further explaining the model and experiment's mismatch and limiting a direct comparison.

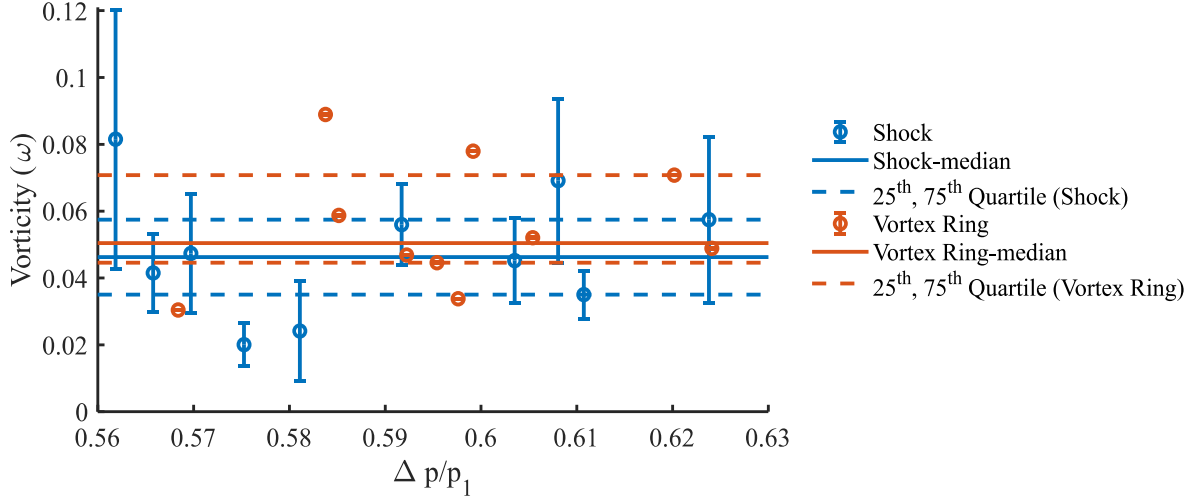


Figure 4.7: Comparison between the non-dimensionalized peak vorticity estimated from the schlieren images with a curved shock model and mean vorticity from PIV measurements.

## 4.5 Conclusions

The flow field induced by a single spark discharge consists of a curved shock wave that propagates radially outward, leaving behind a region of hot gas and vortex ring(s) which drive the cooling and expansion of the hot gas kernel. We use schlieren experiments to capture the shock and develop an image-processing procedure that mitigates the effects of high image noise and low spatial resolution to extract the shock properties. We use the shock properties to estimate the shock-generated vorticity and compare it to the vortex ring vorticity.

The ultra-high-speed recording (700,000 fps) used to obtain the schlieren images leads to high image noise levels, and hardware limitations lead to the low spatial resolution of the recorded images. To achieve an optimal tradeoff between the systematic and random errors in the measurements, we employ a cross-correlation based image processing procedure to extract the shock outline and shock velocity and use Gaussian subpixel fitting schemes commonly used in PIV to provide high spatial resolution. The shock outline is used to calculate the shock curvature and shock angle, while the shock velocity is used to calculate the density ratio, all of which are inputs to the model used to estimate the vorticity jump across the shock wave.

This work shows that the shock profile is approximately cylindrical in the center of the gap with nearly zero curvature, with the shock curvature increasing towards the electrodes and reaching peak curvatures of approximately  $\kappa/\kappa_{gap} = 1.7$ . The normal shock Mach number is highest near the center of the gap, close to Mach 1.2, and decreases near the electrodes to approximately 1.05. The peak values of both the shock Mach number and curvature increase with the analytic pressure gradient, which is related to the electrical energy deposited in the gap. The magnitude of the tangential velocity increases along the shock, and the peak tangential velocity shows no clear dependence on the analytic pressure gradient. The vorticity calculated using the model is close to zero at the center of the gap and progressively increases along the shock towards the electrode tips. The highest vorticity is observed in the regions of the highest shock curvature, with the peak vorticity showing no clear dependence on the analytic pressure gradient. These results are similar to CFD simulations [32] showing the presence of vortices in the region where the shock wave curvature is highest.

The shock-generated vorticity is compared to the vorticity from experimental S-PIV results from previous work [95] with both shown to be statistically equivalent. This suggests that the shock wave induced at early times ( $< 20 \mu\text{s}$ ) contributes to the vorticity in the vortex rings that control the cooling and dynamics of the hot gas kernel at later times ( $> 50 \mu\text{s}$ ). The work is limited in that the schlieren and PIV measurements were non-simultaneous, and the time at which the vorticity is calculated from the model is an order of magnitude lower than the first snapshot of vorticity from the PIV experiments.

We show that the vorticity induced by a spark discharge may be approximated from the shock curvature and velocity using qualitative schlieren experiments and used to obtain an initial estimate of the strength of the vortex rings, having implications in the late stages of the flow field. In the case of pin-to-pin discharges, an estimate of the vortex rings' strength can be used to approximate the rate of cooling [80], [95]. Controlling the strength and location of peak curvature of the shock wave induced at early times can affect the late stages of flow field dynamics.

## 5. TOWARDS 3D VELOCITY MEASUREMENTS IN SPARK INDUCED FLOWS

### *Abstract*

The 3D flow field induced by spark discharges is measured using the tomographic particle image velocimetry technique. The complexities of measuring this flow field due to the low aspect ratio (thick laser volume), non-uniform seeding, large displacements and limited number of cameras results in particle clustering and therefore poor volume reconstructions of the flow field. Preprocessing techniques to mitigate the clustering are tested on synthetic data and used to improve the image quality of the recorded images from the spark experiment. One of the two induced vortex rings are captured from these measurements, and improvements to future experiments are suggested.

### 5.1 Introduction

Spark plasma discharges are characterized by the formation of a thin ionized channel generated by random and chaotic electron avalanches that result in the breakdown of the gas in which the spark is formed. The flow field induced by a spark discharge consists of a shock wave that propagates radially outward leaving behind a hot gas kernel and vortex ring(s) [17], [80], [95], [96]. The vortex rings entrain ambient gas and cool the hot gas kernel, with the strength and dynamics of the vortex rings determining the extent and rate of cooling of the hot gas kernel [95].

Numerical investigations of the flow field induced by spark discharges have so far been limited to axisymmetric assumptions in CFD simulations [24], [29]–[31], [109] while experiments have been limited to 2D measurements of the induced flow field [17], [80], [95], [96]. We recently performed experimental investigations of the spark induced flow field and developed a model to quantify the cooling due to ambient gas entrained by a pair of vortex rings, where the assumption of axisymmetric rings was also made [95]. Although the assumption that the flow induced by a spark generated between a pair of identical electrodes with cone-shaped tips is axisymmetric may be justified by the electrode configuration, CFD simulations have shown that even in purely 2D electrode geometries the flow can evolve into a highly three dimensional flow field [30]. Further,

our recent work studying the cooling of the hot gas kernel by the vortex rings showed a mismatch between a density-based calculation of the cooling rate of the hot gas kernel and an entrainment-based one which relied on the assumption of axisymmetric vortex rings [95]. It is likely that this mismatch is due to the three-dimensional nature of the induced flow field.

In this work, we use high speed, time resolved, tomographic particle image velocimetry (tomo-PIV) measurements to measure the flow field induced by a single spark discharge generated between a pair of electrodes. The low aspect ratio of the measurement volume (thick laser volume) needed to completely capture the vortex rings, non-uniform seeding density that arises from the entrainment of ambient fluid into the laser volume by the vortex rings, and the large dynamic range of the induced velocities create difficulties in the volume reconstruction and 3D velocity calculation of the spark induced flow. Our preliminary results capture one of the two induced vortex rings and we provide recommendations to progress the development of future experimental studies of the spark induced flow using tomo-PIV.

## 5.2 Experimental methods and techniques

A single spark discharge was generated using a nanosecond high voltage pulser in a 5 mm gap between two ceriated-tungsten electrodes with cone-shaped tips. Details on the plasma generation are given in prior work [80].

### 5.2.1 Tomographic particle image velocimetry experimental set-up

A schematic of the tomo-PIV system is shown in Figure 5.1. The system consisted of a QuasiModo quasi-continuous burst-mode (QCBM) Nd:YAG laser [89], three high-speed Photron SA-Z cameras, and an acrylic test section containing the electrodes. The laser was operated at 50 kHz, and laser sheet optics produced an approximately 3 mm thick and 4 mm high laser volume in the region where the spark discharge was generated. The center camera (Camera 2) was oriented perpendicular to the region of interest with the two outer cameras subtended in the  $x$ - $z$  plane having angles of approximately  $\pm 25^\circ$  to the center camera. The outer cameras were operated with Nikon AF FX Micro-Nikorr 200 mm lenses,  $f\# 32$ , the center camera with a Nikon Nikorr 105 mm lens, 2x teleconverter,  $f\# 22$  and all three cameras recorded particle images at a sampling rate of 50 kHz.

The resolution for the cameras was approximately  $640 \times 600$  pixels, corresponding to an approximate field of view of  $5.7 \times 5.4$  mm. Alumina particles were injected into the test enclosure with diameters of about  $0.3 \mu\text{m}$  and an estimated Stokes number of approximately 0.002. A delay generator was used to synchronize and trigger the laser, cameras, and the high voltage pulser.

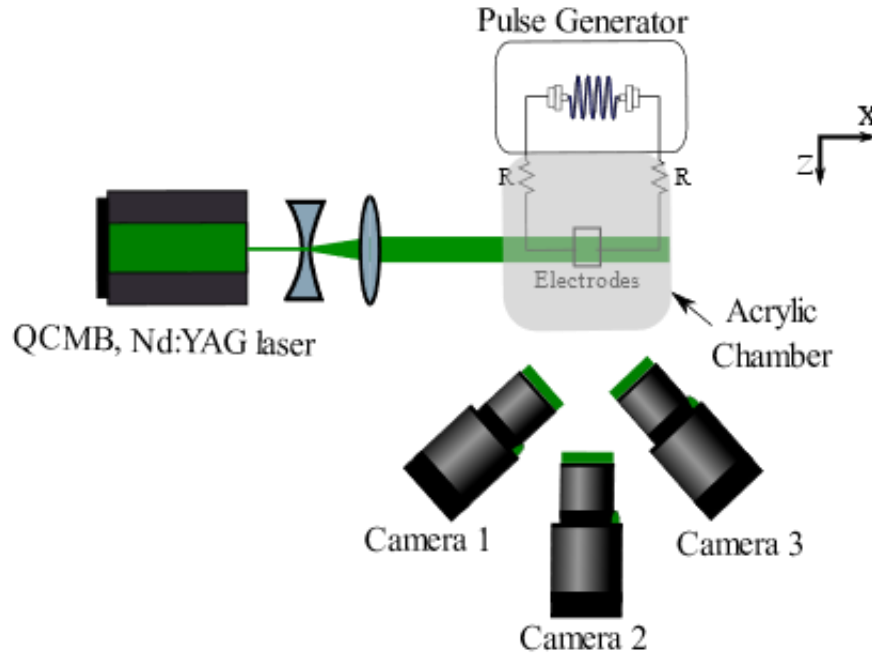


Figure 5.1: Schematic of the experimental set-up for tomographic PIV measurements of the plasma-induced flow field.

## 5.2.2 Image processing

### 5.2.2.1 Calibration

The recorded particle images were processed using DaVis 10.0 software developed by LaVision Inc. A calibration was first performed using a 2D calibration plate which consisted of dots of diameter  $0.125$  mm and spacing  $0.25$  mm that was traversed across the measurement volume in increments of  $0.635$  mm, between  $z = -3.8$  mm to  $z = 3.8$  mm to calculate the mapping function of the camera. The camera coordinates and physical coordinates were fitted using a 3<sup>rd</sup> order polynomial in the  $x$  and  $y$  directions. The calibration error was approximately  $0.2$ - $0.3$  pixels for each camera. A volume self-calibration procedure [110] was then followed to account for misalignments due to inaccuracies in the calibration or slight movements of the cameras between

the calibration and acquisition of particle images and the mapping function was corrected accordingly. The volume self-calibration reduced calibration errors to between 0.02-0.03 pixels.

### **5.2.2.2 Image pre-processing**

The particle images of the spark induced flow suffered from non-uniform seeding resulting in particle clusters in the regions of entrained fluid. A thick laser volume was required to capture the full vortex rings whose approximate radius had been previously found to range from 2-3 mm before collision [80], [95]. The thick laser volume and the entrainment of particles from the surrounding regions by the vortex rings resulted in regions of high seeding density and particle clusters in the vortex rings. The particle clusters of size 6-9 pixels essentially resulted in regions with large particle diameters and this, combined with the seeding density in the jet region of the flow ( $\text{ppp} = 0.018$ ), resulted in large source densities ( $N_s$ ) on the order of 0.5-1.14. As expected, these factors made the volume reconstruction with the 3 camera views difficult [111], [112] and increased the likelihood of reconstructing ghost particles (particles that do not exist in the flow field, but are formed due to poor reconstruction) which can result in a bias error in the velocity measurements [113]. The ghost particles from the resulting poor reconstruction appear as smeared or blurred regions in the reconstructed volume.

In order to mitigate the effect of the regions with clustered particles in the particle image on the volume reconstruction, preprocessing techniques that would effectively reduce the particle cluster sizes were tested. Image sharpening and using a sliding window to subtract the local minimum value were tested with different filter sizes. The sharpening technique works by first blurring the original image, typically using a gaussian filter whose diameter can be varied and then subtracting the blurred image from the original. The gaussian filter diameter should be chosen such that it can capture the highest intensity variation that needs to be eliminated from the image to be sharpened. The sliding minimum window is used to locally threshold the particle images thereby acting to de-cluster the heavily seeded regions of the image. In the case of the spark images, the particle sizes were on average 7 pixels in diameter, and a filter size of 9x9 pixels, combined with a 3x3 sliding minimum filter size was applied to the particle images obtained from the spark experiment with the goal of improving reconstruction quality. Details on how these filter sizes were determined is given in the Appendix of this chapter.

### **5.2.2.3 Volume reconstruction and velocity estimation**

In this work, we used algebraic reconstruction methods to reconstruct the particle volume and calculate the velocity fields. The method used is known as the multiplicative algebraic reconstruction technique (MART) which iteratively reconstructs the 3D particle intensity field from the 2D projections of each camera [111], [112], [114]. After the volume reconstruction, a 3D cross correlation was performed to calculate the 3D velocity field.

A total of 10 MART iterations were used to reconstruct the volume, followed by a 3D cross correlation with a total of 4 passes of window size  $96 \times 96 \times 96$  voxels and overlap of 75%, with each pass validated by universal outlier detection (UOD) [115] and thresholded to keep vectors with correlation coefficient values above 0.1. The grid resolution of these measurements was approximately 0.2 mm.

## **5.3 Preliminary results**

### **5.3.1 Volume reconstruction from MART**

The particle images recorded from the spark experiment were reconstructed and a comparison of the projections from the raw and preprocessed results is shown in Figure 5.2. The smearing effect mentioned previously is observed in the raw images from the spark data, with the particle clustering concentrated in the regions with the spark induced vortex rings. Applying the combined preprocessing significantly reduces the smearing in all projections.

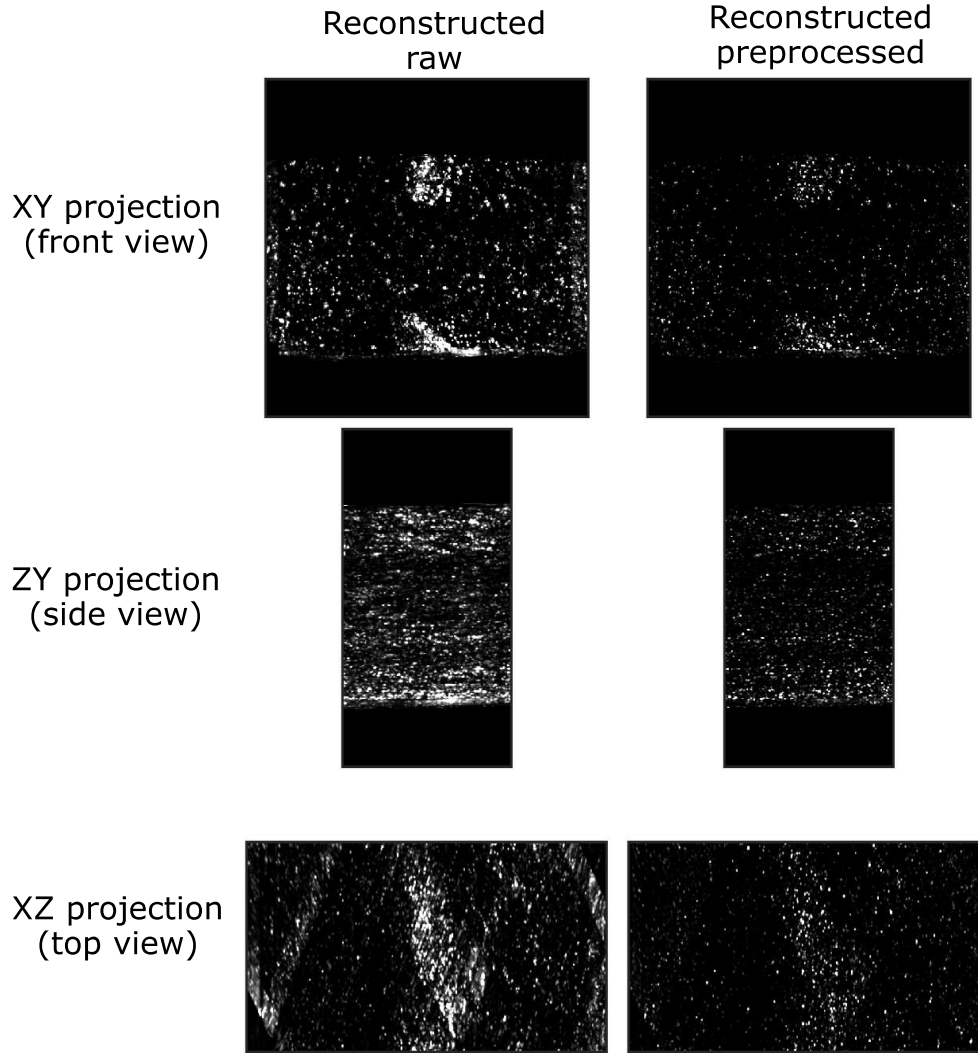


Figure 5.2: XY, ZY and XZ projections of the reconstructed volume from raw images and the reconstructed volume from the preprocessed images of the spark experiment.

### 5.3.2 3D velocity field

The results from the 3D cross correlation of the reconstructed volumes approximately  $120 \mu\text{s}$  after the spark are shown in Figure 5.3. An isometric view of the induced flow field showing the coherent vorticity in green and the velocity vectors colored by their magnitude is given in Figure 5.3(a). The XY (front view), ZY (side view) and XZ (top view) projections of the velocity field are given in Figure 5.3(b). The electrodes (not shown in the plots) are located at  $X = 0$ ,  $Y = \pm 2.5 \text{ mm}$ ,  $Z = 0$ . Based on our previous work, we expect the flow field at this time to include

two vortex rings at the top and bottom and entrainment of ambient gas by the rings. The results show the top vortex ring and entrainment with peak jet velocities of 8 m/s through the top ring. The bottom ring, however, is not captured in these measurements, and results from later time steps do not capture a clear bottom vortex ring either, primarily due to the increased clustering in the lower portion of the images.

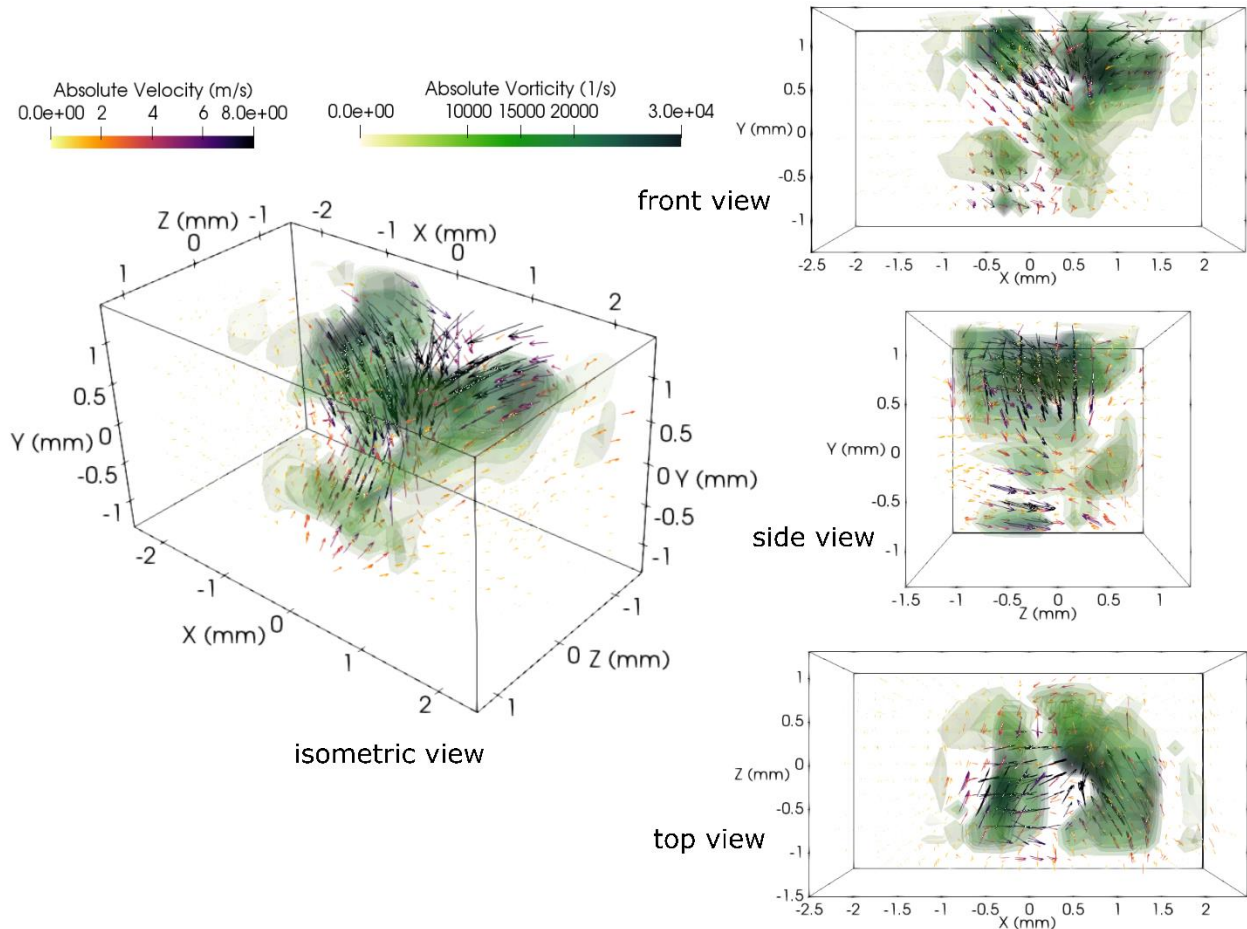


Figure 5.3: (a) Isometric view and (b) front, side and top views of 3D vorticity field (contours) and velocity field (vectors) of the spark induced flow.

#### 5.4 Summary and recommendations

The complex flow field induced by spark discharges is difficult to measure. In this work, we conduct volumetric flow measurements using tomo-PIV with 3 cameras and a thick laser sheet to capture the full 3D shape of the vortex rings. The experiment is limited by the high seeding densities in the regions of the flow containing the vortex rings, low aspect ratio (thick laser volume)

and the use of only 3 cameras, all of which present difficulties in reconstructing the 3D volume. Preprocessing techniques are tested on synthetic images replicating the characteristics of the spark experiment and then implemented in the analysis of the spark experiment data to improve the image quality and reconstruction. The results show the presence of a top vortex ring, however, due to the coarse resolution of the measurements, necessitated by regions of low particle concentrations, we are unable to capture the full top ring with finer detail. The bottom vortex ring is not captured, primarily due to the limitations of the experiment.

These first 3D measurements of the complex spark induced flow field allow us to provide a framework to improve future experiments. The main issues of high seeding density, leading to clustering in the region of the vortex rings, can be mitigated by using a thinner laser sheet to capture half the diameter of the vortex rings instead of the full diameter. This will reduce the number of particles within the laser volume, reducing the clustering effect while still allowing for the assessment of the ring symmetry by evaluating half the vortex ring. Further improvement to the clustering may be achieved with smaller particles, which would result in smaller clusters. Increasing the number of cameras to 4 or 5 would further improve the reconstruction quality [111], [112].

A second method, known as the shake the box technique (STB), is also commonly used to obtain the velocity field from tomo-PIV images. In this method, the particle locations from the first time step are used to predict particle locations in the subsequent time step, where the particles are “shaken” into their predicted locations and their position is iteratively corrected. The STB technique uses the velocity information from tracking the particles in time, to improve their identification at subsequent time steps [116]–[119] and has been shown to reduce ghost particles [117], [119] while being more computationally efficient than MART. However, the STB technique is limited when there are large, non-uniform displacements, due to the difficulties in identifying overlapped particles [116], [117]. Therefore, another possible improvement to future experiments could involve increasing the recording speed (e.g. doubling the speed to 100 kHz) which would enable the use of the STB technique to track the particles, as the maximum displacement would be reduced from 16 pixels to 8 pixels between frames. To compensate for the reduced resolution from

the increased speed in recording, the field of view can be limited to the top or bottom half of the flow field, capturing either the top or bottom vortex ring.

### ***Appendix***

In order to assess the effectiveness of a variety of pre-processing techniques and determine which techniques resulted in the largest improvement in the volume reconstruction of the particle images, synthetic images representative of the experimental images were utilized. The simulated experiment used to generate the synthetic images mimicked the actual spark experiment, in terms of camera angles, magnification and depth of the laser volume. The synthetic images were also used to replicate similar particle densities as the spark experiment. Particle clusters were created in the center of the images, by distributing the particle concentration such that the background had a constant seeding level of 0.0008 ppp and two spherical regions of diameter 1.5 mm in the top and bottom center of the image volume contained seeding levels of 0.02 ppp.

The reconstruction quality was calculated according to [111] to assess the effect of the preprocessing techniques on the resulting volume reconstruction. The reconstruction quality is given by Equation 5.A.1.

$$Q = \frac{\sum_{X,Y,Z} E_1(X, Y, Z) \cdot E_0(X, Y, Z)}{\sqrt{\sum_{X,Y,Z} E_1^2(X, Y, Z) \cdot \sum_{X,Y,Z} E_0^2(X, Y, Z)}} \quad (5.A.1)$$

where  $E(X, Y, Z)$  is the intensity of a 3D array of cubic voxel elements in  $(X, Y, Z)$  and the subscripts  $0$  and  $1$  represent the exact intensity volume and the reconstructed intensity volume respectively.

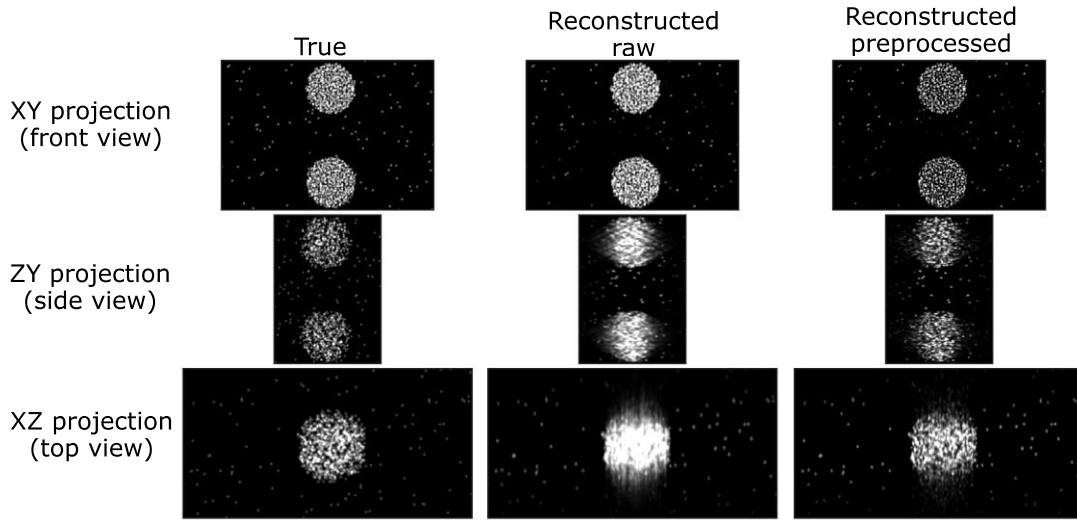
To create the exact 3D volume, the intensity distribution of the source points was approximated as 3D a Gaussian centered at the particle location with the standard deviation set to be  $1/4^{\text{th}}$  of the particle diameters used in the image generation and peak intensities scaled with the bit depth of the camera. The reconstruction quality of for the full 3D volume from the raw images was 0.64.

The preprocessing techniques tested in this work focused on methods that would de-cluster the heavily seeded regions of the images. A sharpening filter and subtracting a sliding minimum window were the two preprocessing techniques tested. The diameter of the gaussian used to blur the original image for the sharpening filter was varied from 9-33 pixels. The sliding minimum windows were varied from 3x3 pixels to 33x33 pixels. The 9-pixel filter used for the sharpening gave the highest reconstruction quality of 0.72, and though the larger window sizes had lower reconstruction quality, the difference was negligible ( $<0.2$ ). Subtracting a sliding minimum window also improved the reconstruction quality with the maximum improvement resulting from a 17x17 pixel window with a Q value of 0.68. If a more severe thresholding is needed to de-cluster the particles, smaller sliding minimum window sizes should be considered.

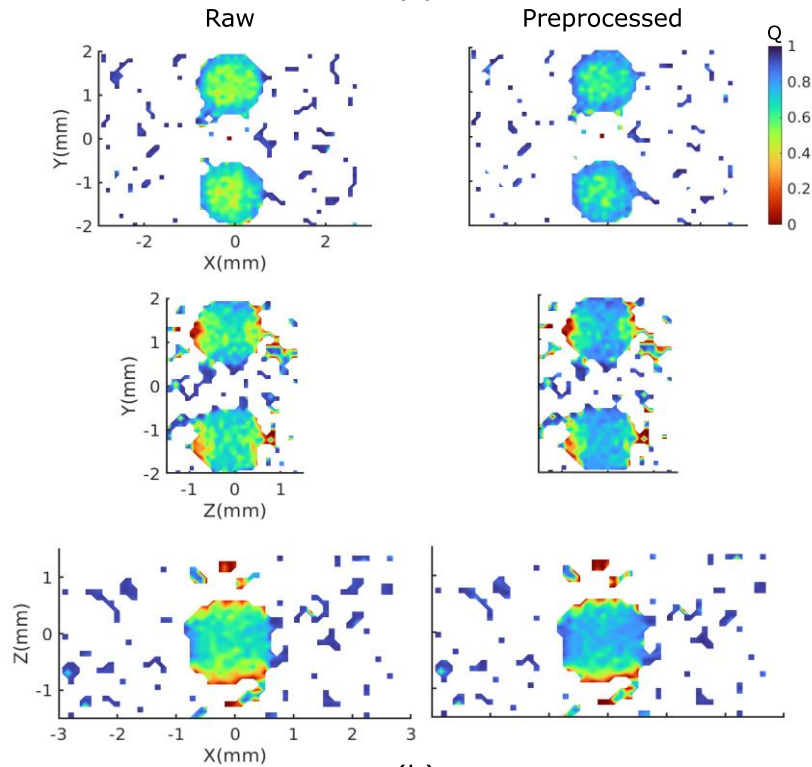
Combining the 9-pixel sharpening filter and the local thresholding from the 17x17 pixel sliding minimum window resulted in the highest increase in reconstruction quality for the synthetic images, of 0.74.

A summary of the results from the pre-processing are shown in Figure 5.4. Figure 5.4(a) shows the XY, ZY and XZ projections of the true intensity field, the reconstructed volume from the raw images and the reconstructed volume from the pre-processed images. The two spheres located in the top and bottom center of the volume have higher particle concentrations than the background and a smearing effect (elongations/blurring of particles) in those regions is observed in the raw images. After the preprocessing is applied, the particle smearing in the reconstructions, although not completely absent, is reduced. Figure 5.4(b) shows a spatial map of the reconstruction quality, calculated over each projection. Regions that are white did not have any particles and are therefore NaN values. The reconstruction quality in the raw images ranged from 0 at the edges of the sphere clusters, meaning no particles in those regions were truthfully reconstructed, to 0.99 outside the cluster regions. The average reconstruction quality for the full 3D volume was 0.64, with 75% of the volume having reconstruction qualities greater than or equal to 0.64 and the majority of the lowest values of reconstruction quality concentrated within the regions with particle clusters. After the preprocessing, the minimum reconstruction quality was still 0 at some of the edges of the cluster, the maximum reconstruction quality was 0.99 and the overall reconstruction quality

increased to 0.74, with 75% of the volume having reconstruction qualities greater than 0.74, primarily due to the improved reconstruction within the cluster.



(a)



(b)

Figure 5.4: (a) XY, ZY and XZ projections of the true intensity volume, the reconstructed volume from raw images and the reconstructed volume from the preprocessed images of the synthetic data. (b) A spatial map of the reconstruction quality of the projections with the raw images and the preprocessed images.

## 6. CONCLUSION

### 6.1 Summary

This work used quantitative experimental measurements and reduced order modeling to study the flow field induced by a single nanosecond spark discharge produced in air under quiescent conditions. A nanosecond, electrical spark was generated between a pair of conical-tipped electrodes using a high voltage pulse generator. The flow field induced by the spark discharge consists of a shock wave at early times ( $< 20 \mu\text{s}$ ) that expands radially outward leaving behind a region of hot gas that cools in time and a pair of vortex rings. A series of experiments was conducted to measure the velocity and density fields induced by the spark using stereoscopic (SPIV) and tomographic (tomo-PIV) particle image velocimetry and background oriented schlieren (BOS), respectively. Using the experiments and reduced order modelling, the following four research objectives were addressed: (1) Quantify the cooling of the hot gas kernel and determine the extent of its convective cooling; (2) Determine the role of the induced vortex rings in entrainment and the cooling of the hot gas kernel and evaluate the effect of energy on the cooling process; (3) Estimate the role of the induced shock wave in the generation of the vortex rings; (4) Perform 3D velocity measurements to assess the symmetry of the induced vortex rings.

The cooling of the hot gas kernel was studied by conducting separate SPIV and BOS experiments to measure the velocity and density of the induced flow field. The density results from BOS showed that the hot gas kernel takes on an initially cylindrical shape, then expands into a torus shape as it cools. The results found that the hot gas kernel cools at two distinct rates, an initially fast cooling regime followed by a slower cooling regime, with the fast cooling regime being almost twice as fast and extending for approximately 1 ms over the range of electrical energy values investigated in this study (approximately 4 - 7 mJ). The velocity measurements confirmed the presence of a pair of vortex rings induced near each electrode tip. The vortex rings propagate towards each other due to self-induction until they collide and then expand radially post collision. The velocity and density measurements in this study were non-simultaneous and thus each realization of the spark induced flow field will be different. Therefore, 25 SPIV experiments and 25 BOS experiments were conducted to compile statistics on the induced flow field. A reduced

order model was developed to relate the total cooling of the hot gas kernel in the fast regime to the amount of entrained fluid within a control volume representing the kernel by considering the rate of change of enthalpy of the kernel. The energy equation was simplified assuming low Mach number, inviscid flow, negligible body forces, negligible heat transfer due to conduction and radiation, and a calorically perfect gas and was then used to calculate the *cooling ratio* parameter. From the point of view of the kernel density, the cooling ratio represents the ratio of the change in kernel density over the fast regime to the initial density deficit with respect to the ambient. From the point of view of entrainment, the cooling ratio represents the time integral of the entrainment of cold gas per unit volume of the hot gas kernel over the duration of the fast regime. A cooling ratio value of 1 indicates the fluid has cooled to the ambient temperature. The cooling ratio parameter was used as a metric to assess the cooling of the hot gas kernel from the BOS density measurements and separately using the entrainment calculated from PIV. The results showed the cooling ratio from the two measurements to be statistically equivalent, validating the hypothesis that the entrainment is leading to cooling of the hot gas. The cooling ratio values showed that almost 50% of the cooling occurred in the fast, convective cooling regime.

The role of the induced vortex rings and the effect of spark energy on the entrainment and cooling of the hot gas kernel was investigated using simultaneous PIV and BOS experiments. A vortex ring cooling model was developed and tested by comparing entrainment and cooling calculated from the model to the experimental values. The filament and thin core vortex rings models were used to estimate the entrainment due to the vortex ring and the theoretical result was compared to the entrainment calculated from the experimental measurements. The results showed that, on average, the entrainment calculated from the model and experiment agreed well, within the experimental uncertainty. The cooling calculations of the model were evaluated against cooling calculated from the PIV and BOS data. The model once again agreed well with the PIV experiment but underpredicted the cooling calculated from the density measurement by about 14%, likely due to the axisymmetric assumptions made in formulating the vortex ring cooling model. Overall agreement in the results showed that the induced vortex rings govern the spatial distribution of the hot gas kernel by driving entrainment of cold ambient gas into the kernel, thereby cooling it. The energy deposited in the electrode gap affected the strength of the vortex rings, as well as the extent

to which the rings and hot gas kernel expanded radially. Stronger vortex rings were induced at higher energy values, resulting in more entrainment and faster cooling of the hot gas kernel.

To understand the role of the induced shock wave in the generation of the vortex ring vorticity, schlieren experiments were used to capture the shock and an image-processing procedure was developed to extract the shock properties. The shock-generated vorticity due to baroclinic torque, was estimated using the shock properties and compared to the vortex ring vorticity measured using SPIV. The schlieren results showed the shock profile to be more curved near the electrode tips than the center of the gap, with peak normal Mach numbers of approximately 1.2. Peak vorticity was generated in the regions of the highest shock curvature, and when compared to the mean vorticity within the vortex rings from the results of the SPIV measurements, the shock generated vorticity and the vortex ring vorticity were found to be statistically equivalent. These results showed that it is likely that the shock wave at early times contributes to the vorticity in the vortex rings that then control the cooling and dynamics of the hot gas kernel at later times.

The 3D nature of the spark induced flow field was investigated using tomo-PIV measurements. The experiment was limited by a thick laser sheet, non-uniform seeding densities that resulted in regions with particle clusters, and only 3 camera views, which made the volume reconstruction difficult. Preprocessing techniques were used to improve the spark image quality and the tomo-PIV results were able to capture one of the 2 induced vortex rings, although with a coarse grid resolution. Using a thinner laser sheet, more camera views, smaller seeding particles, and increasing the acquisition speed to allow for the use of better reconstruction methods would improve future tomo-PIV experiments of the spark induced flow field.

## **6.2 Recommendations for future work**

The present work focused on the flow induced by a single spark discharge and the results from this work can be used by future researchers as a basis for characterizing the 3D flow field with more complex actuator configurations and with different flow conditions. The results from a single spark discharge in quiescent flow can be extended to flow fields where there is both uniform flow and non-uniform flow, and the structure of the vortex rings and the rate of gas cooling can be assessed using the cooling ratio parameter introduced in this work.

In order to get a more complete understanding of the formation of the vortex rings that drive the cooling of the hot gas kernel, it is necessary to capture the flow from the induced shock wave ( $\sim 1 \mu\text{s}$ ), to the formation of the rings ( $\sim 100 \mu\text{s}$ ), with sufficient spatiotemporal resolution. Experimental measurements with sufficient spatiotemporal resolution are difficult in the early stages of the induced flow field, therefore CFD simulations can be used to model the flow field induced by these discharges from the shock generated at early times to the moment the vortex rings are formed. These simulations can be used to investigate the contribution of the induced shock wave and the interaction of the pressure waves behind the shock and the hot gas kernel to vorticity production.

The simultaneous PIV and BOS measurements developed in this work can be extended to study multiple spark discharges pulsed in succession. Future work can start by focusing on the flow field induced by two discharge pulses in succession. The experiments could study: (1) The induced velocity and density field of two successive discharges within the fast cooling regime (this means actuation of the second pulse within less than 1 ms after the first spark); (2) The induced flow field for two successive discharges, with the second discharge after the end of the fast cooling regime. This work can focus on the interaction of the vortex rings from the first and second pulses and use the cooling ratio introduced in this work to determine the extent of cooling before and after the second discharge. Characterizing the coupling between consecutive pulses would allow for recommendations on the optimal pulsation frequency to benefit from the synergetic effect of multiple pulses.

The results of this work showing the spatial extent of the vortex rings and hot gas kernel can also be extended to tomographic PIV and BOS experiments of an array of discharges. The measurements can be used to study the interaction of vortex rings and the three-dimensionality of the flow field when the actuator spacing is less than, equal to, or larger than the gap length.

## REFERENCES

- [1] I. V Adamovich *et al.*, “Plasma assisted ignition and high-speed flow control: Non-thermal and thermal effects,” *Plasma Sources Sci. Technol.*, vol. 18, no. 3, 2009.
- [2] S. M. Starikovskaia, “Plasma assisted ignition and combustion,” *J. Phys. D. Appl. Phys.*, vol. 39, no. 16, pp. R265–R299, Aug. 2006.
- [3] T. C. Corke, C. L. Enloe, and S. P. Wilkinson, “Dielectric Barrier Discharge Plasma Actuators for Flow Control,” *Annu. Rev. Fluid Mech.*, vol. 42, no. 1, pp. 505–529, 2010.
- [4] B. R. Locke, M. Sato, P. Sunka, M. R. Hoffmann, and J. S. Chang, “Electrohydraulic discharge and nonthermal plasma for water treatment,” *Ind. Eng. Chem. Res.*, vol. 45, no. 3, pp. 882–905, 2006.
- [5] Y. G. Utkin, S. Keshav, J. H. Kim, J. Kastner, I. V Adamovich, and M. Samimy, “Development and use of localized arc filament plasma actuators for high-speed flow control,” *J. Phys. D. Appl. Phys.*, pp. 40(3), 685, 2006.
- [6] S. B. Leonov, I. V. Adamovich, and V. R. Soloviev, “Dynamics of near-surface electric discharges and mechanisms of their interaction with the airflow,” *Plasma Sources Sci. Technol.*, vol. 25, no. 6, p. 63001, 2016.
- [7] E. Moreau, “Airflow control by non-thermal plasma actuators,” *J. Phys. D. Appl. Phys.*, pp. 40(3), 605, 2007.
- [8] J. Little, K. Takashima, M. Nishihara, I. Adamovich, and M. Samimy, “Separation Control with Nanosecond-Pulse-Driven Dielectric Barrier Discharge Plasma Actuators,” *AIAA J.*, vol. 50, no. 2, pp. 350–365, Feb. 2012.
- [9] N. Benard and E. Moreau, “Electrical and mechanical characteristics of surface AC dielectric barrier discharge plasma actuators applied to airflow control,” *Exp. Fluids*, vol. 55, no. 11, 2014.
- [10] P. Raizer, Yuri, *Gas discharge physics*. 1991.
- [11] S. Stepanyan, N. Minesi, A. Tibere-Inglesse, A. Salmon, G. D. Stancu, and C. O. Laux, “Spatial evolution of the plasma kernel produced by nanosecond discharges in air,” *J. Phys. D. Appl. Phys.*, vol. 52, no. 29, May 2019.
- [12] M. Akram, “Two-dimensional model for spark discharge simulation in air,” *AIAA J.*, vol. 34, no. 9, pp. 1835–1842, Sep. 1996.
- [13] M. Kono, K. Niu, T. Tsukamoto, and Y. Ujiie, “Mechanism of flame kernel formation produced by short duration sparks,” in *Symposium (International) on Combustion*, 1989, vol. 22, no. 1, pp. 1643–1649.

- [14] M. Thiele, J. Warnatz, and U. Maas, “Geometrical study of spark ignition in two dimensions,” *Combust. Theory Model.*, vol. 4, no. 4, pp. 413–434, 2000.
- [15] S. Au, R. Haley, and P. R. Smy, “The Influence of the Igniter-Induced Blast Wave Upon the Initial Volume and Expansion of the Flame Kernel,” *Combust. Flame*, vol. 88, pp. 50–60, 1992.
- [16] A. Borghese, A. D’Alessio, M. Diana, and C. Venitozzi, “Development of hot nitrogen kernel, produced by a very fast spark discharge,” *Symp. Combust.*, vol. 22, no. 1, pp. 1651–1659, 1989.
- [17] B. Singh, L. K. Rajendran, M. Giarra, P. P. Vlachos, and S. P. M. Bane, “Measurement of the flow field induced by a spark plasma using particle image velocimetry,” *Exp. Fluids*, vol. 59, no. 12, Dec. 2018.
- [18] D. L. Rusterholtz, D. A. Lacoste, G. D. Stancu, D. Z. Pai, and C. O. Laux, “Ultrafast heating and oxygen dissociation in atmospheric pressure air by nanosecond repetitively pulsed discharges,” *J. Phys. D. Appl. Phys.*, vol. 46, no. 46, 2013.
- [19] D. Z. Pai, D. A. Lacoste, and C. O. Laux, “Nanosecond repetitively pulsed discharges in air at atmospheric pressure—the spark regime,” *Plasma Sources Sci. Technol.*, vol. 19(6), 065, 2010.
- [20] S. M. Starikovskaia, “Plasma-assisted ignition and combustion: nanosecond discharges and development of kinetic mechanisms,” *J. Phys. D-Applied Phys.*, vol. 47, no. 35, 2014.
- [21] S. V Pancheshnyi, D. A. Lacoste, A. Bourdon, and C. O. Laux, “Ignition of propane–air mixtures by a repetitively pulsed nanosecond discharge,” *IEEE Trans. Plasma Sci.*, vol. 34, no. 6, pp. 2478–2487, 2006.
- [22] G. L. Pilla, D. A. Lacoste, D. Veynante, and C. O. Laux, “Stabilization of a swirled propane-air flame using a nanosecond repetitively pulsed plasma,” *IEEE Trans. Plasma Sci.*, vol. 36, no. 4 PART 1, pp. 940–941, 2008.
- [23] A. Starikovskiy and N. Aleksandrov, “Plasma-Assisted Ignition and Combustion,” *Prog. Energy Combust. Sci.*, vol. 39, no. 1, pp. 61–110, Feb. 2013.
- [24] F. Tholin and A. Bourdon, “Simulation of the hydrodynamic expansion following a nanosecond pulsed spark discharge in air at atmospheric pressure,” *J. Phys. D-Applied Phys.*, vol. 46, no. 36, 2013.
- [25] S. Lovascio *et al.*, “Effects of pulsation frequency and energy deposition on ignition using nanosecond repetitively pulsed discharges,” *Proc. Combust. Inst.*, vol. 36, no. 3, pp. 4079–4086, 2017.
- [26] S. Adams, J. Miles, T. Ombrello, R. Brayfield, and J. Lefkowitz, “The effect of inter-pulse coupling on gas temperature in nanosecond-pulsed high-frequency discharges,” *J. Phys. D. Appl. Phys.*, vol. 52, no. 35, p. 355203, Jul. 2019.

- [27] J. K. Lefkowitz and T. Ombrello, “An exploration of inter-pulse coupling in nanosecond pulsed high frequency discharge ignition,” *Combust. Flame*, vol. 180, pp. 136–147, 2017.
- [28] D. A. Xu, D. A. Lacoste, D. L. Rusterholtz, P. Q. Elias, G. D. Stancu, and C. O. Laux, “Experimental study of the hydrodynamic expansion following a nanosecond repetitively pulsed discharge in air,” *Appl. Phys. Lett.*, vol. 99, no. 12, pp. 2009–2012, 2011.
- [29] M. Castela *et al.*, “A 3-D DNS and experimental study of the effect of the recirculating flow pattern inside a reactive kernel produced by nanosecond plasma discharges in a methane-air mixture,” *Proc. Combust. Inst.*, vol. 36, no. 3, pp. 4095–4103, 2017.
- [30] S. P. M. M. Bane, J. L. Ziegler, and J. E. Shepherd, “Investigation of the Effect of Electrode Geometry on Spark Ignition,” *Combust. Flame*, vol. 162, no. 2, pp. 462–469, Feb. 2015.
- [31] M. Castela, B. Fiorina, A. Coussement, O. Gicquel, N. Darabiha, and C. O. Laux, “Modelling the impact of non-equilibrium discharges on reactive mixtures for simulations of plasma-assisted ignition in turbulent flows,” *Combust. Flame*, vol. 166, pp. 133–147, 2016.
- [32] C. Dumitrache, A. Gallant, N. Minesi, S. Stepanyan, G. D. Stancu, and C. O. Laux, “Hydrodynamic regimes induced by nanosecond pulsed discharges in air: Mechanism of vorticity generation,” *J. Phys. D: Appl. Phys.*, vol. 52, no. 36, p. 364001, Jul. 2019.
- [33] B. Singh, L. K. Rajendran, P. Gupta, C. Scalo, P. P. Vlachos, and S. P. Bane, “Experimental and Numerical Study of Flow Induced by Nanosecond Repetitively Pulsed Discharges,” in *AIAA SciTech Forum*, 2019, no. January, pp. 1–15.
- [34] J. M. Picone and J. P. Boris, “Vorticity generation by asymmetric energy deposition in a gaseous medium,” *Phys. Fluids*, vol. 26, no. 2, pp. 365–382, 1983.
- [35] J. M. Wang, D. A. Buchta, and J. B. Freund, “Hydrodynamic ejection caused by laser-induced optical breakdown,” *J. Fluid Mech.*, vol. 888, 2020.
- [36] C. Dumitrache and A. P. Yalin, “Gas dynamics and vorticity generation in laser-induced breakdown of air,” *Opt. Express*, vol. 28, no. 4, 2020.
- [37] D. Bradley, C. G. W. Sheppard, I. M. Suardjaja, and R. Woolley, “Fundamentals of high-energy spark ignition with lasers,” *Combust. Flame*, vol. 138, no. 1–2, pp. 55–77, 2004.
- [38] T. A. Spiglanin, A. Mcilroy, E. W. Fournier, R. B. Cohen, and J. A. Syage, “Time-resolved imaging of flame kernels: Laser spark ignition of H<sub>2</sub>/O<sub>2</sub>/Ar mixtures,” *Combust. Flame*, vol. 102, no. 3, pp. 310–328, 1995.
- [39] R. Maly and M. Vogel, “Initiation and propagation of flame fronts in lean CH<sub>4</sub>-air mixtures by the three modes of the ignition spark,” *Symp. Combust.*, vol. 17, no. 1, pp. 821–831, 1979.

- [40] M. T. Lim, R. W. Anderson, and V. S. Arpaci, "Prediction of spark kernel development in constant volume combustion," *Combust. Flame*, vol. 69, no. 3, pp. 303–316, 1987.
- [41] S. Au, R. Haley, and P. R. Smy, "The influence of the igniter-induced blast wave upon the initial volume and expansion of the flame kernel," *Combust. Flame*, vol. 88, no. 1, pp. 50–60, Jan. 1992.
- [42] T. N. Jukes and K.-S. Choi, "On the formation of streamwise vortices by plasma vortex generators," *J. Fluid Mech.*, vol. 733, pp. 370–393, Oct. 2013.
- [43] S. Stepanyan, J. Hayashi, A. Salmon, G. D. Stancu, and C. O. Laux, "Large-volume excitation of air, argon, nitrogen and combustible mixtures by thermal jets produced by nanosecond spark discharges," *Plasma Sources Sci. Technol.*, vol. 26, no. 4, 2017.
- [44] S. Lovascio, J. Hayashi, S. Stepanyan, G. D. Stancu, and C. O. Laux, "Cumulative effect of successive nanosecond repetitively pulsed discharges on the ignition of lean mixtures," *Proc. Combust. Inst.*, vol. 37, no. 4, pp. 5553–5560, 2019.
- [45] S. M. Soloff, R. J. Adrian, and Z. C. Liu, "Distortion compensation for generalized stereoscopic particle image velocimetry," *Meas. Sci. Technol.*, vol. 8, no. 12, pp. 1441–1454, 1997.
- [46] B. Wieneke, "Stereo-PIV using self-calibration on particle images," *Exp. Fluids*, vol. 39, no. 2, pp. 267–280, 2005.
- [47] C. Willert, "Stereoscopic digital particle image velocimetry for application in wind tunnel flows.," *Meas. Sci. Technol.*, vol. 8, no. 12, p. 1465, 1997.
- [48] A. Eckstein and P. P. Vlachos, "Digital particle image velocimetry (DPIV) robust phase correlation," *Meas. Sci. Technol.*, vol. 20, no. 5, 2009.
- [49] A. C. Eckstein and P. P. Vlachos, "Assessment of advanced windowing techniques for digital particle image velocimetry (DPIV).," *Meas. Sci. Technol.*, vol. 20, no. 7, p. 075402, Jul. 2009.
- [50] A. C. Eckstein, J. Charonko, and P. P. Vlachos, "Phase correlation processing for DPIV measurements," *Exp. Fluids*, vol. 45, no. 3, pp. 485–500, 2008.
- [51] F. Scarano and M. L. Riethmuller, "Iterative multigrid approach in PIV image processing with discrete window offset," *Exp. Fluids*, vol. 26, pp. 513–523, 1999.
- [52] F. Scarano and M. L. Riethmuller, "Advances in iterative multigrid PIV image processing," *Exp. Fluids*, vol. 29, pp. S051–S060, 2000.
- [53] F. Scarano, "Iterative image deformation methods in PIV," *Exp. Fluids*, vol. 13, pp. R1–R19, 2002.

- [54] J. Westerweel, D. Dabiri, and M. Gharib, “The effect of a discrete window offset on the accuracy of cross-correlation analysis of digital PIV recordings,” *Exp. Fluids*, vol. 23, pp. 20–28, 1997.
- [55] J. Westerweel and F. Scarano, “Universal outlier detection for PIV data,” *Exp. Fluids*, vol. 39, no. 6, pp. 1096–1100, 2005.
- [56] M. Willert, C.E. and Gharib, “Digital Particle Image Velocimetry”, *Experiments in Fluids*,” *Exp. Fluids*, vol. 3, pp. 181–193, 1991.
- [57] C. Willert, “Stereoscopic digital particle image velocimetry for application in wind tunnel flows,” *Meas. Sci. Technol.*, vol. 8, no. 12, pp. 1465–1479, 1999.
- [58] M. C. Brindise and P. P. Vlachos, “Proper orthogonal decomposition truncation method for data denoising and order reduction,” *Exp. Fluids*, vol. 58, no. 4, pp. 1–18, 2017.
- [59] A. Sciacchitano, “Uncertainty quantification in particle image velocimetry,” *Meas. Sci. Technol.*, vol. 30, no. 9, 2019.
- [60] J. J. Charonko and P. P. Vlachos, “Estimation of uncertainty bounds for individual particle image velocimetry measurements from cross-correlation peak ratio,” *Meas. Sci. Technol.*, vol. 24, no. 6, 2013.
- [61] Z. Xue, J. J. Charonko, and P. P. Vlachos, “Particle image velocimetry correlation signal-to-noise ratio metrics and measurement uncertainty quantification,” *Meas. Sci. Technol.*, vol. 25, no. 11, 2014.
- [62] Z. Xue, J. J. Charonko, and P. P. Vlachos, “Particle image pattern mutual information and uncertainty estimation for particle image velocimetry,” *Meas. Sci. Technol.*, vol. 26, no. 7, 2015.
- [63] B. Wieneke, “PIV uncertainty quantification from correlation statistics,” *Meas. Sci. Technol.*, vol. 26, no. 7, p. 074002, Jul. 2015.
- [64] A. Sciacchitano, B. Wieneke, and F. Scarano, “PIV uncertainty quantification by image matching,” *Meas. Sci. Technol.*, vol. 24, no. 4, p. 045302, Apr. 2013.
- [65] S. Bhattacharya, J. J. Charonko, and P. P. Vlachos, “Particle image velocimetry (PIV) uncertainty quantification using moment of correlation (MC) plane,” *Meas. Sci. Technol.*, vol. 29, no. 11, p. 115301, Nov. 2018.
- [66] S. Bhattacharya, J. J. Charonko, and P. P. Vlachos, “Stereo-particle image velocimetry uncertainty quantification,” *Meas. Sci. Technol.*, vol. 28, no. 1, 2017.
- [67] A. Sciacchitano *et al.*, “Collaborative framework for PIV uncertainty quantification: Comparative assessment of methods,” *Meas. Sci. Technol.*, vol. 26, no. 7, 2015.

- [68] M. Raffel, “Background-oriented schlieren (BOS) techniques,” *Exp. Fluids*, vol. 56, no. 3, pp. 1–17, 2015.
- [69] L. K. Rajendran, J. Zhang, S. Bhattacharya, S. P. M. Bane, and P. P. Vlachos, “Uncertainty quantification in density estimation from background-oriented Schlieren measurements,” *Meas. Sci. Technol.*, vol. 31, no. 5, Sep. 2020.
- [70] R. N. Bracewell, *The Fourier transform and its applications*, 2nd ed. New York: McGraw-Hill, 1986.
- [71] L. K. Rajendran, S. Bhattacharya, J. Zhang, S. P. M. Bane, and P. P. Vlachos, “Assessment of Uncertainty Quantification methods for density estimation from Background Oriented Schlieren ( BOS ) measurements,” in *13th International Symposium on Particle Image Velocimetry*, 2019, pp. 377–395.
- [72] A. Etebari and P. Vlachos, “Improvements on the accuracy of derivative estimation from DPIV velocity measurements,” *Exp. Fluids*, pp. 39(6), 1040–1050, 2005.
- [73] J. Zhou, R. J. Adrian, S. Balachandar, and T. M. Kendall, “Mechanisms for generating coherent packets of hairpin vortices in channel flow,” *J. Fluid Mech.*, vol. 387, pp. 353–396, 1999.
- [74] D. L. Jones, G. G. Goyer, and M. N. Plooster, “Shock Wave from a Lightning Discharge,” *J. Geophys. Res.*, vol. 73, no. 10, 1968.
- [75] S. Stanaway, K. Shariff, and F. Hussain, “Head-on collision of viscous vortex rings,” *Proc. Summer Progr.*, no. Hussain 1986, pp. 287–309, 1988.
- [76] H. W. Coleman and W. G. Steele, *Experimentation, Validation, and Uncertainty Analysis for Engineers*. Hoboken, New Jersey: John Wiley & Sons, Inc., 2009.
- [77] A. Starikovskiy and N. Aleksandrov, “Plasma-Assisted Ignition and Combustion,” *Prog. Energy Combust. Sci.*, vol. 39, no. 1, pp. 61–110, 2013.
- [78] G. Pilla, D. Galley, D. A. Lacoste, F. Lacas, D. Veynante, and C. O. Laux, “Stabilization of a Turbulent Premixed Flame Using a Nanosecond Repetitively Pulsed Plasma,” *IEEE Trans. Plasma Sci.*, vol. 34, no. 6, pp. 2471–2477, Dec. 2006.
- [79] M. Thiele, J. Warnatz, & U. Maas, and U. Maas, “Geometrical study of spark ignition in two dimensions,” *Combust. Theory Model.*, vol. 4, no. 4, pp. 413–434, Dec. 2000.
- [80] B. Singh, L. K. Rajendran, P. P. Vlachos, and S. P. M. Bane, “Two regime cooling in flow induced by a spark discharge,” *Phys. Rev. Fluids*, vol. 5, no. 1, p. 14501, 2020.
- [81] P. G. Saffman, “The Velocity of Viscous Vortex Rings,” *Stud. Appl. Math.*, vol. 49, no. 4, pp. 371–380, Dec. 1970.
- [82] P. G. Saffman, *Vortex dynamics*. Cambridge university press, 1992.

- [83] L. E. Fraenkel, “On steady vortex rings of small cross-section in an ideal fluid,” 1970.
- [84] J. Norbury, “A family of steady vortex,” *J. Fluid Mech.*, vol. 57, pp. 417–431, 1973.
- [85] H. Lamb, *Hydrodynamics*. Cambridge university press, 1895.
- [86] C. Tung and L. Ting, “Motion and decay of a vortex ring,” *Phys. Fluids*, vol. 10, no. 5, pp. 901–910, 1967.
- [87] S. S. Yoon and S. D. Heister, “Analytical formulas for the velocity field induced by an infinitely thin vortex ring,” *Int. J. Numer. Methods Fluids*, vol. 44, no. 6, pp. 665–672, 2004.
- [88] H. Helmholtz, “On Integrals of the hydrodynamical equations, which express vortex-motion,” *London, Edinburgh, Dublin Philos. Mag. J. Sci.*, vol. 33, pp. 485–512, 1867.
- [89] M. N. Slipchenko, J. D. Miller, S. Roy, T. R. Meyer, J. G. Mance, and J. R. Gord, “100 kHz, 100 ms, 400 J burst-mode laser with dual-wavelength diode-pumped amplifiers.,” *Opt. Lett.*, vol. 39, no. 16, pp. 4735–8, 2014.
- [90] “No Title.” [Online]. Available: <https://github.com/aether-lab/prana>.
- [91] L. Rajendran, J. Zhang, S. Bane, and P. Vlachos, “Weighted Least Squares (WLS) Density Integration for Background Oriented Schlieren (BOS),” *arXiv Prepr. arXiv2004.01217*, pp. 1–14, Apr. 2020.
- [92] L. K. Rajendran, B. Singh, R. Jagannath, G. N. Schmidt, P. P. Vlachos, and S. P. Bane, “Experimental Characterization of Flow Induced by a Nanosecond Surface Discharge,” 2020.
- [93] A. Santhanakrishnan and J. D. Jacob, “Flow control with plasma synthetic jet actuators,” *J. Phys. D. Appl. Phys.*, vol. 40, no. 3, pp. 637–651, 2007.
- [94] V. Svetsov, M. Popova, V. Rybakov, V. Artemiev, and S. Medveduk, “Jet and vortex flow induced by anisotropic blast wave: experimental and computational study,” 1997.
- [95] B. Singh, L. K. Rajendran, J. Zhang, P. P. Vlachos, and S. P. M. Bane, “Vortex rings drive entrainment and cooling in flow induced by a spark discharge,” *Phys. Rev. Fluids*, vol. 5, p. 114501, 2020.
- [96] L. K. Rajendran, B. Singh, P. Vlachos, and S. Bane, “Filamentary Surface Plasma Discharge Flow Length and Time Scales,” *J. Phys. D. Appl. Phys.*, vol. 54, no. 20, p. 205201, Feb. 2021.
- [97] T. X. Phuoc, “Laser-induced spark ignition fundamental and applications,” *Opt. Lasers Eng.*, vol. 44, no. 5, pp. 351–397, 2006.
- [98] T. X. Phuoc, “Laser-induced spark ignition fundamental and applications,” *Optics and Lasers in Engineering*, vol. 44, no. 5, pp. 351–397, 2006.

- [99] W. D. Hayes, “The vorticity jump across a gasdynamic discontinuity,” *J. Fluid Mech.*, vol. 2, no. 6, pp. 595–600, Aug. 1957.
- [100] C. Truesdell, “On Curved Shocks in Steady Plane Flow of an Ideal Fluid,” *J. Aeronaut. Sci.*, vol. 19, no. 12, pp. 826–828, Dec. 1952.
- [101] M. Lighthill, *Dynamics of a dissociating gas, Part {I}. Equilibrium flow*, vol. 2, no. 1. 1957.
- [102] W. D. Hayes and R. F. Probstein, “General Considerations,” in *Hypersonic flow theory*, New York and London: Academic Press, 1959, pp. 1–29.
- [103] H. G. Hornung, “Gradients at a curved shock in reacting flow,” *Shock Waves*, vol. 8, no. 1, pp. 11–21, 1998.
- [104] H. G. Hornung, “Vorticity generation and secondary flows,” in *Tenth Australian fluid mechanics conference*, 1989.
- [105] D. Bershader, “Compressible vortices,” in *Fluid vortices*, Springer, 1995, pp. 291–316.
- [106] E. M. Greitzer, C. S. Tan, and M. B. Graf, “Vorticity and circulation,” in *Internal Flow: Concepts and Applications*, Cambridge University Press, 2004, pp. 104–165.
- [107] S. Mölder, “Curved shock theory,” *Shock Waves*, vol. 26, no. 4, pp. 337–353, 2016.
- [108] S. Ghosh and K. Mahesh, “Numerical simulation of the fluid dynamic effects of laser energy deposition in air,” *J. Fluid Mech.*, vol. 605, pp. 329–354, 2008.
- [109] O. Ekici, O. A. Ezekoye, M. J. Hall, and R. D. Matthews, “Thermal and Flow Fields Modeling of Fast Spark Discharges in Air,” *J. Fluids Eng.*, vol. 129, no. 1, p. 55, 2007.
- [110] B. Wieneke, “Volume self-calibration for 3D particle image velocimetry,” *Exp. Fluids*, vol. 45, no. 4, pp. 549–556, Oct. 2008.
- [111] F. Scarano, “Tomographic PIV: Principles and practice,” *Meas. Sci. Technol.*, vol. 24, no. 1, 2013.
- [112] G. E. Elsinga, F. Scarano, B. Wieneke, and B. W. Van Oudheusden, “Tomographic particle image velocimetry,” *Exp. Fluids*, vol. 41, no. 6, pp. 933–947, 2006.
- [113] G. E. Elsinga, J. Westerweel, F. Scarano, and M. Novara, “On the velocity of ghost particles and the bias errors in Tomographic-PIV,” in *Experiments in Fluids*, 2011, vol. 50, no. 4, pp. 825–838.
- [114] M. Novara, K. J. Batenburg, and F. Scarano, “Motion tracking-enhanced MART for tomographic PIV,” *Meas. Sci. Technol.*, vol. 21, no. 3, 2010.
- [115] J. Westerweel and F. Scarano, “Universal outlier detection for PIV data,” *Exp. Fluids*, vol. 39, no. 6, pp. 1096–1100, Dec. 2005.

- [116] B. Wieneke, “Iterative reconstruction of volumetric particle distribution,” *Meas. Sci. Technol.*, vol. 24, no. 2, pp. 24008–24022, 2013.
- [117] D. Schanz, S. Gesemann, and A. Schröder, “Shake-The-Box: Lagrangian particle tracking at high particle image densities,” *Exp. Fluids*, vol. 57, no. 5, p. 70, 2016.
- [118] D. Schanz, S. Gesemann, A. Schröder, B. Wieneke, and M. Novara, “Non-uniform optical transfer functions in particle imaging: Calibration and application to tomographic reconstruction,” *Meas. Sci. Technol.*, vol. 24, no. 2, p. 024009, Dec. 2013.
- [119] M. Novara, D. Schanz, N. Reuther, C. J. Kähler, and A. Schröder, “Lagrangian 3D particle tracking in high-speed flows: Shake-The-Box for multi-pulse systems,” *Exp. Fluids*, vol. 57, no. 8, p. 128, 2016.

# VITA

## EDUCATION

---

**Purdue University** *West Lafayette, IN* May 2021  
Ph.D. in Aeronautics and Astronautics  
Thesis: Characterization of flow induced by a single nanosecond spark discharge in quiescent air  
Advisor: Professor Sally P.M. Bane

**Purdue University** *West Lafayette, IN* December 2015  
M.Sc. in Aeronautics and Astronautics  
Thesis: Development of particle image velocimetry for plasma induced flow measurements  
Advisor: Professor Sally P.M. Bane

**Purdue University** *West Lafayette, IN* December 2012  
B.S. in Aeronautics and Astronautics

## RESEARCH

---

**Graduate research assistant (Ph.D.)** January 2016 – May 2021

**Purdue University, Aerospace Sciences and Zucrow Laboratories**

Characterizing the flow induced by nanosecond spark plasma discharges to determine the mechanisms driving cooling of the induced hot gas. Designed sets of high spatiotemporal resolution stereoscopic particle image velocimetry (S-PIV) and background oriented schlieren (BOS) measurements to capture the flow induced by a single spark and showed the presence of a pair of vortex rings around the induced hot gas kernel. Developed reduced order vortex ring cooling models to show the role of vortex rings in the entrainment of cold ambient gas and subsequent cooling of the hot gas kernel as well as to quantify the time scales at which the cooling takes place. Designed 50 kHz tomographic PIV experiments to study the 3D nature of the induced flow field, specifically the induced vortex rings. Designed 700 kHz schlieren experiments to capture the shock wave induced by a single spark discharge and used models of vorticity generated due to shock curvature to estimate the vorticity generated due to the shock wave and compare to PIV data of the induced vortex rings.

**Graduate research assistant (M.Sc.)** January 2016 - December 2015

**Purdue University, Aerospace Sciences Laboratory**

Designed and executed planar PIV experiments to capture the flow fields induced by spark plasma discharges and determine the main flow features of the induced flow field. Designed and prototyped a 3D printed wind model and collected surface pressure measurements in a wind tunnel, to provide validation data for CFD models.

## TEACHING AND COURSE DEVELOPMENT

---

**Course developer** January 2019 – May 2021

**School of Engineering Education-First Year Engineering, Purdue University**

Develop in-class material for instruction of design and programming in MATLAB to 2000+ incoming students. Coordinate Engineering Your Major events that inform first-year students on the different engineering majors ahead of their transition to major.

**Course Instructor** August 2017 - December 2018

**School of Engineering Education-First Year Engineering, Purdue University**

Led classes each week on engineering design and programming in MATLAB. Mentored new graduate teaching assistants and undergraduate teaching assistants for the class.

**Teaching Assistant** January 2015 - December 2015

**School of Aeronautics and Astronautics, Purdue University**

Led fluid dynamics and aerodynamics laboratory sessions for undergraduate students and graded lab reports.

**Teaching Assistant** January 2013 – May 2017

**School of Engineering Education-First Year Engineering, Purdue University**

Taught MATLAB and engineering design during one-on-one in-class sessions. Mentored and managed undergraduate teaching assistants who aided with in-class instruction.

Recipient of Estus H. and Vashti L. Magoon award for Excellence in Teaching.

## JOURNAL PUBLICATIONS

---

**Singh, B.**, Rajendran, L. K., Vlachos, P. P., & Bane, S. P. (2021). "Estimation of vorticity generated due to a spark induced shock wave." *Journal of Physics D: Applied Physics*. (Under review).

Rajendran, L. K., **Singh, B.**, Vlachos, P., & Bane, S. (2021). Filamentary Surface Plasma Discharge Flow Length and Time Scales. *Journal of Physics D: Applied Physics*.

**Singh, B.**, Rajendran, L. K., Zhang, J., Vlachos, P. P., & Bane, S. P. (2020). Vortex rings drive entrainment and cooling in flow induced by a spark discharge. *Physical Review Fluids*, 5(11), 114501.

**Singh, B.**, Rajendran, L. K., Vlachos, P. P., & Bane, S. P. "Two regime cooling in flow induced by a spark discharge." *Physical Review Fluids* (2020). (Selected for Editors highlights) doi: 10.1103/PhysRevFluids.5.014501

**Singh, B.**, Rajendran, L. K., Giarra, M., Vlachos, P. P., & Bane, S. P. "Measurement of the flow field induced by a spark plasma using particle image velocimetry." *Experiments in Fluids* (2018). doi: 10.1007/s00348-018-2632-y

## CONFERENCE PUBLICATIONS AND PRESENTATIONS

---

- Singh, B.**, Rajendran, L. K., Vlachos, P. P., & Bane, S. P. (2020). "Study of cooling and the effect of energy deposited in a single nanosecond spark plasma discharge using simultaneous 50 kHz PIV and BOS." In *AIAA Scitech 2020 Forum* (p.1885). doi: 10.2514/6.2020-1885
- Rajendran, L. K., **Singh, B.**, Jagannath, R., Schmidt, G. N., Vlachos, P. P., & Bane, S. P. (2020). "Experimental Characterization of Flow Induced by a Nanosecond Surface Discharge." *AIAA Scitech 2020 Forum*. doi: 10.2514/6.2020-1164
- Singh, B.**, Rajendran, L.K., Vlachos, P. P., & Bane, S. (2019). "Vorticity Generation in a Single Nanosecond Spark Discharge Due to Shock Curvature." In *APS Division of Fluid Dynamics Meeting Abstracts*.
- Rajendran, L.K., **Singh, B.**, Jagannath, R., Schmidt, G.N., Vlachos, P., Bane. S. (2019). "Experimental Characterization of Flow Induced by a Nanosecond Surface Discharge." In *APS Division of Fluid Dynamics Meeting Abstracts*.
- Singh, B.**, Rajendran, L. K., Gupta, P., Scalo, C., Vlachos, P. P., & Bane, S. P. (2019). "Experimental and Numerical Study of Flow Induced by Nanosecond Repetitively Pulsed Discharges." *AIAA Scitech 2019 Forum*. doi:10.2514/6.2019-0740
- Singh, B.**, Rajendran, L. K., Bane, S. P., & Vlachos, P. (2018). "Characterization of Fluid Motion Induced by Nanosecond Spark Plasmas: Using Particle Image Velocimetry and Background Oriented Schlieren." *2018 AIAA Aerospace Sciences Meeting*. doi:10.2514/6.2018-0680
- Singh, B.**, Rajendran, L.K., Vlachos, P. P., & Bane, S. (2018). "Characterization of early stages of flow induced by spark plasma discharges using high-speed PIV and BOS." In *APS Division of Fluid Dynamics Meeting Abstracts*.
- Singh, B.**, Rajendran, L. K., Bane, S. P., & Vlachos, P. (2018). "Characterization of fluid motion induced by nanosecond spark plasmas: Using particle image velocimetry and background oriented schlieren." In *2018 AIAA aerospace sciences meeting*. doi: 10.2514/6.2018-0680
- Rajendran, L. K., **Singh, B.**, Giarra, M., Bane, S. P., & Vlachos, P. P. (2017). "PIV/BOS Synthetic Image Generation in Variable Density Environments for Error Analysis and Experiment Design." *55th AIAA Aerospace Sciences Meeting*. doi:10.2514/6.2017-0254
- Singh, B.**, Rajendran, L.K., Giarra, M., Bane, S., & Vlachos, P. (2016). "Study of shock shape and strength as a function of plasma energy using background oriented schlieren and shadowgraph." In *APS Division of Fluid Dynamics Meeting Abstracts*.
- Rajendran, L.K., **Singh, B.**, Giarra, M., Bane, S., & Vlachos, P. (2016). "Assessment of sources of error in Background Oriented Schlieren (BOS) measurements." In *APS Division of Fluid Dynamics Meeting Abstracts*.

**Singh, B.,** Rajendran, L. K., Giarra, M., Bane, S. P., & Vlachos, P. (2016). "Fluid Motion Induced by Spark Plasma: Development of Particle Image Velocimetry Measurements." *54th AIAA Aerospace Sciences Meeting*. doi:10.2514/6.2016-1214

**Singh, B.,** Belmouss, M., & Bane, S. P. (2015). "Characterization of Flow Control Actuators Based on Spark Discharge Plasmas Using Particle Image Velocimetry." In *46th AIAA Plasmadynamics and Lasers Conference*. doi: 10.2514/6.2015-3249

## **SYNERGETIC ACTIVITIES**

---

**Aerospace engineering graduate women's group (GWG) ambassador** May 2019 - May 2020  
**School of Aeronautics and Astronautics, Purdue University**

Led and organized graduate women and undergraduate women events to promote a sense of community within the department. Facilitated the second Amelia Earhart Aerospace Summit which is a student organized conference that highlights the role of women in aerospace

**Graduate student in aerospace leadership team (AeroAssist)** August 2016 – May 2017  
**School of Aeronautics and Astronautics, Purdue University**

Led and organized inter-departmental social, recreational and professional events geared towards graduate student wellness.

**Graduate student representative in course curator team** August 2017 – December 2019  
**School of Engineering Education-First Year Engineering, Purdue University**

Provided feedback on the development of instruction and course strategies for the first-year engineering courses Transforming Ideas to Innovation I and II.

### **Awards and Memberships**

Caltech Young Investigator Lecture series presenter award

Journal publication selected as editors' highlights.

**Singh, B.,** Rajendran, L. K., Vlachos, P. P., & Bane, S. P. "Two regime cooling in flow induced by a spark discharge." *Physical Review Fluids* (2020). (*Selected for Editors highlights*) doi: 10.1103/PhysRevFluids.5.014501

Estus H. and Vashti L. Magoon award for Excellence in Teaching

American Institute of Aeronautics and Astronautics (AIAA), American Physical Society (APS), Graduate Women in Engineering (GWEN)